SYNTHESIS AND CHARACTERIZATION OF MAGNETICALLY HARD Fe-Pt ALLOY NANOPARTICLES AND NANO-ISLANDS

by

Xiaocao Hu

A dissertation submitted to the Faculty of the University of Delaware in partial fulfillment of the requirements for the degree of Doctor of Philosophy in Materials Science and Engineering

Winter 2016

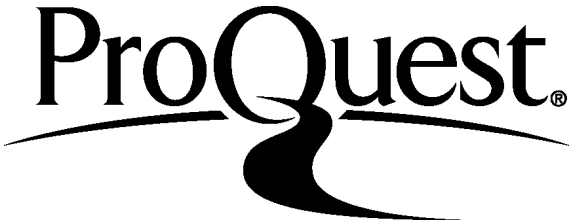

SYNTHESIS AND CHARACTERIZATION OF MAGNETICALLY HARD Fe-Pt ALLOY NANOPARTICLES AND NANO-ISLANDS

by

Xiaocao Hu

Approved: _____
Darrin Pochan, Ph.D.
Chair of the Department of Materials Science and Engineering

Approved: _____
Babatunde A. Ogunnaike, Ph.D.
Dean of the College of Engineering

Approved: _____
Ann L. Ardis, Ph.D.
Interim Vice Provost for Graduate and Professional Education

I certify that I have read this dissertation and that in my opinion it meets the academic and professional standard required by the University as a dissertation for the degree of Doctor of Philosophy.

Signed: _____

George C. Hadjipanayis, Ph.D.
Professor in charge of dissertation

I certify that I have read this dissertation and that in my opinion it meets the academic and professional standard required by the University as a dissertation for the degree of Doctor of Philosophy.

Signed: _____

John Q. Xiao, Ph.D.
Member of dissertation committee

I certify that I have read this dissertation and that in my opinion it meets the academic and professional standard required by the University as a dissertation for the degree of Doctor of Philosophy.

Signed: _____

Chaoying Ni, Ph.D.
Member of dissertation committee

I certify that I have read this dissertation and that in my opinion it meets the academic and professional standard required by the University as a dissertation for the degree of Doctor of Philosophy.

Signed: _____

Joshua Zide, Ph.D.
Member of dissertation committee

ACKNOWLEDGMENTS

Five years' Ph. D. research is like a long journey. During the process of research and writing the thesis, I received a lot of help from many kind people. At first, I would like to appreciate my advisor Professor George C. Hadjipanayis who not only gave me great guidance but also was always supportive in the past five years especially during my pregnancy period. The most important thing he taught me is that diligence is the key to success and you have to be prepared for future success.

I also would like to thank other members of my thesis committee, Dr. Xiao, Dr. Zide and Dr. Ni. I really appreciate their time on carefully reviewing my dissertation and providing constructive suggestions on my research project.

I would like to thank the kind and professional group members: Dr. Alexander Gabay for his proficiency of everything in the lab; Dr. Nilay Gunduz Akdogan and Ozan Akdogan who taught me how to use the sputtering system, fix the problems of this old system and how to do the characterization; Rob Schmidt and Dan Neil for help in measurements of AFM, PPMS and VSM. I also want to thank my cooperators Aldo Capobianchi from CNR in Italy and Vasilis Tzitzios from N.C.S.R in Greece for the great ideas they shared with me. They are both chemists and have given me significant guidance of the details to do a successful chemical reaction.

I acknowledge the great help from Dr. Chaoying Ni and Dr. Fei Deng in my EM work. Specially, I would like to thank Dr. Wanfeng Li because he guided me into the world of microscopy. He taught me how to use the TEM, analyze the data and prepare different kinds of TEM samples especially the planar view and cross-section

thin film samples by ion milling. He also gave me a lot of suggestions and encouragement when I encountered difficulties.

On top of all, I would like thank my husband Jun Jiang. He has been always with me for professional help and encouragement. He is the person that I always want to catch up for his intelligence and diligence. This dissertation is dedicated to my husband Jun and my dear son Miles.

TABLE OF CONTENTS

LIST OF TABLES

LIST OF FIGURES

ABSTRACT

In this dissertation, we explored the fabrication of FePt nanoparticles and nano-islands with the face-centered tetragonal (fct, $L1_0$) phase prepared by both chemical synthesis routes and physical vapor deposition. Microstructure and magnetic properties characterizations were used to gain a fundamental understanding of the nano-structure formation and atomic ordering behavior and determine the possible applications in the next generation ultra-high density magnetic storage media.

FePt nanoparticles prepared by thermal decomposition of iron pentacarbonyl [$Fe(CO)_5$] have been widely investigated and by tuning the processing procedure monodispersed FePt nanoparticles with good assembly can be obtained. The as-made FePt nanoparticles are usually in the magnetically soft face-centered cubic (fcc) phase. To transformation to the fct phase, post-annealing at above 600℃ is needed which, however, introduces undesirable agglomeration and sintering. To address this problem, we used three different fabrication processes which are discussed below.

In the first fabrication experiment, the FePt nanoparticles were fabricated by a novel environmental friendly method involving crystalline saline complex hexaaquairon (II) hexachloroplatinate ($[Fe(H_2O)_6]PtCl_6$) with a special layered structure. Then the precursor was ball milled with NaCl and annealed at temperatures above 400℃ under a reducing atmosphere of forming gas (95% Ar and 5% H_2) FePt nanoparticles were obtained after washing away NaCl with deionized water. This method avoids the use of the very poisonous $Fe(CO)_5$ and other organic solvents such

as oleylamine and oleic acid. Instead, environmentally friendly NaCl and water were used. The size of FePt nanoparticles was controlled by varying the proportion of precursor and NaCl (from 10mg/20g to 50mg/20g). Particles with size in the range of 6.2–13.2 nm were obtained. All the nanoparticles annealed above 400℃ are in the highly ordered fct phase with a coercivity range of 4.7 kOe to 10.7 kOe. Compared with reported high annealing temperatures above 600℃, this fabrication process led to a significantly decreased temperature to achieve the $L1_0$ phase FePt by 200℃. A qualitative model was set up to explain the surprising low $L1_0$ phase achievement temperature and the influence of annealing temperature on the microstructure and magnetic properties was investigated.

Although FePt nanoparticles with high coercivity and small size were successfully obtained by the first fabrication method, agglomeration happened during the washing procedure due to the large inter-particle magnetostatic force caused by their high magnetization. To avoid this agglomeration, exfoliated graphene was introduced in the second preparation method to keep the nanoparticles separated. Different from the traditional solvent-phase reaction to disperse FePt nanoparticles onto the exfoliated graphene, a novel solid-phase reaction was used in this dissertation involving the layered precursor $[Fe(H_2O)_6]PtCl_6$ molecule. The $[Fe(H_2O)_6]PtCl_6$ water solution was mixed with exfoliated graphene oxide (GO) and then the top solution was removed. Fe^{2+} and Pt^{2+} ions were absorbed onto the surface of GO. The remaining product was annealed under a reducing atmosphere of forming gas at different temperatures (500℃ to 950℃). During the reduction process, GO was reduced to "graphene" and FePt nanoparticles were formed on the surface of exfoliated graphene. The separation effect by the exfoliated graphene increased the phase transformation

temperature to 600℃ compared to the first method. However, even at an annealing temperature as high as 750℃, we could still obtained separated, small size FePt nanoparticles with coercivity of 8.3 kOe.

The third preparation method used in this dissertation is the traditional magnetron sputtering with very short deposition time (10 s to 25 s) on heated MgO (001) substrate to form separate nano-islands instead of continuous thin films. The ordering of FePt nano-islands were studied by high resolution transmission electron microscopy. Because of the low degree of atomic ordering of the as-prepared nano-islands, post annealing at 700℃ under an atmosphere of forming gas was introduced. Ordering of nano-islands of as small as 3 nm was revealed. We discovered that in the ordered FePt nano-islands, there are defects present. Particularly, we observed an onion like structure in a FePt nano-island composed of c-domains perpendicular to each other. These defects explained the low coercivity of the L10 ordered FePt nano-islands, which was envisioned theoretically.

In summary, in this dissertation, novel solid-phase, environmentally friendly synthesis methods to fabricate FePt nanoparticles and FePt nanoparticles on "graphene" with high coercivity are first reported. Also, a special onion-like structure was first discovered by high-resolution microscopy and theoretical simulation was done with good agreement with the experimental results.

Chapter 1

INTRODUCTION

Richard Feynman first gave his famous talk “There is Plenty of Room at the Bottom” in 1959 which inspired the foundation of the concept of “nanotechnology”. The invention of scanning tunneling microscope (STM) in 1980s has introduced the boost of nanotechnology development. Nanotechnology also attracted great interest of the scientists to apply it to magnetic materials which is called “nanomagnetism”. Ever since the first half of the 20th century, magnetic nanostructures have been widely investigated and there are plenty of present and emerging applications such as magnetic recording media [1], soft magnets [2], permanent magnets [3], sensors [4] and spin electronics [5].

There are several advantages of the magnets with nanostructures:

1. The key advantage of nanomagnets is their ability to have better magnetic properties than naturally existed magnets. Nanostructured permanent and soft magnets are the examples.
2. Nanomagnets can be fabricated with a variety of geometries such as nanoparticles, nanotubes, nanowires, thin films and nano-islands. Great progress has been made towards tuning the chemistry, crystallographic microstructure and magnetic properties of a given geometry [6]. For example, plenty of work has been done to obtain monodispersed magnetic nanoparticles, nano rods and nanowires. Nanotubes can be produced as both hard and soft magnets.

3. Nanomagnetism involves physics of a mixture of atomic-scale and macroscopic effects. For example, the competition between relativistic corrections (e.g. spin-orbit coupling) and electrostatic interactions (e.g. exchange) in on a scale of a few nanometers which gives rise to a variety of zero- and finite-temperature governing the static and dynamic behavior of the nanostructures. [6]

To be specific, the fabrication process of high anisotropy magnetic nanoparticles with uniform size distribution, good magnetic properties and without post-annealing is widely discussed and investigated due to its potential application in magnetic sensors [7], magnetic filter [8], high performance magnets as the building blocks of the bottom-up approach [9] and catalysts in the oxygen reduction reaction (ORR) [10].

The next generation ultra-high-density magnetic recording media requires the size of the magnetic nanoparticles to be very small to include more bits in one disk to increase the areal density [11]. However, the superparamagnetic effect has set up the size limit. The most commonly used Co based alloy has reached its physical limit. Binary alloys such as FePt [12], CoPt [13] and FePd [14] have been discussed widely due to their high anisotropy energy which allow their superparamagnetic limit size to be smaller than 3 nm.

In this dissertation, the fabrication approaches of FePt alloy nanoparticles have been investigated. There are two major types of fabrication method widely used by the scientists. One is the reduction of Fe salts and Pt salts in a chemical synthesis [15-17] and the other one is physical vapor deposition (PVD) such as magnetron sputtering [18-20]. Although plenty work has been done during the past twenty years, the

magnetically hard $L1_0$ phase and uniform size distribution is still a dilemma for scientists.

To solve this problem, in the first part of this dissertation, a special layered structured crystal precursor $Fe(H_2O)_6PtCl_6$ with alternative Fe and Pt layers was introduced . This special layered structure significantly decreased the temperature (a 250℃ decrease) to achieve the $L1_0$ phase of FePt nanoparticles. Planetary ball milling technique was used to decrease the size of FePt from bulk to the nano-scale. Another significant advantages of this fabrication method is that only environmental friendly NaCl salt matrix and deionized water was used during the fabrication process instead of organic solvents. Therefore, this method is called “green synthesis”.

Although well separated small FePt nanoparticles with reasonable coercivity is successfully prepared, the problem of agglomeration and a wide size distribution still exists due to the mechanism of planetary ball milling and the magnetostatic force between the nanoparticles. To further improve the size distribution, exfoliated graphene support was used. The significance of this work is that it has provide a new routine to fabrication binary alloy nanoparticles on the surface of graphene. FePd, CoPt etc. nanoparticles can also be made by changing the composition of precursor. What is more important, is that well separated magnetically hard FePt nanoparticles do not only have the application in ultra-high-density magnetic recording but also can be used as very good catalysts for many reactions.

In the last part, magnetron sputtering was used to prepare FePt nano-islands. Heated (001) MgO substrate was used to achieve an epitaxial growth of FePt nano-islands in $L1_0$ phase. . Not very high coercivity was achieved even after high temperature annealing. An ultra-high resolution transmission electron microscopy

(TEM) TEAM 0.5 which is one of the two best TEMs in the world was used. The significance of this work is that the ultra-high resolution TEM has provided the possibility to see the FePt nano-islands in atom scale. Ordered FePt nano-islands with the particle size as small as 3 nm was found. Specially, an onion like structure was first discovered. QSTEM modeling was used to simulate this structure and the phase simulation results was in good accordance with the experimental results.

Chapter 2

PREVIOUS STUDY ON FePt NANOPARTICLES

2.1 Fundamental Properties of FePt Nanoparticles

2.1.1 Structure of FePt

As seen from Figure 1[16], stoichiometric FePt alloy has two phases one of which is face-centered cubic (fcc) and the other one is face-centered tetragonal (fct) or $L1_0$ structure (shown in Figure 2[16]). In the disordered fcc structure, the probability of face and corner sites being occupied by a specific type of atom is the same. $L1_0$ is a crystallographic derivative structure of the fcc structure and has two of the faces occupied by one type of atom and the corner and the other face occupied with the other type of atom[21]. Therefore, $L1_0$ phase is usually called the ordered phase. The disordered to ordered (fcc to $L1_0$) transformation will introduce translational domains (also called anti-phase domains, see Figure 3[21]), orientational domains (also called variants or merohedral twins, see Figure 4[21]) and magnetic domains. The first two type of domains are produced by the lowering of translational and point symmetry. The magnetic domains are due to the transformation from paramagnetic to ferromagnetic domains. The $L1_0$ phase of FePt is stable at the temperature less than 1300℃. The fcc to $L1_0$ transformation is a first-order transformation but the reaction can happen homogeneously and continuously when the reaction temperature is away from the equilibrium phase boundary and below the instability temperature.

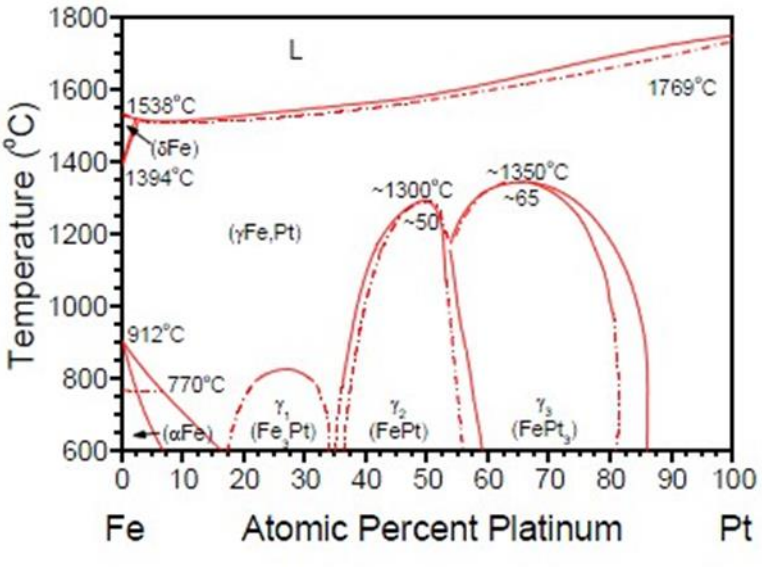

Figure 1 Phase diagram of FePt[16]

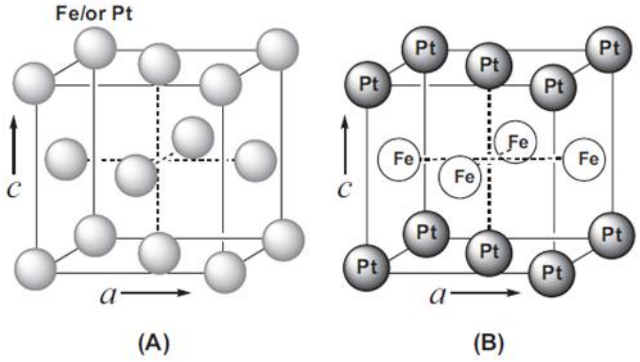

Figure 2 fcc and L10 structure of FePt[16]

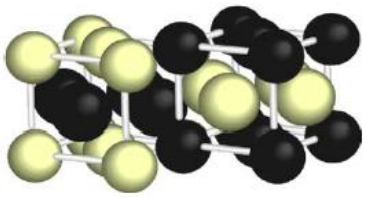

Figure 3 The two translational domains of the $L1_0$ structure along with its higher energy anti-phase boundary[21]

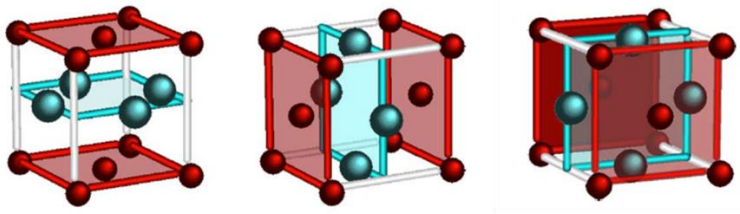

Figure 4 The three orientational domains or variants[21]

2.1.2 Magnetic Properties of FePt

The fcc-structured FePt has a small coercivity and is magnetically soft. The fully-ordered FePt with $L1_0$ structure has Fe and Pt atom layered alternating along the [001] direction (the c-axis in Figure 2B). The anisotropy constant K measures the ease of magnetization reversal along the easy axis. Compared to known rare earth elements based alloys, FePt with $L1_0$ structure has a very high anisotropy energy (up to 6.6×10^7 erg/cc) and high resistance to oxidation[15, 22]. The large anisotropy is due to Fe and Pt interactions from the spin-orbit coupling and the hybridization between Fe 3d and Pt 5d states. Meanwhile, the Fe-Pt interatomic interaction makes the FePt nanoparticles more chemically stable compared with the common high-moment nanoparticles of Co and Fe, as well as the large coercive materials of $SmCo_5$ and $Nd_2Fe_{14}B$.

2.2 Technological Applications-- Ultra-High Density Magnetic Recording

The first hard disk drive (HDD) was invented by IBM in 1953, with the capacity of 5 MB using 50 magnetic disks[23] with a diameter of 24 in whose areal density (number of bits per square inch of disk surface) was 2 KB/in^2. For more than five decades, HDD has been used as the primary storage device for computers. The areal density of HDD experienced a rapid growth in late 1990s, reaching 100% increase in some years [24]. In the year of 2011 an areal density of 744 GB/in^2 was reported and it was predicted that the HDD areal density will be doubled in five years according to a report from IHSi iSuppli Research [25].

The traditional magnetic recording devices were mainly longitudinal recording where the easy axis of magnetization lies in the plane of the recording media as is shown in Figure 5(a)[26]. However, since late 1990s, it has been known that the superparamagnetic limit will prevent the increasing of areal density. Perpendicular recording which was first proposed in the late 1970s with [27-29] the preferred axis of magnetization is normal to the plane of recording film [30] (see Figure 5(b)), has been considered as a promising method to further increase the areal density. HDD with perpendicular recording media was first commercialized in 2007 [31].

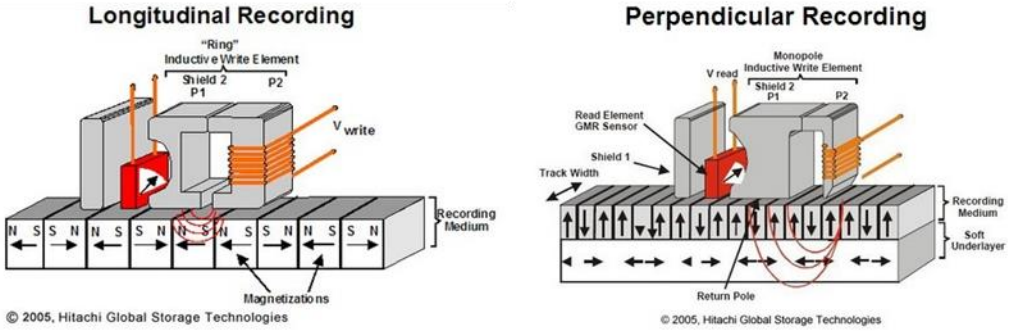

Figure 5 Schematic views of (a) longitudinal and (b) perpendicular magnetic recording[26]

To further increase the areal density, the magnetic units have been made smaller and smaller to keep a large signal to noise ratio (SNR) down to the smallest possible units- grains. According to the discussion in the review by Rithter [30, 32], the energy stored in one grain is KV, where K is the magnetic anisotropy energy density and V is the volume of the grain. KV competes against the thermal energy k_BT where k_B is Boltzmann constant and T is the temperature. Magnetic anisotropy energy must be large enough to prevent spontaneous magnetization reversals which cause undesirable thermal decays. In principle, to obtain a high SNR, a small volume of the material is required which indicates a high K value. Higher anisotropy energy K usually goes with higher anisotropy field H_A which demands a higher switch field. However the switch fields are limited by the material to fabricate the magnetic poles. Thus the design space is constrained by the so-called "trilemma": thermal stability, SNR and writing ability. To break or more precisely postpone the trilemma, there are several ways such as perpendicular recording [33], heat-assisted magnetic recording [34] and self-organized-magnetic-array (SOMA)-type bit patterned media [35]. However, all of these methods are based on the development of magnetic recording materials. The materials should have high anisotropy energy and high coercivity (to overcome the superparamagnetic limit), and also good thermal stability of itself at room temperature. All of these requirements make FePt a promising candidate for ultra-high density recording media.

2.3 Fabrication Approach of FePt Nanoparticles

One of the commonly used fabrication method is to use the vacuum-deposition techniques (magnetron sputtering). The most popular sputtering equipment is shown in Figure 6. An FePt target is used as the source of sputtering and the substrate (Si, MgO,

etc.) is placed at the top of the chamber. To achieve certain structure of the thin film, the substrate can be heated. The as-deposited FePt films usually have a chemically disordered fcc structure and are magnetically soft. Post-deposition annealing is essential to transform the fcc structure into the chemically ordered face-centered tetragonal (fct) (also called $L1_0$) structure. However, random nucleation in the early stage of growth leads to broad distribution of particle size.

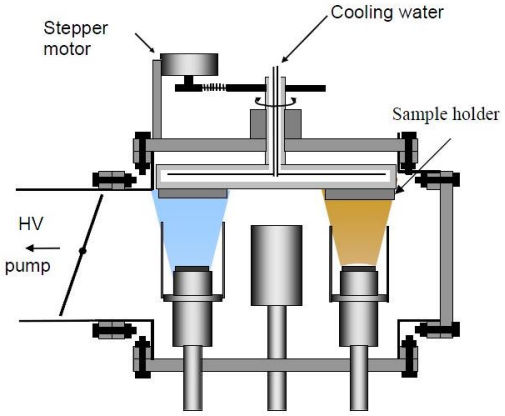

Figure 6 Demonstration of typical sputtering system

To control the size and narrow the size distribution, two methods are commonly used. One of the methods is to bury the vacuum-deposited FePt nanoparticles in a variety of insulator matrices. Chih-Ming Kuo et al. fabricated separated $L1_0$ FePt nanoparticles in Si_3N_4 matrix (see Figure 7) with a coercivity of 10 kOe after the annealing at 750℃ for 30 min [36]. The composition is $(FePt)_{70}$–$(Si_3N_4)_{30}$. C. P. Luo et al. successfully prepared separated FePt nanoparticles in SiO_2 matrix [37] with 10 kOe coercivity after the annealing at 650℃ for 30 min. Researchers also tried the Al_2O_3 [38] and B_2O_3 [39] matrix to avoid the agglomeration and sintering during the high temperature annealing but the size discrepancy of FePt

nanoparticles is still large. The other method is the epitaxial growth of single crystal FePt thin films [40-42] and isolated islands [43, 44] prepared by magnetron sputtering. When grown on heated single crystalline MgO (001) substrates, FePt films have a (001) texture with the magnetization preferred direction along c-axis. To obtain a high chemical ordering, numerous studies have focused on the influence of different seed layers [45], film thickness [46], Fe-Pt composition [47] and annealing on their structure and magnetic properties [48]. Below a certain film thickness, FePt films show an island-like morphology. Several reports have successfully made FePt islands with high coercivity (over 100 kOe at 50K). However, most of the reports by now only have managed to fabricate islands with the size of 50-100 nm (See Figure 8). This size is too large for the ultra-high density magnetic recording.

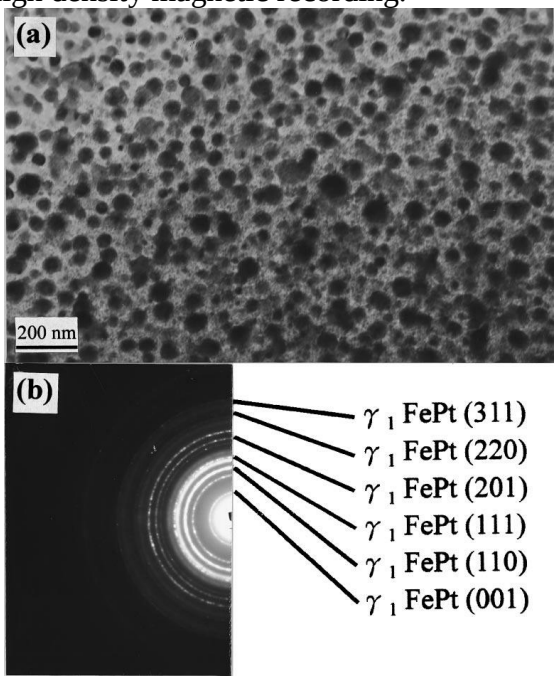

Figure 7 (a) Bright-field image and (b) electron diffraction pattern of $(FePt)_{70}$–$(Si_3N_4)_{30}$ film[36]

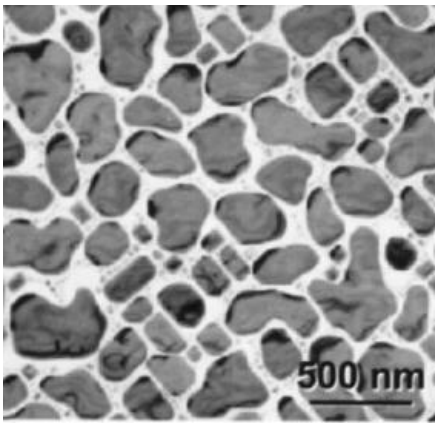

Figure 8 FePt islands with high coercivity[42]

Another popular fabrication method is the solution-phase synthesis via thermal decomposition of $Fe(CO)_5$ and reduction of $Pt(acac)_2$. Figure 9 [16] shows the synthetic chemistry of FePt nanoparticles. In a typical fabrication process (shown in Figure 10 [49]), $Pt(acac)_2$, dioctyl ether and 1,2-hexadecanediol were firstly mixed in a three-neck flask and stirred using a magnetic stirring bar. The mixture is heated to 100℃ in an atmosphere of N_2 flow to remove oxygen and moisture. After oleic acid and oleylamine were added, the mixture was further heated to reflux temperature (297℃). The refluxing lasted for 30 min and the heating source was removed. The black product is precipitated by adding ethanol and separated by centrifugation.

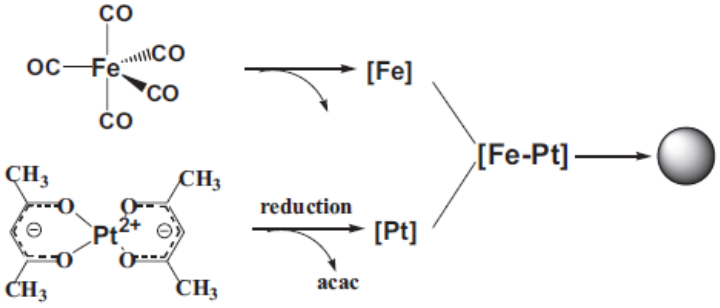

Figure 9 Schematic illustration of FePt nanoparticle formation[16]

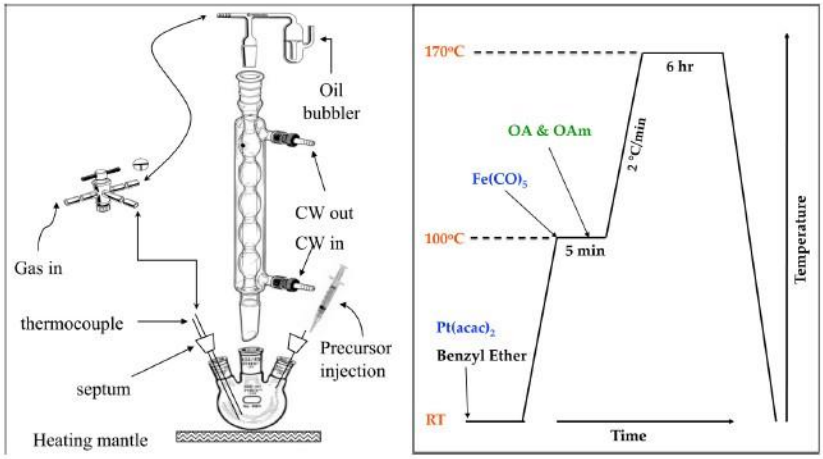

Figure 10 A typical solution-phase synthesis of FePt nanoparticles[49].

The main advantages of this fabrication method are the ease to gain monodisperse FePt nanoparticles and the easy control of particle size and shape. Sun et al. [15] successfully fabricated monodisperse FePt nanoparticles with the size of 6 nm (shown in Figure 11). The size of the FePt nanoparticles can be controlled by the molar ratio of the stabilizers to $Pt(acac)_2$ and heating conditions. The shape of the FePt nanoparticles is controlled by sequential addition of the surfactants. However, the as-made FePt nanoparticles prepared by this method are also in the magnetically soft fcc phase. Thermal annealing is required to make the transformation from fcc phase to $L1_0$ structure to obtain desired hard magnetic properties. The serious side effect of the annealing is the deterioration of the monodispersity of the nanoparticles. Previous studies by using the technique of in-situ TEM (shown in Figure 12) [50] and XRD [51] revealed the coalescence of the FePt particles annealed at 600℃ or above. Plenty of studies have been done to solve this problem. S. Momose et al [52] embedded the FePt nanoparticles in thick organic matrices, H. Zeng, C. Liu et al [53, 54] put the

FePt nanoparticles in robust inorganic matices. M. Mizuno et al assembled the FePt nanoparticles on the surface of –Si-O- network to limit the mobility of the particles at high temperature. Another solution is to dope FePt with another element (Cu, Ag, Au etc.) to lower the structure transformation temperature. For example, both the experimental results and first-principle band calculations revealed that the substitution of Cu in Fe site which enhances the free energy between the ordered and disordered phase and increases the driving force in the disorder-order transformation.

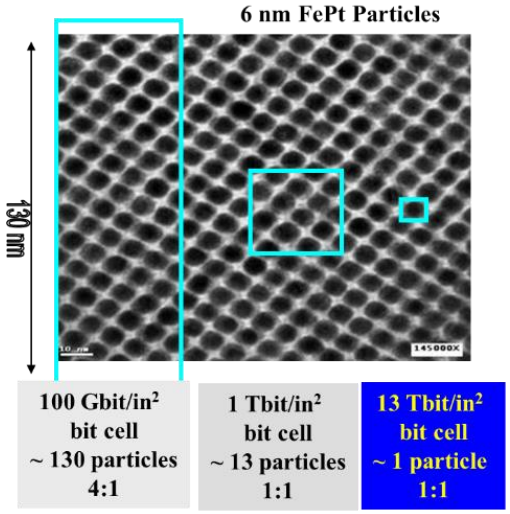

Figure 11 Monodisperse FePt nanoparticles with the particle size of 6 nm[15]

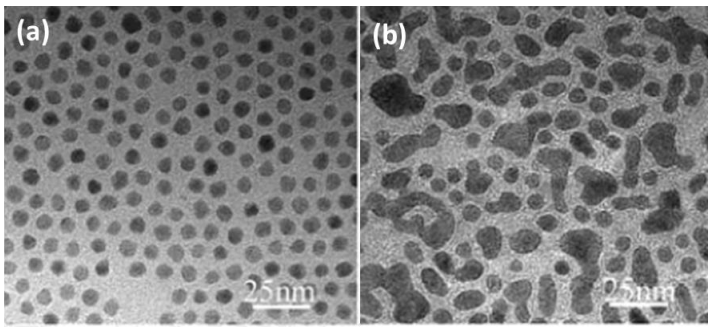

Figure 12 FePt nanoparticles (a) before annealing and (b) after annealing

Summarizing from the above fabrication methods, there is a need to explore a fabrication method to directly prepare FePt nanoparticles in $L1_0$ structure with uniform size distribution. In this thesis, a special layered crystal precursor $[Fe(H_2O)_6]PtCl_6$ was used and applied in new fabrication approaches.

Chapter 3

THEORETICAL BACKGROUND

3.1 Introduction to magnetism

The first magnet was discovered by Thales of Miletus in a city called Magnesia around 500 B.C. The early magnetic device was a compass named “south pointer” and was used for geomancy in China at the beginning of our era. It was carved in the shape of a Chinese spoon and it turns to align its handle with the earth’s magnetic field. Despite of such an early discovery and application of magnetism, it was not until the mid-1920s that humans realized that the magnetic effect comes from the electrons rotating around the nuclei and their own axis (orbital magnetic moment and spins).

3.2 Origin of Magnetism

Regardless of phase or atomic composition, all materials exhibit magnetic properties which arise from the electron clouds of each atom and the way they interact with the surrounding environment. According to response to an applied magnetic field, magnetism can be classified as: diamagnetism, paramagnetism, ferromagnetism, antiferromagnetism and ferrimagnetism.

Inside each atom, the electron possesses a spin which is equivalent to a magnetic moment. According to Pauli’s principle, there are only two electrons with opposite spins allowed for each energy state. For atoms with closed shells of electrons, the spin magnetism is self-cancelled. Once a magnetic field is applied, a magnetic flux

is induced which is countered by the external field. This is the origin of a **diamagnetic** material whose magnetization is antiparallel to the direction of the applied field.

If there are unpaired spins inside some atomic shells, the atom will have a net magnetic moment. But the magnetic moments cannot be aligned perfectly with the magnetic field because of the thermal fluctuation. When the magnetic field is removed, the magnetic moments become random again. This behavior is called **paramagnetism**.

Ferromagnets consist of spontaneously magnetized magnetic domains which are small regions inside the material containing parallel magnetic moments. The spontaneous magnetization is due to unpaired electrons from partially filled electronic shells. The strong exchange interaction makes these spins to be aligned parallel. As a magnetic field is applied, the total magnetization will increase from zero to saturation. However, if the magnetic field is removed, the magnetization will not become zero. Instead, the material exhibit a behavior called hysteresis. Ferromagnets become paramagnets above a certain temperature which is called Curie temperature, T_C.

In an **antiferromagnetic** material, there is an ordered arrangement of antiparallel aligned spins on different sublattices, which causes a zero net spontaneous magnetization. At the lower temperature, an applied external magnetic field faces strong opposition because of the interaction between the spins, causing a decrease of the susceptibility with temperature. However, above a certain temperature which is called Neel temperature, T_N, the antiparallel alignment of magnetic moments will vanish and become totally random. The antiferromagnetic material then will behave like a paramagnet.

To some extent, **ferrimagnetism** resembles the behavior of both ferromagnetism and antiferromagnetism. In ferrimagnetic materials, the two interpenetrating lattices have unequal antiparallel magnetizations which results in a total non-zero, spontaneous magnetization. Similar to ferromagnets, the spin arrangement will become random above the Curie temperature and ferrimagnets become paramagnetic.

3.3 Hysteresis loops

The magnetic property of ferromagnetic materials can be demonstrated by the M-H curve which is also called the hysteresis loop as is shown in Figure 13.

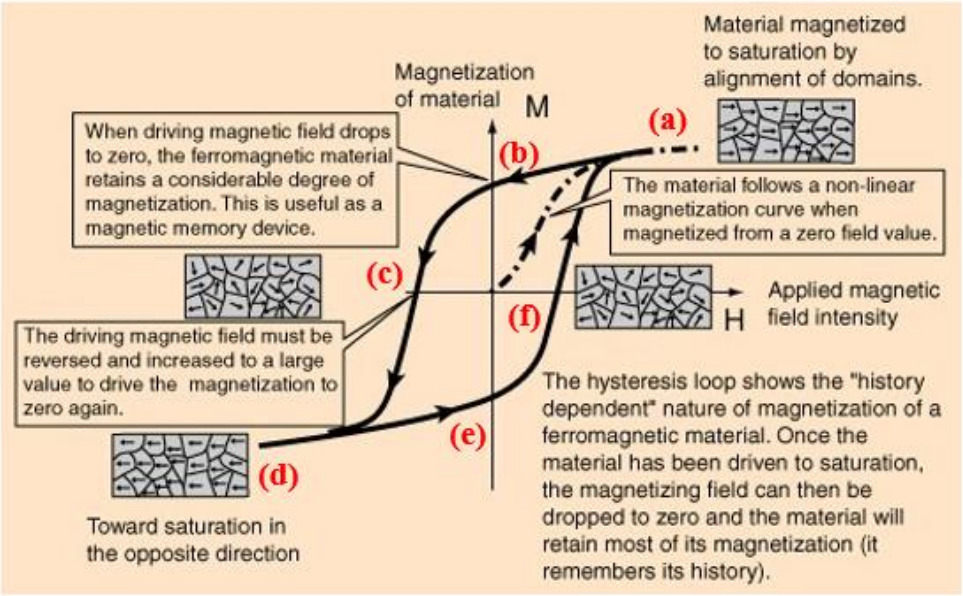

Figure 13 Typical hysteresis loop of a ferromagnet[55]

When an external magnetic field is applied to a ferromagnetic material which has never been magnetized before, the magnetization will follow the dash curve (known as the initial curve) as H increases. At high fields, when all the magnetic

domains are aligned as is shown at point (a), the material reaches its saturation magnetization. Further increasing the external magnetic field will have little effect on the magnetization value.

As H is reduced to zero, the magnetization value will move from (a) to (b) at which point the magnetization value of the material is not zero. This value is called remanence or remanent magnetization. To make the magnetization of the ferromagnetic material become zero, an external magnetic field in the opposite direction is needed (point (c)). This value of H is called coercivity or coercive field. With the increasing of magnetizing force in the opposite direction, the material will finally reach saturation in the opposite direction (point (d)). From point (d) to point (a), going through point (e) and (f), the material behaves in a similar procedure like in the upper part of the curve. At point (e), it has remanence and with the same coercive field (point (f)), the magnetization becomes zero. A whole cycle of hysteresis loop should be symmetric.

3.4 Exchange energy

According to Pauli's exclusion principle, electrons in neighboring orbitals cannot share the same orbital with the same spin (to avoid having the same quantum numbers). Electronic spins will be either aligned parallel or antiparallel according to the interaction. This exchange energy leads to the spontaneous magnetization and is a quantum mechanics explanation of magnetization. For a pair of spins, the exchange energy density is given by:

$$E_{ex} = -2J_{ex}S_i \cdot S_j$$

where J_{ex} is the exchange integral and S_i and S_j are spin vectors. The specific crystal structure determines the value and sign of the exchange integral. Exchange energy is at its minimum when the electronic spins are aligned parallel or antiparallel. For ferromagnetic materials, the exchange integral is positive which means the parallel alignment of the spins is the minimum energy state. For antiferromagnetic materials, the exchange integral is negative which means the antiparallel alignment of the spins is the minimum energy state [56].

3.5 Magnetic anisotropy

The theory of ferromagnetism and ferrimagnetism is based on the electronic exchange force which is so strong that these materials are spontaneously magnetized even without an applied field. There are small sub volumes inside the ferromagnets which are called **domains**. Each domain is spontaneously magnetized to saturation but the direction of magnetization varies from domain to domain (is random). The net vector sum of all the domains produces a zero total magnetization at zero applied field. The dependence of the magnetic properties on a preferred direction is called magnetic anisotropy. There are several different types of anisotropy which are listed in Table 1:

Table 1 Types and origin of anisotropy

Types of anisotropy	Origin of anisotrpy
Magnetocrystalline	crystal structure
Stress	applied or residual stresses
Shape	grain shape

3.5.1 Magnetocrystalline anisotropy

The crystal structure usually dominates the magnetic energy for spherical particles with low saturation magnetization or single-domain particles through the **magnetocrystalline anisotropy**. Magnetocrystalline anisotropy comes from the spin-orbit coupling. The spins are held in a specific direction by the strong coupling between the spin and orbit which makes the switching of the magnetization difficult. The crystallographic directions along which magnetocrystalline energy is at a minimum are called easy directions of magnetization.

For Fe, which has a body-centered cubic structure, [100] are the easy directions and [110] and [111] are hard directions. As is shown in Figure 14, the Fe atoms arrange on the cube corners and at each cube center. The [100] directions are along a cube edge, the [110] directions along a face diagonal and the [111] directions along a cube body diagonal. Cobalt has a hexagonal closed-packed (hcp) structure which has only one easy axis leading to uniaxial anisotropy. When the magnetization is along the easy axis, the magnetocrystalline anisotropy energy is a minimum. When the magnetization is at 90 °to the easy axis, the magnetocrystalline anisotropy energy is a maximum.

Compared to cubic materials, the magnetocrystalline anisotropy energy is much higher in uniaxial materials. The anisotropy energy is given by:

$$E_a = K_0 + K_1 \sin^2 \theta + K_2 \sin^4 \theta + \cdots$$

Where K_i is material-dependent anisotropy constant and θ is the angle between the easy axis and the magnetization. K_0 is the change in energy due to moment rotations and exists in all materials. Thus it can be ignored. For a given crystal class such as cubic structures, direction cosines (α_i) related to the cube edges are used to define the direction of magnetization. The anisotropy energy is then given by:

$$E_a = K_1(\alpha_1^2\alpha_2^2 + \alpha_2^2\alpha_3^2 + \alpha_1^2\alpha_3^2) + K_2(\alpha_1^2\alpha_2^2\alpha_3^2) + \cdots$$

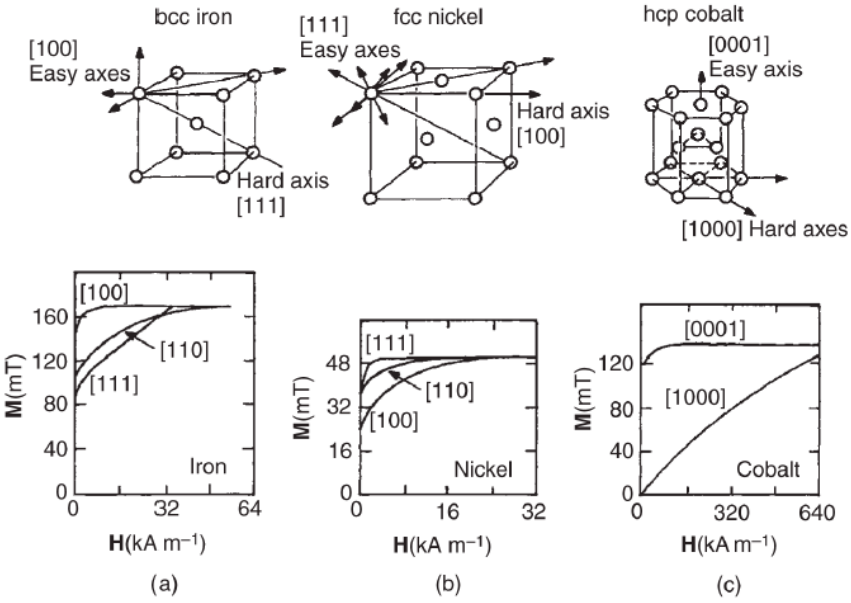

Figure 14 The crystal structure and magnetization loops For Fe, Ni and Co, demonstrating the anisotropic nature of the magnetization process[13]

3.5.2 Stress anisotropy

Stress anisotropy is caused by the stress applied to a magnetic material. The magnetic energy density due to the application of stress to a crystal can be given by:

$$E_\sigma = \frac{3}{2}\bar{\lambda}\sigma \sin^2\theta$$

Where λ is the magnetorestriction constant, σ is the stress and θ is the angle between the stress and the easy axis. This effect can be usually seen in films due to lattice mismatch between the magnetic thin film and the substrate.

3.5.3 Shape anisotropy

The third type of anisotropy is due to the shape of the material. Magnetic charges or poles will be generated by a magnetized material at the surface. This

surface charge is another source of a magnetic field, called demagnetizing field. The direction of the demagnetizing field is opposite to the direction of magnetization field (See Figure 15).

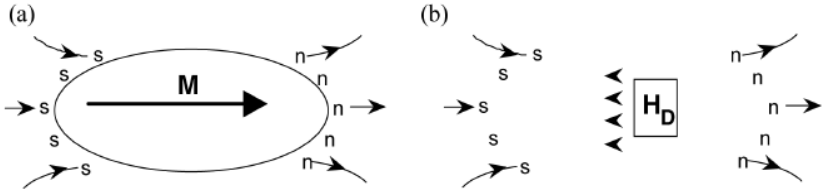

Figure 15 (a) Magnetization produces apparent surface pole distribution (b) Demagnetizing field due to apparent surface pole distribution

Take a long thin needle shaped grain for example, if the magnetization is along the long axis, the demagnetization field will be smaller. This makes the long axis an easy magnetization axis. The magnitude of shape anisotropy is dependent on the saturation magnetization and it is much smaller than magnetocrystalline anisotropy.

3.6 Magnetism in small particles

Especially for small particles, the coercivity varies depending on the different range of particle size. As is shown in Figure 16, when the particle size is above a certain size D_s, known as the single domain particle size (different according to different materials), the nanoparticles have multi-domain inside one single particle. Domain wall motion changes the magnetization. The dependence of coercivity on particle size for some, but not all, materials is given approximately by

$$H_c = a + \frac{b}{D}$$

Where a, b are constants and D is the diameter of the particle.

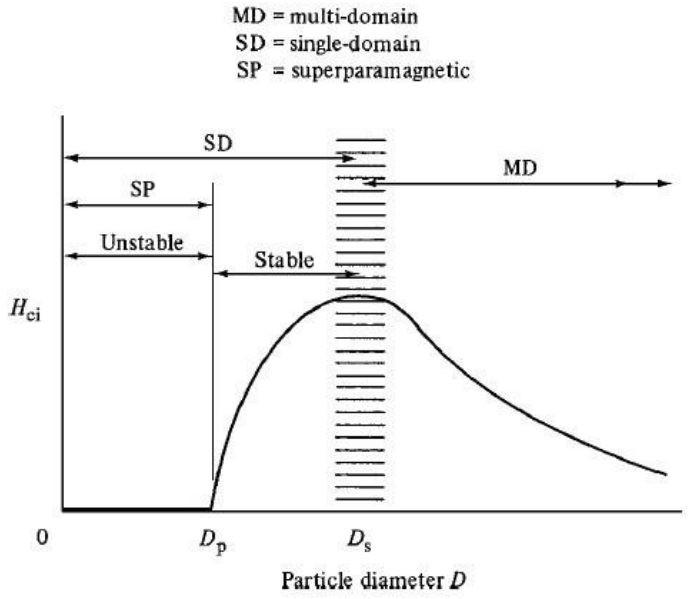

Figure 16 Dependence of intrinsic coercivity H_c on particle diameter D

The particles become single domain below the critical diameter. The maximum of coercivity can be reached in this region. When the particle size decreases below D_s, the coercivity starts decreasing with decreasing particle size.

Below the superparamagnetic size D_p, the coercivity is zero because of the thermal fluctuation which is strong enough for a spontaneous demagnetization. This phenomenon is called superparamagnetism[57]. To be specific for FePt, the large magnetic anisotropy energy of 7×10^7 erg/cc[58] [35] allows the particle size to be as small as 2.8 nm to overcome the superparamagnetic limit.

3.7 Thermal effects

For a single domain particle with uniaxial anisotropy, the relaxation of magnetization can be described by an Arrhenius-type law [59]:

$$\mathrm{M}(t) = M_0 exp\left(-\frac{t}{\tau}\right)$$

Where M_0 is the initial magnetization and τ is the characteristic relaxation time. The relaxation time is a function of the energy barrier and the temperature:

$$\tau = \tau_0 exp\left(\frac{\Delta E}{k_B T}\right) = \tau_0 exp\left(\frac{KV}{k_B T}\right)$$

Where k_B is the Boltzmann constant, and τ_0 is inversely proportional to the jump attempt frequency of the particle magnetic moment between the opposite directions of the magnetization easy-axis; τ_0 can be determined by experimental data and theoretical calculation. Reported values of τ_0 are in the range of 10^{-9}~10^{-10} s.

For a specific material, if the characteristic measuring time τ_m (the time window) $\gg \tau$, the relaxation is faster than the magnetization orientation observed in this time window, which allows the system to reach thermodynamic equilibrium. These nanoparticles are considered to be superparamagnetic. On the other hand, if $\tau_m \ll \tau$, the system relaxation proceeds very slowly. The nanoparticles are in so-called blocked regime. The temperature that divides these two regimes is called blocking temperature T_B. T_B is related to the energy barrier and increases as the particle size increases.

3.8 Superparamagnetism

As describe above, the magnetization as a function of time can be given by:

$$\mathrm{M}(t) = M_0 exp\left(-\frac{t}{\tau}\right)$$

The relaxation time is the time required for the remanence to decay to $1/e$ of M_0. τ depends on the competition between magnetic anisotropy energy and thermal energy. With zero applied field:

$$\tau = \tau_0 exp\left(\frac{KV}{k_B T}\right)$$

For a typical measurement time of 100 sec,

$$25k_BT = KV$$

Superparamagnetism occurs when the material is composed of very small particles (1-10 nm). In a superparamagnetism, the thermal energy is sufficient to change the direction of magnetization of the entire crystallite even though the temperature is below the Curie or Neel temperature. The material behaves like paramagnetic materials but the individual atom is independently influenced by an external magnetic field. Compared to paramagnets, superparamagnets have larger value of magnetic moment because the magnetic moment of the entire crystallite tends to align with the magnetic field.

There exists a critical particle size smaller than which the particles are all in the superparamagnetic regime. The critical particle size for superparamagnetism is directly proportional to the temperature. If the particles has a grain size distribution, as the temperature increases, more particles become superparamagnetic. Superparamagnetism can be verified by plotting of M/M_s verses H/T. Above the blocking temperature curves must superimpose [60].

3.9 Law of approach to saturation

In the high-field region, domain rotation is the predominant effect. The relation between M and H in this region is called the **law of approach to saturation** and is given by [61]:

$$\mathrm{M} = M_s\left(1 - \frac{a}{H} - \frac{b}{H^2} - \frac{c}{H^3} - \cdots\right) + \kappa H$$

The first term a/H can be explained as a result of stress field caused by dislocation, non-magnetic inclusions or voids. This term is usually not included in the calculation. b and c are interpreted by the crystal anisotropy and related to the

saturation magnetization and anisotropy constant of the material according to the following expressions for uniaxial materials [62]:

$$\mathrm{b} = \frac{4}{15}\left(1 + \frac{16K_2}{7K_1} + \cdots\right)\frac{K_1^2}{M_s^2}$$

$$\mathrm{c} = \frac{16}{105}\left(1 + \frac{8K_2}{3K_1} + \cdots\right)\frac{K_1^3}{M_s^3}$$

In the case of strong uniaxial materials, $K_2 \approx 0$

$$\mathrm{b} = \frac{4}{15}\frac{K_1^2}{M_s^2}$$

$$\mathrm{c} = \frac{16}{105}\frac{K_1^3}{M_s^3}$$

The last term κH represents the field-induced increase in the spontaneous magnetization of the domains and κ is called the high field susceptibility. At temperature below Curie temperature, this term is very small and can be neglected.

Chapter 4

CHARACTERIZATION TECHNIQUES

In this thesis, different techniques were used to characterize the properties of the particles. Transmission electron microscopy (TEM) was used to characterize the size and crystal structure of the nanoparticles through electron diffraction. Scanning electron microscopy (SEM) was used to determine the surface morphology of the particles. Structural studies were carried out by X-ray diffraction (XRD) measurements. Vibrating sample magnetometer and physical property measurement system (PPMS) were employed for the magnetic characterization of the nanoparticles.

4.1 Electron microscopy

Electron microscopy is a very important technique to analyze the morphology, size and structure of nanoparticles. Electron microscopes generate images with much higher resolution than light microscopes due to short wavelengths of the accelerated electrons. The resolution of transmission electron microscopes can be below angstrom if lens aberrations can be minimized. Two main different types of electron microscope, TEM and SEM, are commonly used. SEM is mostly used to characterize the surface and subsurface of nanostructured systems. TEM is used for the imaging the internal microstructure of ultrathin specimens and nanoparticles.

4.1.1 Electron-Specimen Interactions

Figure 17(a) demonstrates various signals generated by the electron-specimen interactions in the SEM. Different interaction volumes and penetration depths which

generate different signals are calculated. The interaction volume is the volume that 95% of the electrons are brought to rest by the scattering and it has a typical teardrop shape as is shown in Figure 17(a). The penetration depth and lateral width are roughly proportional to V^2 and $V^{3/2}$, where V is the accelerating voltage. High atomic number materials will have decreased penetration depths and increased lateral spread compared with lower atomic number materials.

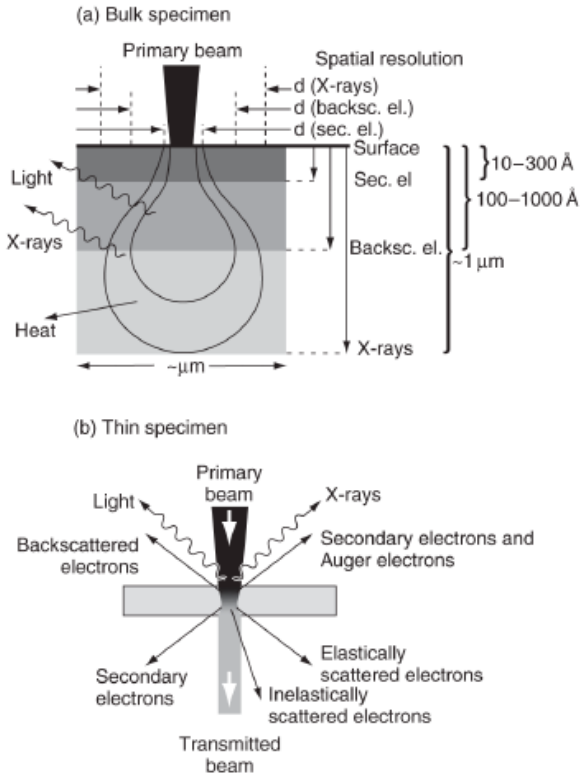

Figure 17 Electron-specimen interactions in (a) a thick specimen and (b) a thin specimen [63]

Figure 17(b) shows the signals generated by TEM imaging process in thin specimens. The transmitted beam (unscattered electrons), the elastically and

inelastically scattered electrons are usually examined for thin specimens. Transmitted beam is composed of incident electrons transmitted through the thin specimen without any interaction. Thicker specimens will have fewer transmitted electrons and weaker transmitted beam so that the images look darker. For thinner specimens, more transmitted electrons will go through the specimen and stronger beam can be detected so that the images are brighter. The elastically scattered electrons are the electrons that scattered by the specimen atoms and there is no loss of energy. These electrons follow Bragg's law $\lambda = 2\mathrm{d}\sin\theta$ where λ is the wavelength, d is the space between the atoms in the specimen and θ is the angle of scattering. All the electrons scattered by the same atomic spacing will have the same angle. These electrons can be collated using magnetic lenses to form a pattern of spots. Each spot corresponds to a specific plane giving the information about the orientation, atomic arrangements and corresponding phases. Inelastically scattered electrons are the electrons that interact with the specimen atoms with an energy loss. These electrons can be used by the ways listed below:

Kikuchi pattern: patterns of alternating light and dark lines that are formed by inelastic scattering interactions. Kikuchi pattern is related to the atomic spacing and the width of Kikuchi pattern is inversely proportional to atomic spacing.

Electron Energy Loss Spectroscopy (EELS): the loss of energy of the inelastic scattered electrons is characteristic of involved elements. Therefore, EELS can be used to achieve the information of composition and bond.

4.1.2 Transmission Electron Microscopy

As is shown in Figure 18 [63], similar to a transmission light microscope, TEM has the following five parts along the optical path which are light source,

condenser lens, specimen stage, objective lens and projector lens. However, instead of using a visible light and glass lenses, TEM uses an electron beam and electromagnetic lenses. Meanwhile, TEM has more intermediate lenses and more apertures (e.g. selected area aperture). A typical TEM constitutes of the following parts: two or three condenser lenses to focus the electron beam on the sample, an objective lens to form the diffraction in the back focal plane and the image of the sample in the image plane and some intermediate lenses to magnify the image or the diffraction pattern on the screen. A vacuum environment is need due to the use of electron beam for TEM to avoid collisions between high-energy electrons and air molecules which will significantly absorb electron energy.

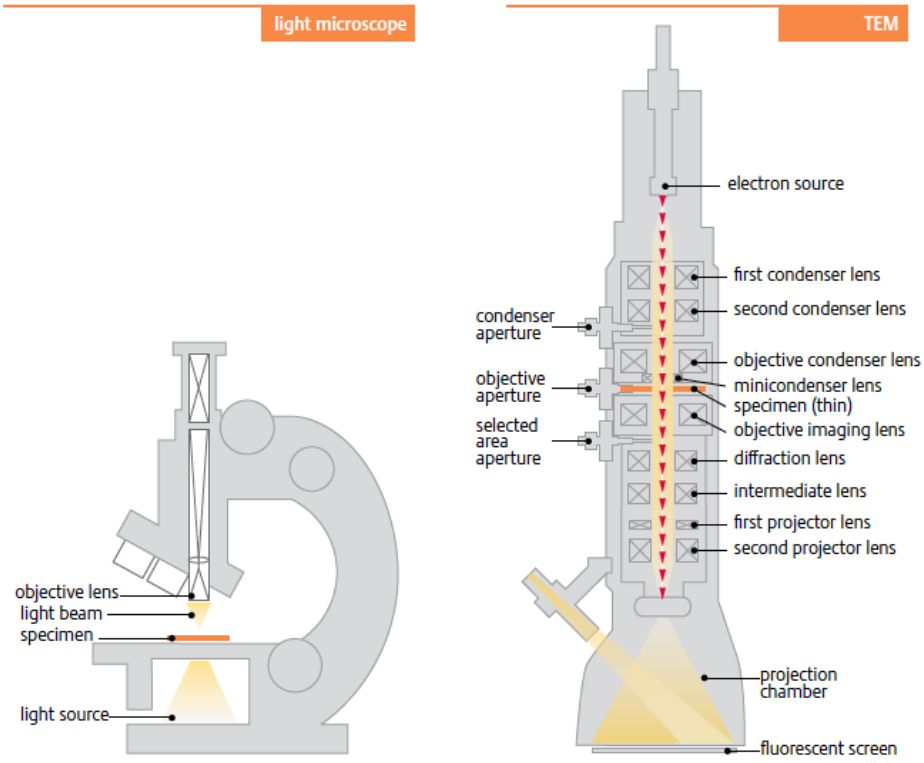

Figure 18 Light and transmission electron microscopes [63].

There are two most commonly used imaging modes in TEM: **bright field (BF) mode and selected area electron diffraction (SAED) mode**. An objective diaphragm is inserted in the back focal plane to select the transmitted beam in order to obtain an amplitude-contrasted image (shown in Figure 19(a)). The crystal parts which are in Bragg's direction will show dark in the image and the crystal parts which are not in Bragg's direction and the amorphous part will show bright in the image. This image mode is called bright field mode. For the SAED mode, a selected area diaphragm (shown in Figure 19(b)) is used to select only part of the specimen (e.g. a particle or a precipitate). Crystal structure information can be obtained from SAED image.

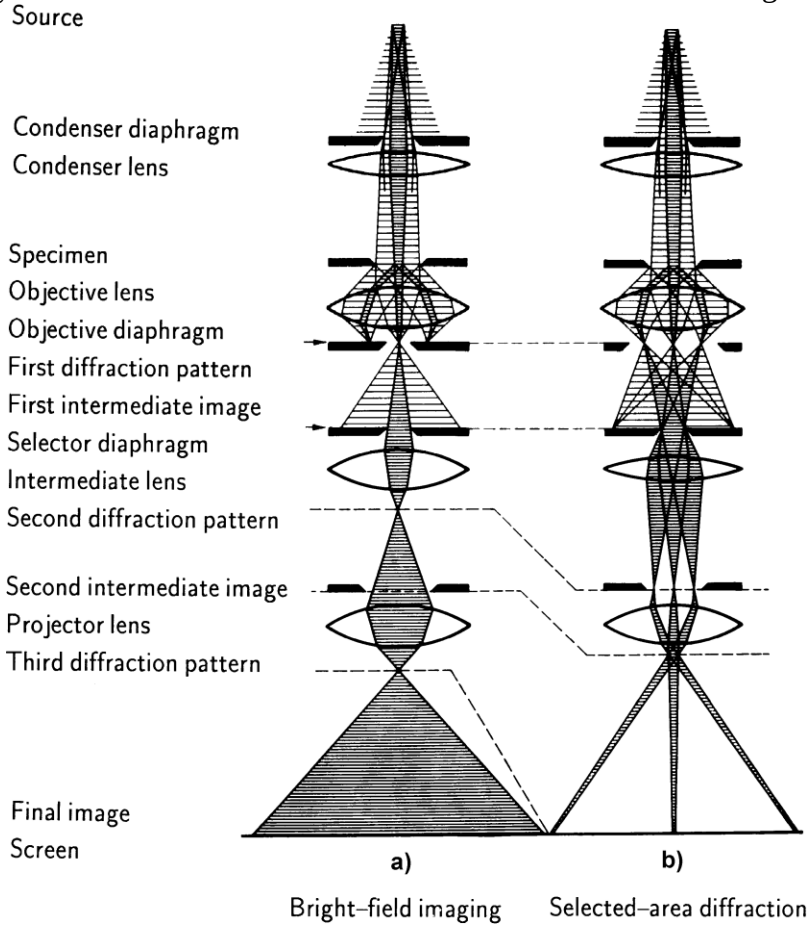

Figure 19 (a) The bright-field mode and (b) selected area electron diffraction (SAED) mode [63]

4.1.3 Scanning electron microscopy

The scanning electron microscope (SEM) examines microscopic structure by scanning the surface of materials and is the most widely used electron microscope. An SEM image is obtained by the scanning over the surface area of a specimen by a focused electron beam.

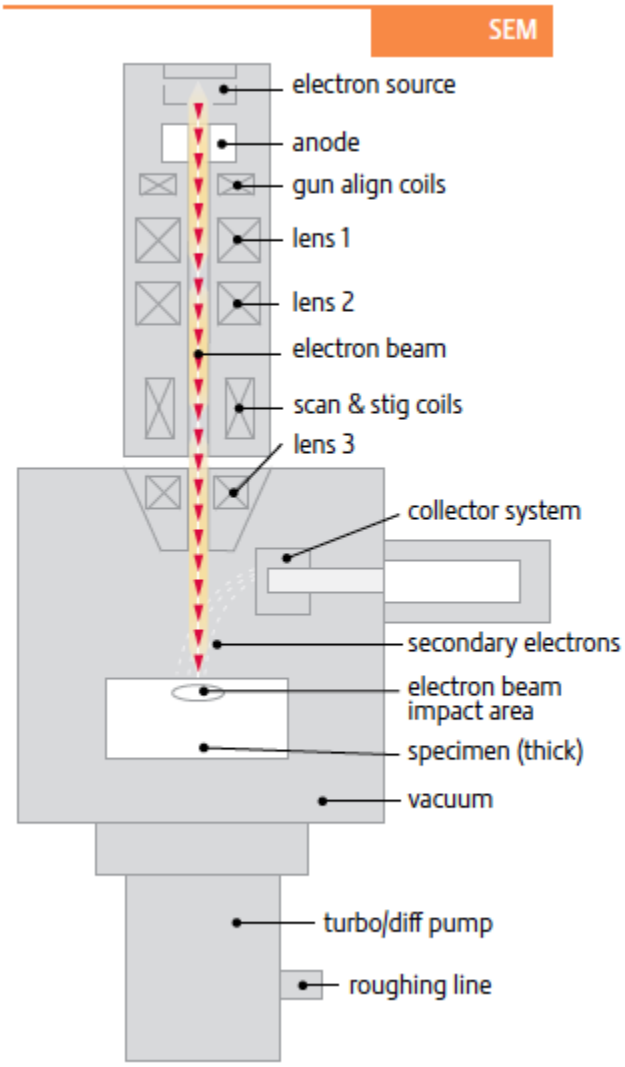

Figure 20 The SEM microscope [63]

As is shown in Figure 20, there are several electromagnetic lenses, including condenser lenses and one objective lens, in the optical path of SEM. Different from TEM, the electromagnetic lenses are used for electron probe formation in SEM instead of image formation directly. In the optical path, the electron beam crossover diameter is reduced by the two condense lenses and then is focused by the objective lens with a

diameter of nanometer scale. There is a deflection system inside the SEM which moves the scanning probe over the specimen surface along a line. The detector collects the electrons emitted by the specimen and then the signal is amplified, and used to reconstruct an image [64].

4.1.4 Energy Dispersive X-ray Spectroscopy

One important issue during the characterization of the specimen is the element composition. The energy disperse X-ray spectroscopy (EDS) is the commonly used technique to determine the element composition of the phase. In the discussion of electron-specimen interaction part, we know that inelastic interactions between electrons and specimen generate different kinds of signals: secondary electrons, Auger electrons, X-rays, light and lattice vibrations. Among all these signals, X-ray relates to the two energy level difference of the electron cloud of an atom (K, L.). Once this energy is quantified, we can characterize the specific elements. There are two parts in the EDS spectrum one is the background produced by the Bremsstrahlung X-rays and the other is the characteristic peaks of the specific elements. If the peaks do not overlap, the identification is straightforward except the element of carbon.

4.2 X-ray diffraction

Crystals are made of an orderly arrangement of planes of atoms. The discovery of X-ray by Conrad Roentgen in 1895 has given the scientist a very powerful tool to further investigate the structure of crystals.

When the X-ray goes into the atom planes, it will interact with the atoms behaving like waves reflected by the atom planes. This procedure is shown in Figure 21. Consider two X-ray beams enter the crystal and θ is the angle between the beam

and the atom plane; d is the spacing between the atomic planes. Ray 1 reflects off the upper atomic plane with the same angle θ (between the beam and the atom plane). Ray 2 has the similar reflect with the lower atomic plane. If the distance 2a is equal to an integral number of wavelength, Rays 1 and 2 will have constructive interference. On the other hand, if the distance 2a is not equal to an integral number of wavelength, Rays 1 and 2 will cancel each other. Therefore, the condition for constructive interference is:

$$n\lambda = 2a = 2d\sin\theta$$

This is Bragg's law in X-ray diffraction.

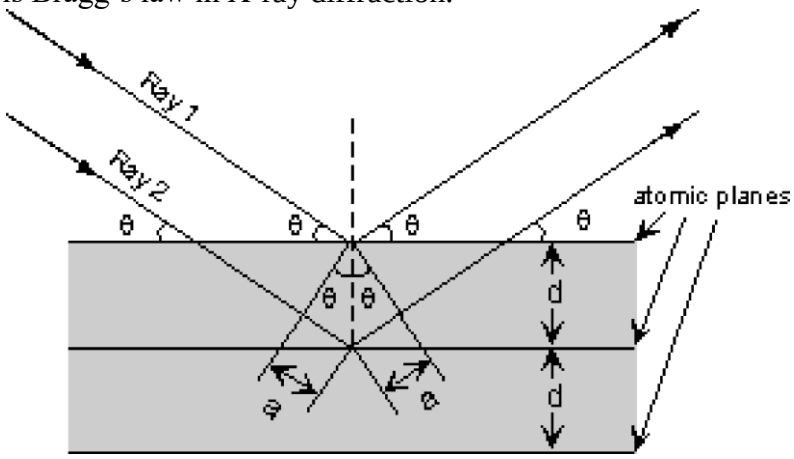

Figure 21 Scheme of the diffraction geometry of X-ray from atomic planes [65]

Experimentally, if we know the wavelength of the X-ray λ and measuring θ we can know the atom plane spacing d. By knowing d, the crystal structure and phase can be identified.

Another application of XRD is to estimate the particle size by using Sherrer's formula [66]:

$$t = \frac{0.9\lambda}{\beta\cos\theta}$$

where β is the half maximum width of the peak in radians, λ is the wavelength of the X-ray and θ is the corresponding constructive interference angle.

4.3 Vibrating sample magnetometer

The vibrating sample magnetometer (VSM) is based on Faraday's law [49]. It states that a field will be generated in a coil when there is a change in the flux. For a coil with n turns:

$$\mathrm{V} = -\mathrm{na}\frac{dB}{dt}$$

If the coil is in a magnetic field ($\mathrm{B} = \mu_0 H$), after we put a sample with a magnetization of M, the field will be:

$$\mathrm{B} = \mu_0(H + M)$$

Then the corresponding flux change is:

$$\Delta\mathrm{B} = \mu_0 M$$

Combining the above two equations, we get:

$$\mathrm{Vdt} = -\mathrm{na}\mu\mathrm{M}$$

Therefore, the output signal of the coil is proportional to the magnetization.

As is shown in Figure 22, during a measurement of VSM, we put the magnetized sample in a coil and subject it to a sinusoidal motion with a frequency of ν. The corresponding voltage induced from the stationary pick-up coils. The electrical signals of the pick-up foil also have a frequency of ν, and the intensity of the output signal is proportional to the magnetization of the sample.

In this thesis, we use a Quantum Design's VersaLab VSM, is a cryogen-free cryocooler-based VSM with a sensitivity of better than10^{-6} emu. This 3-Tesla VSM works under a temperature range of 50 to 400 K.

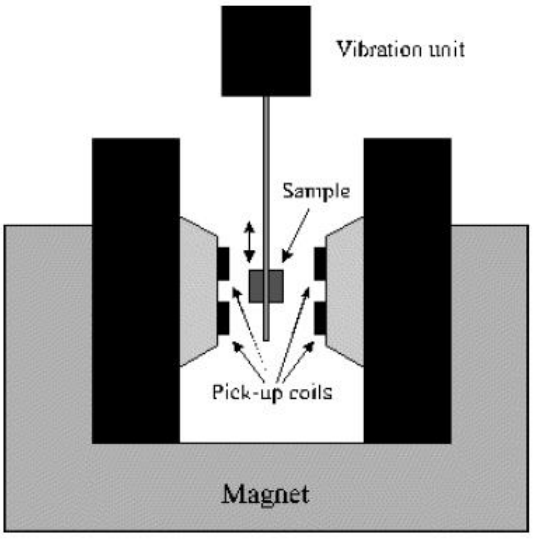

Figure 22 Schematic diagram of a Vibrating Sample Magnetometer [49]

4.4 Physical Property Measurement System

The Physical Property Measurement System (PPMS) used in this thesis is from Quantum Design. The measuring theory is the same as what we discussed in the VSM part. Different from the low magnetic field of 3 Telsa, the Quantum Design PPMS consists of a 9 Tesla superconducting magnet in a helium dewar with sample temperature range of 1.9-400K (shown in Figure 23). During the measuring procedure, the samples are put in a sample rod and the magnetic response signal is measured by the two pick-up coil. This machine has a sensitivity around 10^{-5} emu.

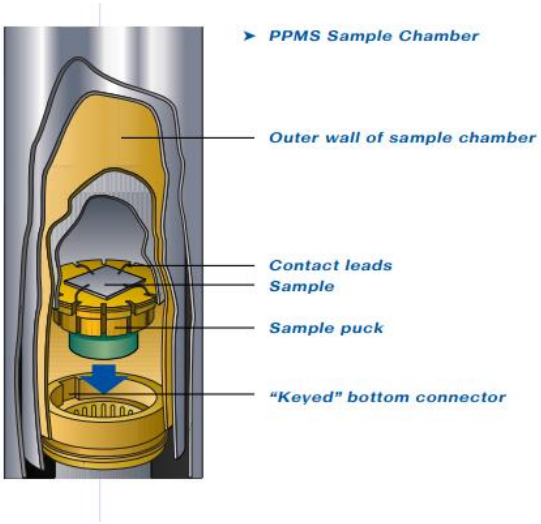

Figure 23 Schematic diagram of Physical Property Measurement System [67]

Chapter 5

A LOW-TEMPERATURE AND SOLVENT-FREE CHEMICAL SYNTHESIS FEPT NANOPARTICLES BY BALL MILLING

5.1 Introduction

Magnetic nanoparticles have been attracting a great attention recently, due to their potential application in different fields such as magnetic filters [68], data storage[69], permanent magnetic nanocomposites[70, 71] and biomedicine.[72] Magnetically soft nanoparticles are currently applied for cancer treatment as a targeted drug carrier and for cancer detection as a contrast enhancer (e.g. MRI)[73]. [22, 73].

As mentioned before, in the FePt $L1_0$ alloy, a face centered tetragonal (fct) structure is formed by two different atoms (big atoms such as Pt or Pd and smaller ferromagnetic atoms such as Fe or Co) occupying alternatively the lattice sites. Due to spin-orbital coupling between the alternate planes of the metals, the $L1_0$ structure has a high magnetocrystalline anisotropy. For this reason such materials have a great importance in the magnetic applications. In recent years, $L1_0$ FePt nanoparticles are considered as one of the most promising candidates for future magnetic recording media with areal density larger than 1 Tbit/in^2 due to their large magnetic anisotropy energy of 7×10^7 erg/cc[58] [35] (which allows stable ferromagnetic particles with size as small as 2.8 nm), their resistance to oxidization and their stability at room temperature.[43]

Fabrication of well-separated, single crystal nanoparticles with moderate coercivity plays a key role in the development of high density recording media.

Currently, there are two major methods for fabricating FePt nanoparticles. One method is to deposit films or nano-islands of FePt through physical vapor deposition (PVD) techniques such as sputtering. Usually substrates with certain type of texture, for example MgO (001), are used to obtain an epitaxial growth of the FePt films or islands [43, 44, 74]. However, the FePt islands reported with a high coercivity usually have a particle size as large as 50-100 nm which is certainly undesirable for magnetic recording. Also, to get the $L1_0$ structure, very high substrate temperatures up to 800 ℃ are used which are not environmental friendly. Another very popular method is the chemical synthesis of FePt nanoparticles based on the reduction of mixed metal salts ($Fe(CO)_5$ and $Pt(acac)_2$) in the presence of a long chain carboxylic acid and primary amines in organic solvent which was first reported by Sun et al [15]. To obtain nanoparticles, organic solvents and surfactants are used. This together with the use of the dangerous and hazardous compound $Fe(CO)_5$ make this synthesis not environmental friendly. Furthermore, the as-made FePt nanoparticles are in the fcc phase and more energy (annealing higher than 650 ℃) is needed for the phase transformation from the fcc to fct which usually introduces uncontrolled agglomeration and sintering of the particles [16, 75, 76]. For this reason, many attempts have been made in order to decrease the annealing temperature required for the phase transformation. Nakaya et al. [77] reported a phase transformation temperature of 300 ℃ under pure H_2 environment. Another method reported is the use of metals as catalysts for the fcc-fct transformation. [78] Other new chemical routes for direct synthesis of $L1_0$ FePt nanoparticles have been proposed [79, 80], but the fraction of the ordered phase obtained is usually small [81].

A direct chemical synthesis of FePt nanoparticles in $L1_0$ phase was reported in reference [82]. In this thesis, we report a new environmental friendly approach for the direct synthesis of FePt nanoparticles, starting from the same polycrystalline molecular compound $[Fe(H_2O)_6]PtCl_6$, in which the Fe and Pt atoms are arranged on alternating planes resembling the order they have in the fct FePt structure. Mixtures of this compound with NaCl were milled by planetary ball milling and then the mixture was annealed under an atmosphere of forming gas (5% H_2 and 95% Ar) at 400 ℃ for 2h. After washing the annealed products, $L1_0$ FePt nanoparticles with controlled size were obtained. Similar mechanochemical synthesis procedure has been applied to fabricate other magnetic nanoparticles such as Nd-Fe-B and Sm-Co [83, 84]. In this green synthesis method, unlike the previously reported methods, no organic solvents are used but only $FeCl_2$ and $H_2PtCl_6(H_2O)$ in stoichiometric amounts to fabricate precursors, the environmentally friendly and low cost NaCl to mill and water to wash. Furthermore, also in this case the temperature to obtain a highly ordered, magnetically hard phase was reduced by about 250 ℃ to as low as 400 ℃ compared to the annealing needed in the case of various nanoparticles synthesis.

5.2 Experimental Procedure

5.2.1 Synthesis of $[Fe(H_2O)_6]PtCl_6$

All the reagents used were purchased from Aldrich. To synthesize the starting polycrystalline complex $[Fe(H_2O)_6]PtCl_6$, a 0.5 M solution containing equal atomic concentration of $H_2PtCl_6 \cdot 6H_2O$ and $FeCl_2 \cdot H_2O$ was prepared using distilled water. The acidity of the solution of $H_2PtCl_6 \cdot 6H_2O$ (pH = 1) prevented the Fe^{2+} to Fe^{3+} oxidation. The reaction begun immediately after mixing the reactants, with the

production of HCl gas, as proved by the white AgCl precipitation obtained when the vapor was reacted with an $AgNO_3$ solution. After a slow evaporation of the solvent at room temperature, a yellow precipitate of hexagonal crystals was collected. The only safe way to increase the reaction velocity was to remove the vapor by a nitrogen flow or to work under vacuum conditions (10^{-3} mbar); since both $H_2PtCl_6 \cdot 6H_2O$ and $Fe(H_2O)_6PtCl_6$ are thermolabile compounds, the temperature should be kept under 50 ℃ to avoid the reduction of Pt. The hexagonal crystals were then purified by recrystallization in ethyl alcohol.

Direct annealing of the $Fe(H_2O)_6PtCl_6$ will form bulk porous $L1_0$ FePt solids. Annealing was performed on the as-made samples in order to investigate the temperature needed to obtain the $L1_0$ phase.. The orange crystal $Fe(H_2O)_6PtCl_6$ was annealed under the atmosphere of forming gas (5% Hydrogen and 95% Argon) at temperatures of 300℃, 350℃, 400℃, 450℃ and 500℃ for 30min.

5.2.2 Synthesis of $L1_0$ FePt Nanoparticles

Although direct annealing of the crystal precursor $Fe(H_2O)_6PtCl_6$ can produce $L1_0$ FePt solids, the bulk FePt is not what we need. To prepare $L1_0$ FePt nanoparticles, ball milling technique was introduced. Figure 24 demonstrates the planetary ball milling process. The relatively large size material was put in a grinding jar with encapsulated balls. The grinding jar was continuously shaking until a fine powder is produced. In a planetary ball milling process, the vial will not only rotate about its own axis but also rotate about the so-called sun-wheel. The grinding balls in the grinding jars are subjected to superimposed rotational movements which are called Coriolis forces. There is a difference in speeds between the balls and grinding jars

which produces an interaction between frictional and impact forces releasing high dynamic energies. This energy will significantly reduce the size of the material.

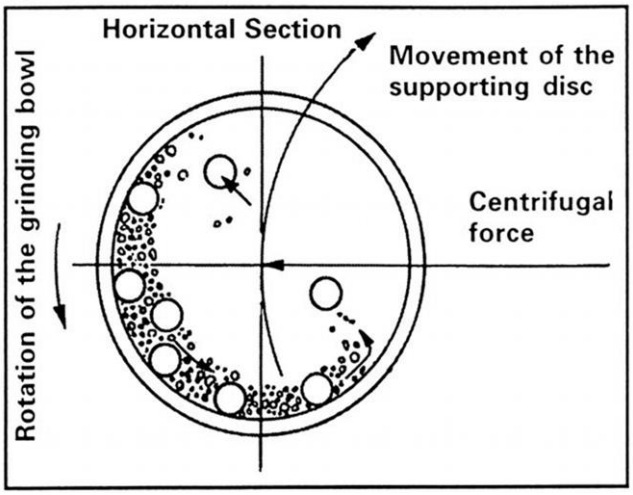

Figure 24 Demonstration of the planetary ball milling process

The precursor $Fe(H_2O)_6PtCl_6$ was mixed with NaCl in different proportion (50mg/20g, 25mg/20g, 10mg/20g) and milled in a planetary milling using a jar (50 mm diameter; 50 mm height) with 6 ZrO balls (10 mm diameter). After milling, a uniform light-yellow mixture containing NaCl and separated nanocrystals of the precursor was obtained. Then, the powder was heated (heating rate = 5 K/min) at different temperatures in a horizontal furnace under a reducing atmosphere of 0.1 L/min flow of 5% H_2 and 95% Ar. Then the samples were kept at the final temperature for 2 h. The following reduction reaction takes place:

$$[Fe(H_2O)_6]PtCl_6 + 3H_2 \rightarrow FePt(L1_0) + 6H_2O + 6HCl.$$

After cooling down, a pale-grey powder was collected, and washed with water. The $L1_0$ FePt nanoparticles were collected by magnetic separation using a magnetic field generated by an electromagnet, until the test on the washing water with $AgNO_3$,

very sensitive to the presence of Cl^{-}, became negative. The theoretical mass yield of our method is 43% (after elimination of H_2O and Cl). Actually, we observed a yield of 35%, due to the loss of the smallest size nanoparticles during the washing step. The whole fabrication process can be demonstrated in Figure 25.

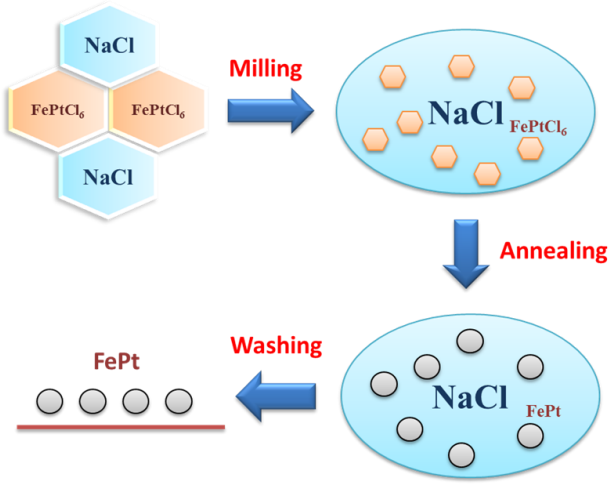

Figure 25 Demonstration of fabrication process of FePt nanoparticles

The FePt particle size and size distribution were determined by transmission electron microscopy (TEM) (JEOL JEM-2010) with a voltage of 200 keV. The crystal structure was determined by both selected area electron diffraction (SEAD) and X-ray diffraction (XRD) patterns (Ultima IV with Cu Kα radiation) using a conventional θ-2θ plane reflection geometry. In the structural study, XRD data were collected at room temperature on an Oxford Diffraction Xcalibur S CCD system with X-ray wavelength $\lambda = 0.71073\dot{A}$. The structure was solved by direct methods and refined using SIR2008 program (part of "IL MILIONE" structure determination and refinement package). Of the 4032 reflections which were collected, 610 were independent.

Magnetic properties were measured by a Versa Lab vibrating sample magnetometer (VSM) (Quantum Design).

5.3 Results and discussion

5.3.1 Structure information of layered precursor $[Fe(H_2O)_6]PtCl_6$

Crystal and data collection details together with structure refinement are summarized in Table 2. All of the data was collected from the newest PDF database. Figure 26 demonstrate the XRD spectra of $Fe(H_2O)_6PtCl_6$.

Table 2 Crystallographic information of $[Fe(H_2O)_6]PtCl_6$

Fomula	$Cl_6FeH_{12}O_6Pt$
Molecular weight	571.65
Crystal system	Trigonal
Lattice parameters	$a = 10.485(2)\dot{A}$
	$b = 10.485(2)\dot{A}$
	$c = 10.901(2)\dot{A}$
	$\alpha = 90^{\circ}$
	$\beta = 90^{\circ}$
	$\gamma = 120^{\circ}$
Space group	$R\bar{3}$
Calculated density	$2.744 g/cm^3$

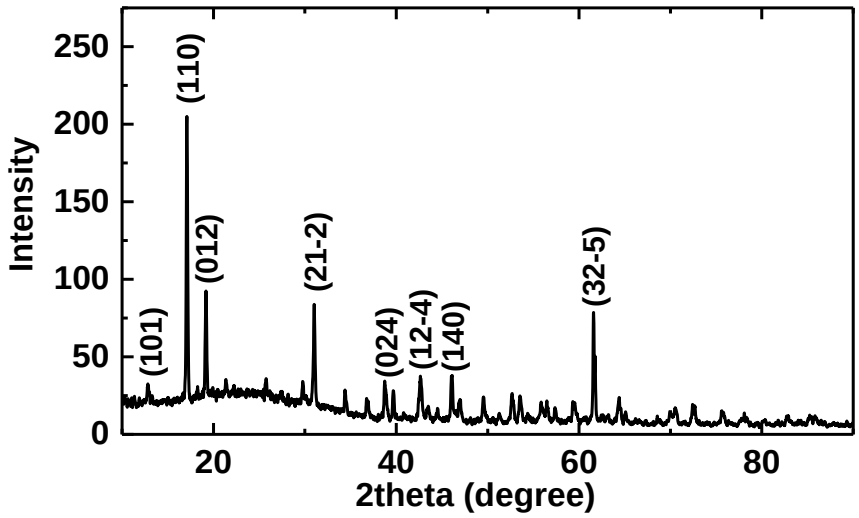

Figure 26 XRD spectra of $Fe(H_2O)_6PtCl_6$

Single crystals of $[Fe(H_2O)_6]PtCl_6$, characterized by a perfect hexagonal shape, were obtained by re-crystallization of the crude product (see experimental section for the synthesis). The crystal structure of $[Fe(H_2O)_6]PtCl_6$ has been reported.[85] A view of the crystal packing is shown in Figure 27, representing octahedral $[PtCl_6]^{2-}$ and $[Fe(H_2O)_6]^{2+}$ ions linked together through a network of hydrogen bonds [86].

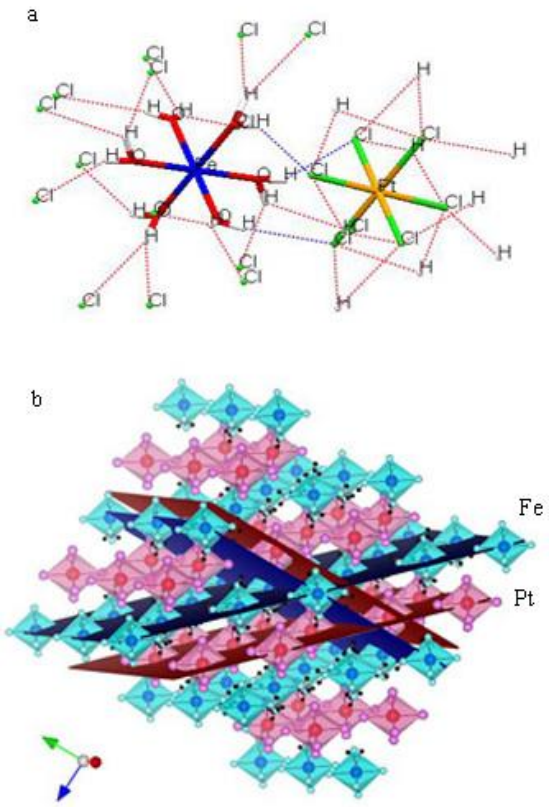

Figure 27 (a) Octahedral ions of Fe and Pt, (b) crystal structure of $Fe(H_2O)_6PtCl_6$ where alternate plans of Fe and Pt are visible

The $FePtCl_6 \cdot 6H_2O$ crystallizes in the trigonal $R\bar{3}$ space group and its asymmetric unit consists of Pt, Cl, Fe, O, H1 and H2. The atomic coordinates with isotropic displacement parameters are listed in Table 3[85]. There are $[Fe(H_2O)_6]^{2+}$ cations and $[PtCl_6]^{2-}$ anions in the crystal which show an octahedron structure as is shown in Figure 28.

Table 3 crystal data and structure refinement[85]

Atom	x/a	y/b	z/c	$U_{eq}(\dot{A}^2)$
Pt	0	0	0	0.0138(1)
Cl	0.0264(2)	0.1934(1)	0.1224(1)	0.0264(3)
Fe	0	0	0.5000	0.0184(3)
O	0.1682(5)	0.1637(5)	0.3871(4)	0.0300(12)
H1	0.16360	0.20840	0.3080	0.0390
H2	0.23270	0.12190	0.36860	0.0390

The $[Fe(H_2O)_6]^{2+}$ cations and $[PtCl_6]^{2-}$ anions are linked by hydrogen bonds involving chlorine atoms and water molecules. There two types of hydrogen bonds one of which involves the H1 atoms and forms a triple bridge between adjacent $[Fe(H_2O)_6]^{2+}$ and $[PtCl_6]^{2-}$. This chain-like structures are shown in Figure 28. The other type of hydrogen bond involves the H2 atoms forming single bridges that links $[Fe(H_2O)_6]^{2+}$ and $[PtCl_6]^{2-}$ ions belonging to different chains.

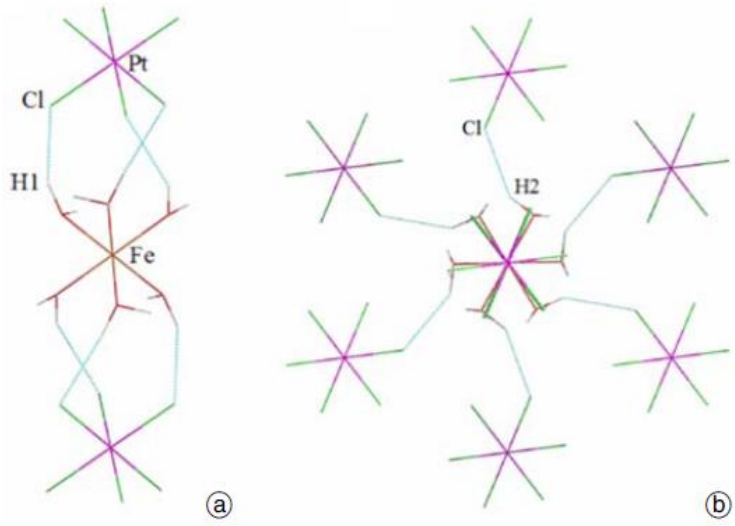

Figure 28 Geometrical representation of hydrogen bonding system of (a) intra chains of O-H1⋯Cl (b) intra chains of O-H2⋯Cl (c) molecular packing view along c-axis[85]

The hydrogen bonding system described above forms alternate layers of Pt and Fe atoms as is shown in Figure 29. The Pt atoms occupy the planes $z = \pm 1/6$ and $z = 1/2$, while Fe atoms occupy the (011) planes and form a second layer. Along the direction of diagonal of bc planes, the interplanar distance of Fe atoms is 3.78 $\dot{A}$ which is almost equal to the length of c-axis for FePt in $L1_0$ phase. Thus, the alternate layered structure of Pt and Fe atoms, which usually exists in the $L1_0$ phase FePt, is obtained in the $R\bar{3}$ space group. The $R\bar{3}$ space group has three-fold symmetry which allows two monoatomic family planes in the same unit cell.

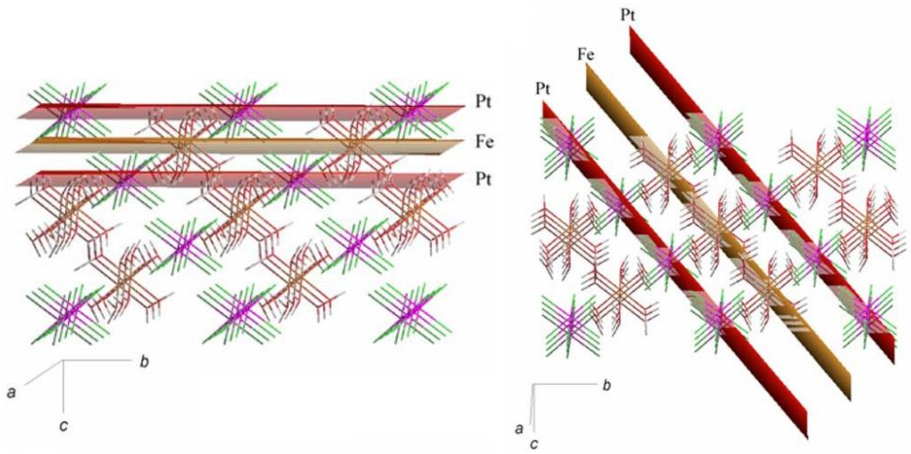

Figure 29 Monoatomic alternating Fe and Pt layers staking along (a) the [001] and (b) [011] directions[85]

5.4 Direct annealing of layered precursor $[Fe(H_2O)_6]PtCl_6$

Since the crystal $[Fe(H_2O)_6]PtCl_6$ has a layered similar to $L1_0$ FePt, direct annealing under the reduction atmosphere will produce FePt alloy in the $L1_0$ phase. The reduction was done under the atmosphere of forming gas with different temperatures varying from 300℃ to 500℃. Figure 25 is the XRD pattern of the FePt annealed at 500℃ for 2h. This pattern fits well with the standard PDF data (PDF 43-1359). To be specific, for FePt alloy in fcc phase, the first allowed peak is the (111) peak and only the peaks with all even or all odd index numbers are allowed ((200) and (220)). For FePt in $L1_0$ phase, due to the slightly difference between c and a (c/a=0.97), the diffraction waves of (001) no longer cancel each other thus the first allowed peak will be (001) instead of (111). This peak is called supperlattice peak. Meanwhile, the distortion of the cubic lattice will decrease the symmetry and cause the splitting of (200) and (002), (220) and (202) peaks. Figure 25 is a typical XRD pattern of $L1_0$ FePt. According to Sherrer's formula [66]:

$$t = \frac{0.9\lambda}{\beta \cos\theta}$$

(where β is the peak width in radian, λ is the wavelength of the X-ray and θ is the corresponding constructive interference angle), sharper diffraction peaks (smaller β) means larger grains. The diffraction peaks in Figure 25 are very sharp which means, that the FePt obtained from direct reduction of $[Fe(H_2O)_6]PtCl_6$ has very large grain size. This is confirmed in the following discussion of the morphology.

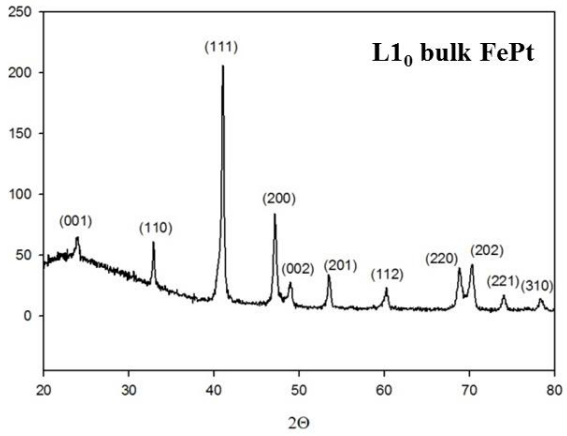

Figure 30 XRD pattern of bulk FePt from direct reduction of $[Fe(H_2O)_6]PtCl_6$

5.4.1 Effect of annealing temperatures

To investigate the lowest temperature needed to get the $L1_0$ FePt, different annealing temperatures (300℃, 350℃, 400℃, 450℃ and 500℃) were used. Figure 31 are the images of FePt samples obtained at different annealing temperatures. From the images we can see that the FePt is porous bulk alloy due to the HCl gas generated during the reduction reaction:

$$[Fe(H_2O)_6]PtCl_6 + 3H_2 \rightarrow FePt(L1_0) + 6H_2O + 6HCl$$

The morphology of FePt annealed at 300℃ is like rods with the length of several hundreds of nanometers and connected to each other to form the bulk material.

With increasing annealing temperature, the rods become shorter and agglomerate. With an annealing temperature of 450℃, the morphology of FePt has changed from rods to porous bulk.

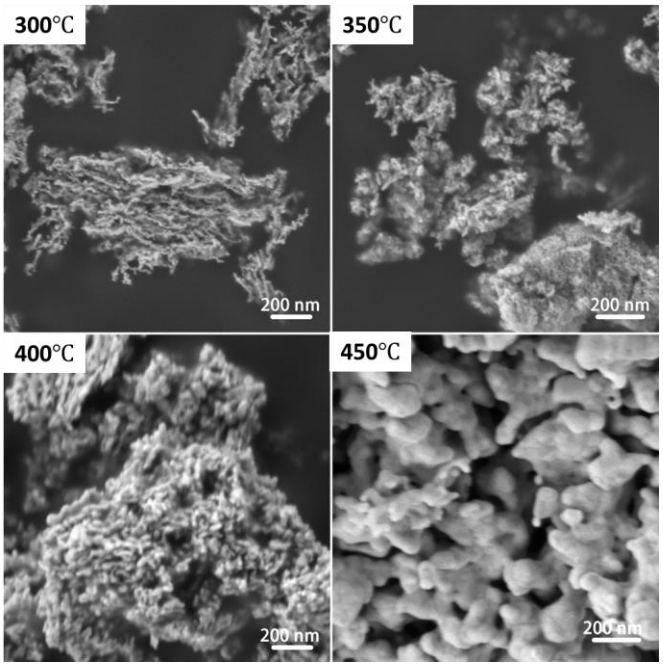

Figure 31 SEM images for bulk FePt from direct annealing of the precursor

Figure 32 shows the XRD pattern of bulk FePt annealed at different temperatures. With annealing temperatures higher than 350℃, the characteristic (100), (110), (201) and (112) superlattice peaks are clearly seen in the XRD pattern. This means that at 400℃, the bulk FePt obtained is in the $L1_0$ phase. At the annealing temperatures of 400℃, 450℃ and 500℃, splitting of (200) and (002), (220) and (202) peaks is very clear. At 350℃, the split cannot be seen but the shift of the (200) and (220) can be observed compared to the peak positions of the sample annealed at 300℃. This means that the degree of $L1_0$ ordering is relatively small with the annealing temperature of 350℃. As the annealing temperature increases, there is also a

shift of (111) peak to higher angles. However, at 300℃ there are no visible characteristic peaks of $L1_0$ phase FePt. Due to the broadness of the peaks, we cannot say that there is no $L1_0$ phase FePt especially when the degree of ordering is very low.

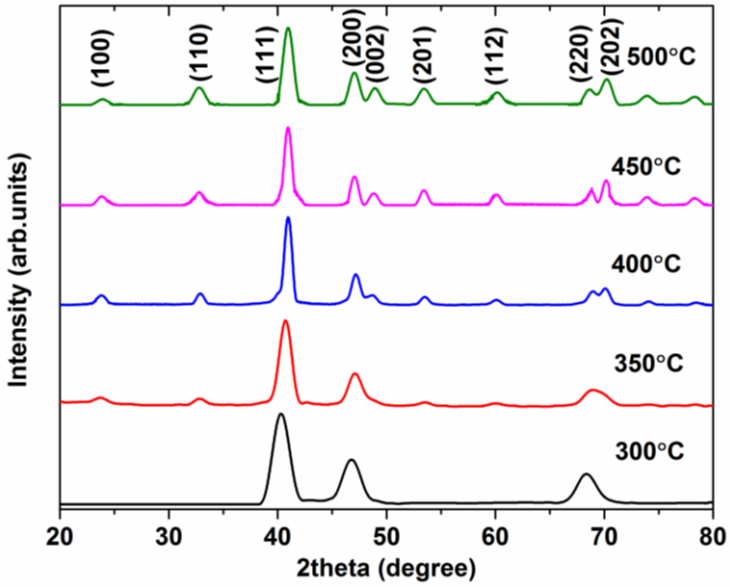

Figure 32 XRD patterns of bulk FePt annealed at 300℃, 350℃, 400℃, 450℃ and 500℃

Figure 33 demonstrates the hysteresis loops of bulk FePt annealed at different temperatures. The annealing temperature varies from 100℃ to 500℃ and the hysteresis loops were measured at room temperature. Table 4 lists the coercivity data of these samples. With the increase of annealing temperature, the coercivity increases. At annealing temperatures lower than 300℃, the coercivities are smaller than 1 kOe which means the chemical degree of ordering of $L1_0$ FePt phase is very low. At annealing temperatures higher than 400℃, the coervities are higher than 10 kOe. The coercivity data agrees with the XRD pattern shown above very well. Beginning at 350℃, the clear sign of $L1_0$ FePt can be seen with the emergence of (001) and (110)

peaks and split of (200) and (002) peaks. At 300℃ only broad peaks can be seen and no superlattice peaks are observed which means that most of the FePt bulk annealed at 300℃ is in the magnetically soft fcc phase; the presence of the $L1_0$ fct with very low degree of ordering cannot be excluded.

But from the enlarged image of the loops for the sample annealed at 300℃ and 200℃, a coercivity of around 1 kOe can be observed which is much higher than the coervity of pure fcc phase FePt. . According to DTA-TGA data in Figure 35 which will be discussed later, the loss of H_2O molecules, Cl atoms and formation of ordered structure happened at the same time. Therefore, even at the very beginning of the reaction a small amount of $L1_0$ FePt is formed. This would explain the reason why with the annealing temperature as low as 200℃, there is still some coercivity which is higher than the coercivity of fcc FePt phase. Another possibility is that the $L1_0$ FePt formed at low annealing temperature has a very low degree of ordering but this low degree of ordering which cannot be detected from the XRD pattern because of the broad peaks.

According to Sherrer's formula [66]:

$$t = \frac{0.9\lambda}{\beta \cos\theta}$$

where β is the XRD width in radians, λ is the wavelength of the X-ray and θ is the corresponding constructive interference angle. For the 350℃ annealed sample ,the grain size calculated is 6.6 nm which is very small explaining the broadness of the diffraction peaks.

At 350℃, the characteristic superlattice (100) and (110) peaks are broad and weak and there is no obvious split of (200) and (002) but the higher angle shoulder of this peak indicates the presence of of a small amount of (002). . Compared to the

sample at 300℃, the chemical degree of ordering is higher and therefore, this sample has an intermediate coercivity of 5.4 kOe. For the most commonly used chemical synthesis, to get ordered $L1_0$ phase FePt nanoparticles, post annealing with temperatures higher than 600℃ is needed. In the green synthesis procedure used in this thesis, even at the temperature as low as 350℃, a relatively high chemical ordering of $L1_0$ and coercivity were obtained. This significant decrease of the temperature to obtain $L1_0$ FePt is due to the special layered structure of alternating planes of Fe and Pt atoms of the crystal precursor $[Fe(H_2O)_6]PtCl_6$ [82, 87].

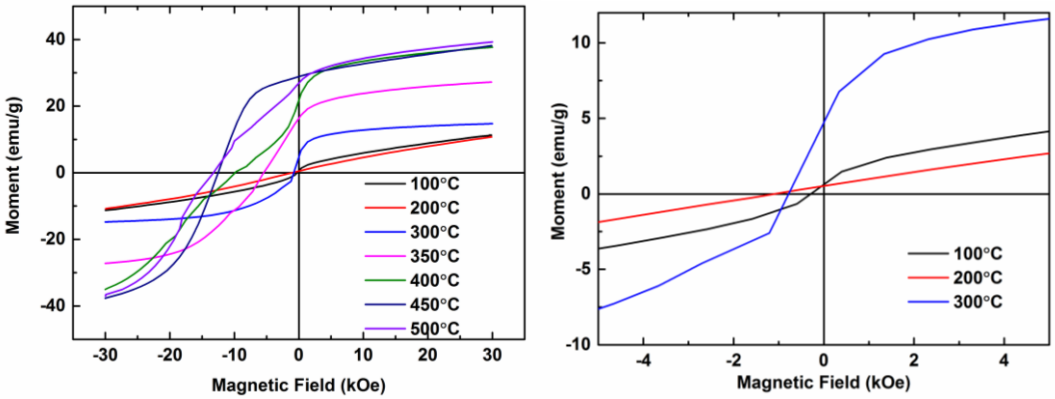

Figure 33 RT hysteresis loops of bulk FePt annealed at different temperatures

Table 4 Coercivities of bulk FePt annealed at different temperatures

Temperature/℃	100	200	300	350	400	450	500
Coercivity/kOe	0.3	1.0	0.8	5.4	9.7	12.4	13.5

As reported in the literature, the annealing temperature for initiating the fcc to fct transition in a bulk FePt system is about 800-850 ℃, and it can be decreased to around 650 ℃ in nanoparticles prepared by chemical route.[16, 75, 76] In sputtered

FePt films a transition at lower temperature (T = 500 ℃) was observed.[88] Nakaya et al.[77] reported that the use of pure H_2 during the annealing treatment leads to a decrease of the transformation temperature to 300 ℃, attributing this result to the higher mobility of Fe and Pt atoms due to hydrogen diffusion in interstitial sites. A more remarkable temperature reduction (down to 275 ℃) was observed in FePt epitaxial films obtained by the alternate layer growth of Fe and Pt.[89] In both films and nanoparticles the starting alloy completes the phase transformation in a temperature range and a well-defined transition temperature is hardly identified. The presence of random starting configurations in particle systems and different degrees of order achieved in the different preparation processes can explain the spread of transition temperatures reported in the literature. Indeed, it is generally agreed that a higher percentage of chemically ordered Pt and Fe atoms in the starting material is associated with a decrease of the phase transformation temperature.[90] Song and co-workers published a work about the utilization of a single organometallic compound $(CO)_3Fe(-Ph_2PCH_2PPh_2)(-CO)PtCl_2$ containing Fe and Pt atoms inside the same molecule.[91] After reduction and annealing at 550 ℃ partially ordered FePt nanoparticles were observed.

In this thesis, we successfully obtained the fct FePt at an annealing temperature as low as 350 ℃ due to the ordered starting precursor. From a thermodynamic point of view, in our synthesis an energetically favored starting point for the transformation to the tetragonal phase is presented. Figure 29 shows a qualitative thermodynamic diagram for the fcc/fct phase transformation for both amorphous and ordered crystalline precursors. In the case of an amorphous precursor (Figure 34(a)) a low energy is needed for the salt reduction (the reduction easily

happens in solution, as in the Sun's synthesis)[15]. This step brings to the crystalline but chemically disordered fcc phase. However, a much higher energy (proportional to the decrease of the entropy S) is required to induce the disorder-order transition where the atoms re-arrange by diffusion onto alternate single metal layers. When using a crystalline layered precursor, the energy balance for the reaction is more favorable, the entropic contribution is minimized (see Figure 34(b)) and less energy is required for Fe and Pt reduction (the reduction in this case occurring in the solid/gas interaction).

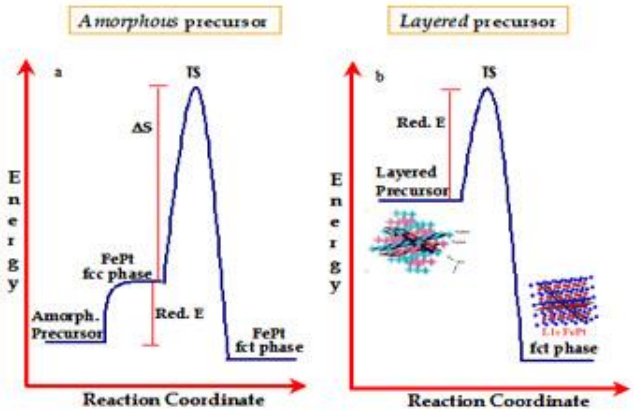

Figure 34 Qualitative thermodynamic reaction paths in the case of amorphous or crystalline precursors

Thermal analysis is shown in Figure 35. The heating process of $[Fe(H_2O)_6]PtCl_6$ powder was monitored by a thermogravimetric and differential thermal analysis (TGA-DTA) under the reductive atmosphere of forming gas performed up to 700℃ with a heating rate of 5℃/min. In the TGA curve, there are four well distinct weight losses during the heating: below 100℃ (≅ 4%), 120℃ (≅ 28%), 200℃ (≅ 16%) and 230℃ (≅ 10%). The total loss of weight is about 56% which is related to the expected loss of 6 H_2O molecules and 6 Cl atoms. According to the DTA

curve, the process is partially overlapped and it is not possible to isolate and characterize each single step. A reasonable sequence under the thermogravimetric experimental condition is proposed in the paper [82] as follows: The first broad weight loss under 100℃ is likely due to the water desorption. The drop at 120℃ is related to the elimination of 6 H_2O molecules linked to Fe atoms and 2 Cl atoms according to the following reduction reaction:

$$[Fe(H_2O)_6]PtCl_6 + H_2 \rightarrow FePtCl_6 + 6H_2O + 2HCl$$

At the temperatures above 200℃, there is a wide temperature range for the elimination of the remaining 4 Cl atoms. The small DTA bump at 450℃ is due to the structrural rearrangement after the loss of Cl atoms is complete. At the temperatures higher than 450℃ up to 700℃, there is no weight loss and not any signs of phase trasition in the DTA curve. All of the discussion above indicates that the $L1_0$ FePt alloy is obtained after the elimination of Cl atoms. To verify this result, low temperature annealing (400℃, 350℃, 300℃, 200℃ and 100℃) was performed and the XRD pattern and hysteresis loops are shown in Figure 32 and 33. Results reveal that even with the annealing temperatures lower than 300℃, there is still some coercivity around 1 kOe which can not be achieved in the isotropic fcc phase. The magnetization at 30 kOe decreases with the decrease of annealing temperatures. This means the elimination of Cl atoms and the formation of $L1_0$ FePt happened simutaneouly. With the annealing temperature lower than 300℃, the energy is not enough for the elimination of all Cl atoms and only partial of the crystal is reduced to FePt. As the annealing temperature increases, the portion of reducted FePt alloy increases which can explain the increase of magnetization at 30 kOe. At 400℃, the elimination of Cl atom is almost finished and there is a large portion of reduced $L1_0$ FePt alloy.

Therefore, the coercivity increases to 9.7 kOe. There is no evidence of the fcc-fct phase transition and it is related to the ordered arrangement of Fe and Pt irons on the alternating atomic planes in the $[Fe(H_2O)_6]PtCl_6$ crystals.

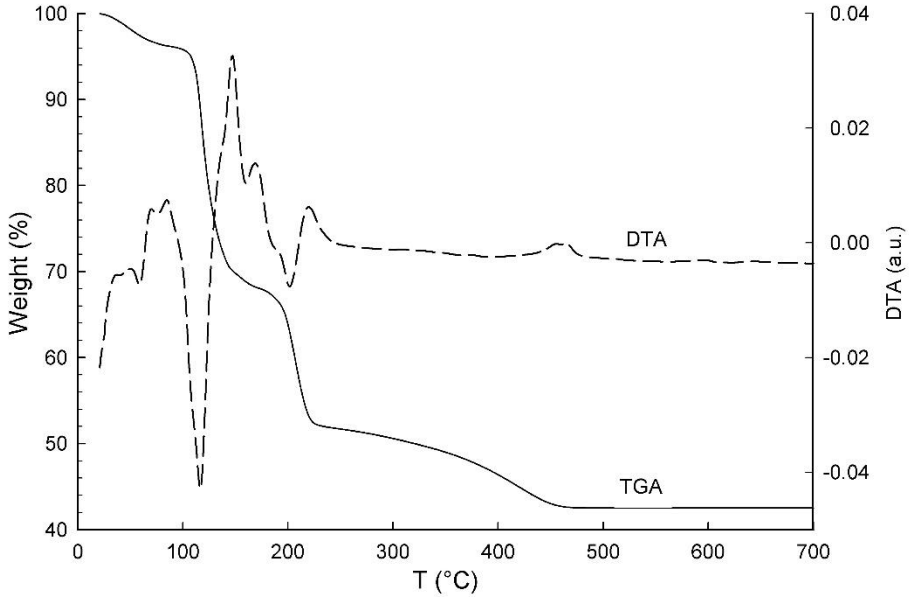

Figure 35 TGA-DTA of $[Fe(H_2O)_6]PtCl_6$ under flux of forming gas[82]

5.5 $L1_0$ FePt Nanoparticles Fabricated by Ball Milling of the Precursor with NaCl

Although $L1_0$ FePt alloy was successfully obtained at the temperature as low as 400℃, the SEM images in Figure 26 showed a porous bulk structure which is not what we want for the ultra-high density magnetic recording. To get small $L1_0$ FePt nanoparticles, NaCl matrix and planetary ball milling techniques were introduced. The mechanism of planetary ball milling was discussed above (see the experimental details).

The main difference of the synthesis proposed in this thesis compared to the synthesis already discussed [82] is the type of additive used in the ball milling step. In the previous synthesis the intermediate products were FePt nanoparticles mixed with silica oxide, which had to be eliminated using HF, and therefore, the procedure could not be considered environmentally friendly. In the present synthesis we replaced SiO_2 microparticles by NaCl.

NaCl was chosen because its crystals are hard enough to break the crystals of the starting salt without destroying the crystalline structure. Moreover, after heating and cooling procedures in reducing atmosphere, NaCl can be easily removed using deionized water and the $L1_0$ FePt nanoparticles can be collected.

5.5.1 Effect of annealing temperature

To investigate the temperature to obtain the $L1_0$ FePt particles made by our method, different annealing temperatures were used in the range of 350℃ to 500℃. The hysteresis loops in Figure 36 and coercivity values in Table 5 revealed that at around 400℃, the elimination of Cl atoms was partial with the particles showing room temperature (RT) coercivity of 4.9 kOe. At 450℃, the coercivity is further increased up to 10.9 kOe at RT which is large for chemically synthesized FePt nanoparticles. Also, there is a significant increase of the magnetization at 30 kOe. This large coercivity and increase of magnetization revealed that the chemical reaction finished at 450℃ and the $L1_0$ phase FePt nanoparticles were obtained. The XRD patterns in Figure 37 also showed the characteristic (001), (110) peaks of fct phase and the splitting of (200) peaks in the samples annealed at 450℃ and 500℃. However, for the 400℃ sample, the (111) and (200) peaks are broadened and shifted towards the angle of fct phase; however, the (001) and (110) peaks are so weak and broad that can’t be

seen clearly in Fig 37(b). The lower coercivity values at 400℃ indicate an incomplete $L1_0$ phase formation. Also, Figure 36 shows a magnetization increase as the annealing temperature is increased which can also be explained by the degree of phase formation increasing which increases with higher annealing temperature.

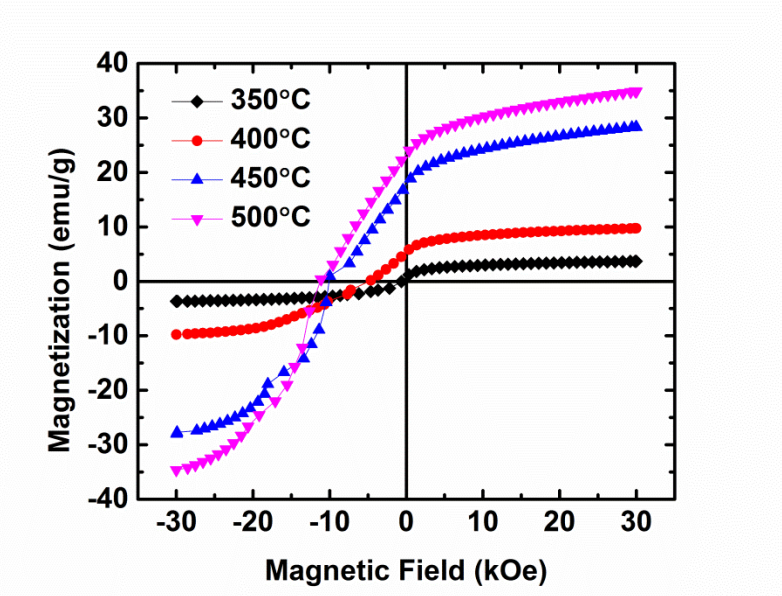

Figure 36 RT hysteresis loops of FePt nanoparticles annealed at different temperatures

Table 5 Coercivity and magnetization values at 30 kOe of FePt nanoparticles annealed at different temperatures

Annealing temperature(℃)	350	400	450	500
H_c (kOe)	0.5	4.9	9.2	10.9
M_s (emu/g)	3.7	9.7	28.4	34.9

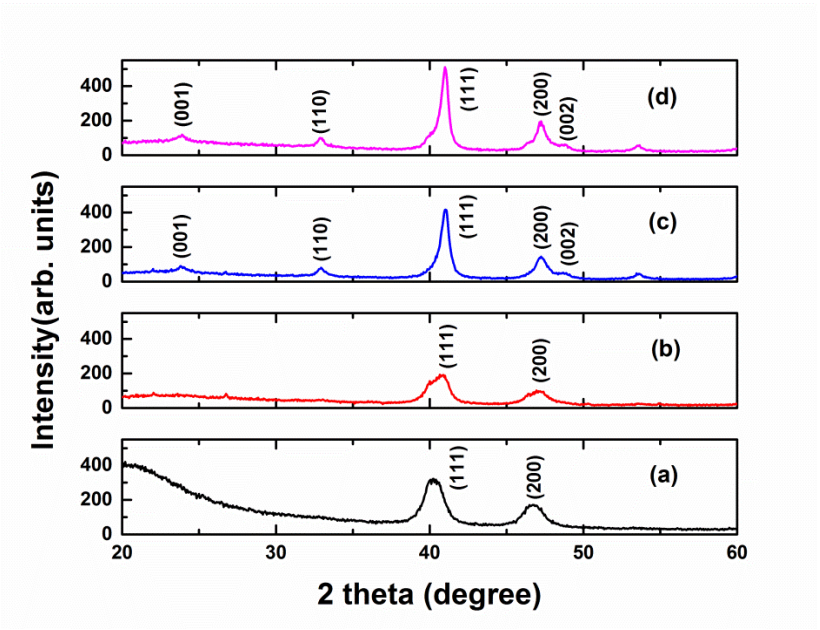

Figure 37 XRD patterns of FePt nanoparticles annealed at (a) 350℃ (b) 400℃ (c) 450℃ (d) 500℃

5.5.2 Effect of ball milling conditions

5.5.2.1 Effect of precursor/NaCl ratio

To investigate the influence of different precursor/NaCl ratio, one set of FePt nanoparticles was fabricated as listed in the summary Table 6.

Table 6 Summary of structural and magnetic data for the samples with different precursor/NaCl ratio

Label	S50	S25	S10
Precursor/NaCl ratio	50mg/20g	25mg/20g	10mg/20g
Ms at RT (emu/g)	35.4	20.6	14.7
Hc at RT(kOe)	10.9	5.2	4.7

Mr/Ms at RT	0.67	0.59	0.56
Average Size (nm)	13.2	12.1	6.2
Standard Deviation of Size (nm)	5.6	4.6	2.6

The XRD patterns reported in Figure 38 show the presence of the peaks characteristic of the $L1_0$ phase. For sample S50, the characteristic (001), (110), (201) and (112) peaks are easily observed and as well as the splitting of peaks (002) and (200), (220) and (202). Both S25 and S10 samples show broader diffraction peaks, which are attributed to the presence of very small particles/grains However, the broadened and asymetric (200) and (220) peaks also suggest the presence of the $L1_0$ phase.

The degree of chemical ordering of FePt nanoparticles can be quantified by the long-range ordering parameter S, which can be calculated by the following formula [92]:

$$S = \left[\left(\frac{I_{001}}{I_{002}}\right)\left(\frac{F_f}{F_s}\right)^2 \frac{(L \times A \times D)_f}{(L \times A \times D)_s}\right]^{\frac{1}{2}} \cong 0.85\left(\frac{I_{001}}{I_{002}}\right)^{\frac{1}{2}}$$

where I_{hkl} is the integrated intensity, F the structure factor, L the Lorentz polarization factor, A the absorption factor, D the temperature factor, and the subscripts f and s refer to the fundamental and superlattice peaks respectively.[92] According to the formula, the ordering parameter for sample S50 is 0.75, which is high for chemically synthesized FePt nanoparticles. For samples S25 and S10, the ordering parameter is 0.75 and 0.53, respectively. Theoretically, the fully ordered fct phase FePt should have a chemical degree of order of 1.0. A degree of ordering lower than 1.0 indicates a not fully ordered fct phase. The positions of fcc and fct (111) and (200) peaks in the XRD are very close and the width of the peaks makes it impossible

to eliminate the possibility of a small portion of fcc phase FePt nanoparticles. Moreover, the defects inside the FePt nanoparticles may generate partial disordering inside the FePt nanoparticles which will also decrease the degree of chemical ordering.

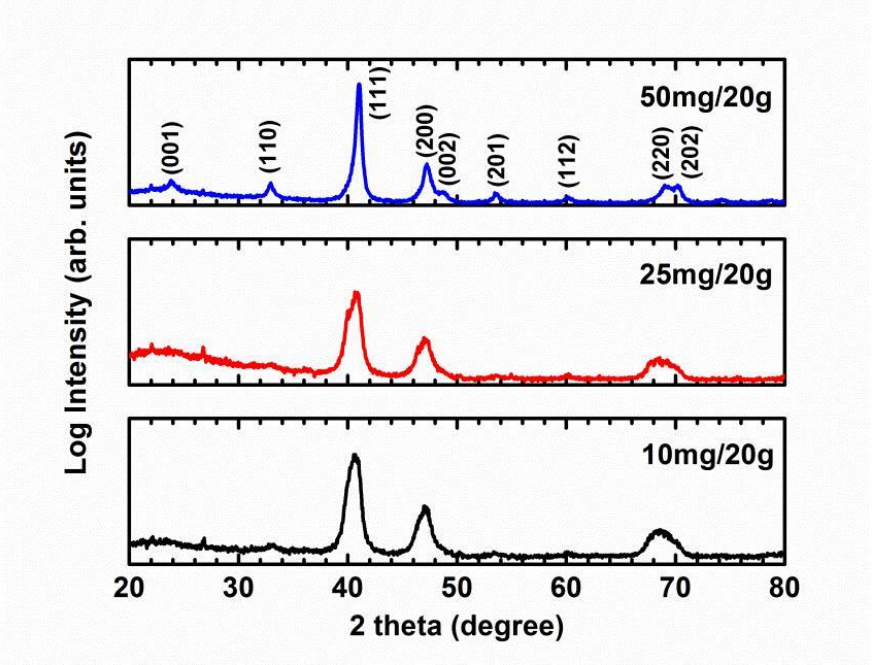

Figure 38 θ-2θ XRD pattern of FePt nanoparticles with different precursor/NaCl ratio

The TEM images of FePt nanoparticles are shown in Figure 39. For the sample S50 the bright-field images show a size distribution (see Figure 39a_1) in the range 5 - 35 nm (Figure 39a_3). All the observed nanoparticles are single crystals as shown from the high-resolution TEM (HRTEM) images in Figure 39a_2. Some coalescence exists, indicating that the concentration of $[Fe(H_2O)_6]PtCl_6$ in NaCl was too high for this sample to ensure a good separation of the nanocrystals. The (100) and (110)) characteristic superlattice rings in the SAED pattern (Figure 39a_4) confirmed that the FePt nanoparticles have the fct structure. By decreasing the content of the precursor

(sample S25) (Figure $39b_1$) a narrower size distribution (5-23 nm) was obtained (Figure $39b_3$). Actually, the majority of the nanoparticles have a size in the range 5-15 nm and only a few nanoparticles larger than 20 nm were observed. Some coalescence phenomena were also observed (Figure $39b_1$, Figure $39b_3$). In this sample, the nanoparticles are also single crystals (Figure $39b_2$) and with the fct structure. Better results were achieved in sample S10. In Figure $39c_1$ we can see well-separated nanoparticles in the range 3-6 nm with only few nanoparticles out of it. In this sample we did not observe coalescence phenomena, the nanoparticles remaining always well separated. The HRTEM images (Figure $39c_2$) always confirm the presence of single crystal nanoparticles and SAED pattern (Figure $39c_4$) together with XRD (Figure 38_{S10}) confirmed the fct structure.

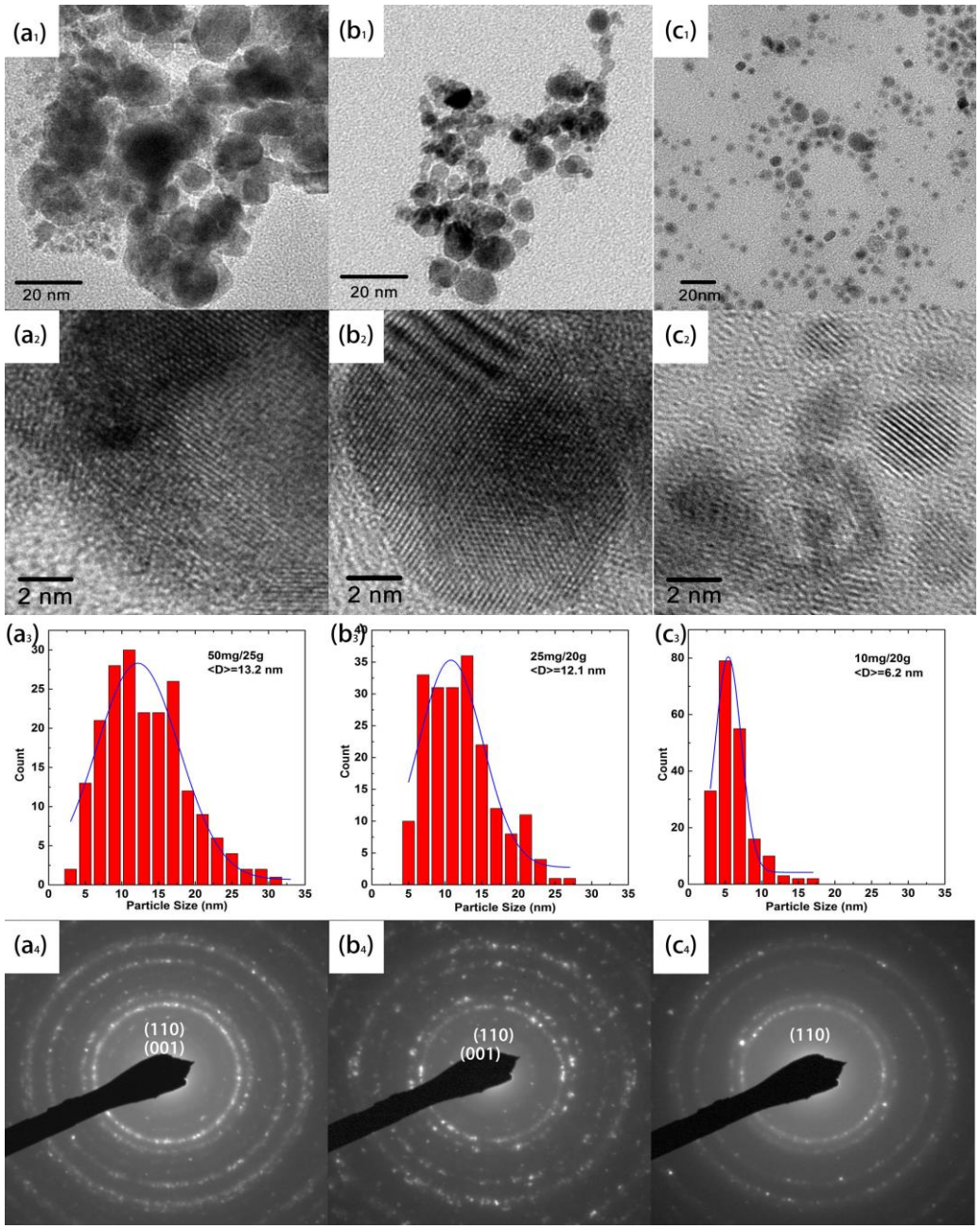

Figure 39 (a_1) bright-field image of sample S50 (a_2) high resolution image of sample S50 (a_3) size distribution of sample S50 (a_4) diffraction pattern of S50 (b_1) bright-field image of sample S25 (b_2) high resolution image of sample S25 (b_3) size distribution of sample S25 (b_4) diffraction pattern of S25 (c_1) bright-field image of sample S10 (c_2) high resolution image of sample S10 (c_3) size distribution of sample S10 (c_4) diffraction pattern of S10

Figure 40 shows the hysteresis loops of the three samples. The magnetization value at 30 kOe (maximum field used) is far from the saturation value because of the large magnetocrystalline anisotropy of the fct FePt phase and the randomness of the particles. The highest coercivity is obtained in the sample S50 with the largest average grain size of 13.2 nm. As expected, the coercivities are larger at lower temperature because of thermal activation. The coercivty increases from 10.9 kOe (RT) to 15.7 kOe (50 K) for sample S50 (Figure 40a), from 4.7 kOe (RT) to 4.8 kOe (50K) for sample S10 (Figure 40c) and the largest variation is from 5.2 kOe (RT) to 10.3 kOe (50 K) for sample S25 (Figure 40b). According to Figure 16, for small particles with the size decreasing from the multidomain regime (bigger particles) toward smaller particles, the coercivity first increases to a maximum (with the particle size equals the single domain size D_s), and then decreases with size reduction because of thermal effects. Below a critical size, different for each material, the coercivity becomes zero and the system enters the so-called superparamagnetic state, where thermal effects are predominant making the magnetization unstable. For $L1_0$ FePt nanoparticles the superparamagnetic critical size at room temperature (RT) is 2.8 nm. We can argue that in our nanoparticle systems there are two main contributions to the magnetization reversal: one is the predominant portion of single domain ferromagnetic fct nanoparticles and the other is the partially ordered nanoparticles with the mixture of fcc phase and fct phase (the possibility of a pure fct phase but with low degree of atomic ordering cannot be excluded). The decrease of coercivity observed going from sample S50 to sample S10 can be explained by the particle size reduction below the single domain region. The kink in the second quadrant of sample S25 and S10 could be due to the presence of a magnetically soft phase which as we explained before can

be attributed to the presence of some fcc FePt nanoparticles or to some nanoparticles with a low degree of atomic ordering. Solid conclusions cannot be made because of the limitation of the characterization methods. However, in the discussion of Chapter 8, the ultra-high-resolution HAADF images revealed several kinds of defects in the nano-islands fabricated by magnetron sputtering. Even inside a single nanoparticle with the size of several nanometers, there are several kinds of defects leading to local disorder (we can also say partial fcc phase). Therefore, we can argue that in the nanoparticles fabricated by this green chemical method, there is a high possibility that the nanoparticles are composed of predominant portion of fct phase and a small portion of fcc phase or fct with very low degree of ordering Moreover, from the bright field images of Figure 39, we can find some very small nanoparticles with the particle size smaller than 2.8 nm which are superparamagnetic nanoparticles. Because the lowest testing temperature of the VSM used is 50K which is higher than the blocking temperature of small FePt nanoparticles, no significant difference of the coercivities can be observed. The different coercivities obtained can be explained by the different degree of atomic ordering.With the decrease of particle size, surface effects play a more important role during the ordering. R. Wang et al[93] reported that for very small nanoparticles, surface is an important defect to decrease the degree of ordering. Therefore, for smaller nanoparticles, the degree of ordering decreases with the decreased size. Sample S10 shows the highest percentage of smaller nanoparticles and smallest coercivity compared to the other two samples.

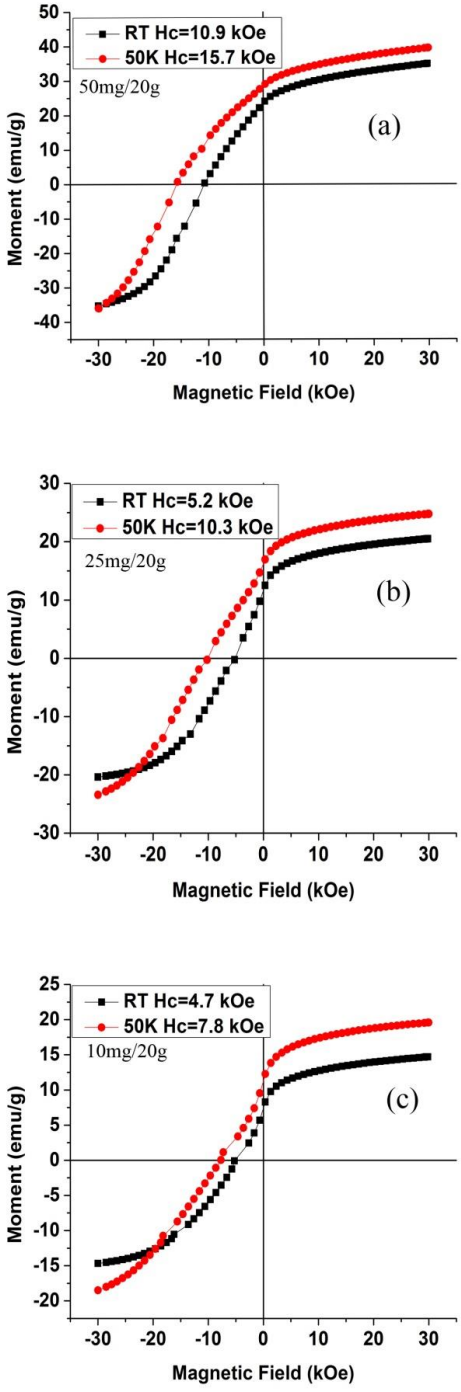

Figure 40 Hysteresis loop of the samples (a) S50, (b) S25 and (c) S10 at room temperature and 50K

5.5.2.2 Effect of ball milling time

To further investigate the influence of ball milling conditions on the morphology and particle size, bright-field TEM images of FePt nanoparticles with different milling times are shown in Figure 41. Because the nanoparticles were collected using a magnetic field, there is agglomeration of the nanoparticles. As the milling time is increased from 2h to 15h, there is an obvious trend of particle size decrease from 28.2 nm to 8.7 nm as shown in Table 7. According to the hysteresis loops shown in Figure 42, in the samples milled for 1h, 2h and 10h, shoulders are observed on the demagnetization part of the loops which are attributed to the presence of a soft phase, possibly the FePt fcc phase/low degree of ordering fct as discussed before. However, there is no such shoulder in the 5h sample. This inconsistency is probably due to the control of reaction conditions which in this case were ideal for the formation of mostly magnetically hard fct particles with no evidence of fcc/low degree ordered fct .. Moreover, the ball milling process introduces defects to the nanoparticles such as surface and local disordered regions which also contribute to the shoulder in the loops. Furthermore, the XRD patterns shown in Figure 43 suggest that the sample milled for 5 h has the highest degree of ordering as indicated by the stronger superlattice peaks. It may be also possible that at long milling times, the energy introduced into the ball milled material transforms some of the fct phase back to the fcc phase.

Table 7 Particle size of FePt nanoparticles with different milling times

Milling time(h)	10	5	2	1
Particle size(nm)	8.7	12.8	16.7	28.2

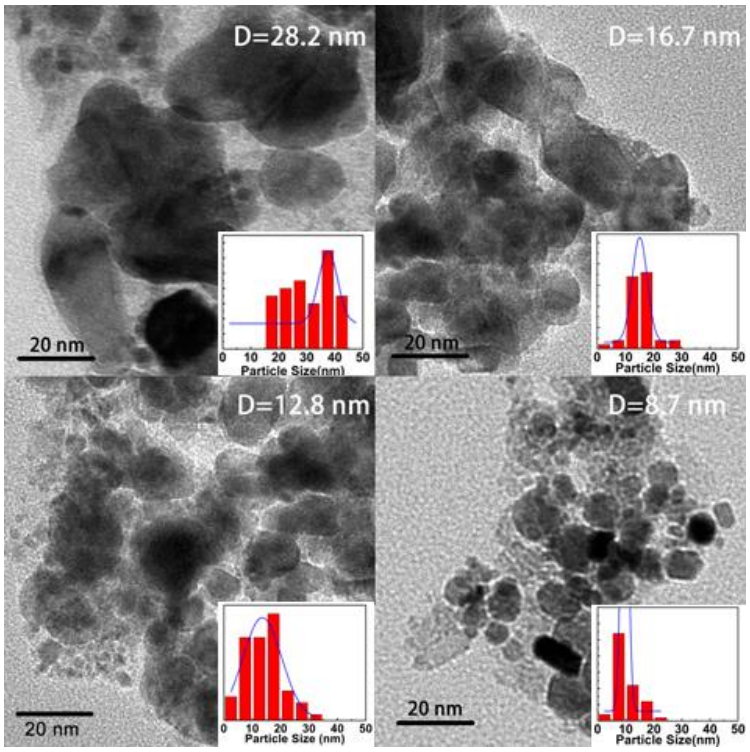

Figure 41 Bright-field images of FePt nanoparticles with milling times of (a) 1h (b) 2h (c) 5h and (d) 10h

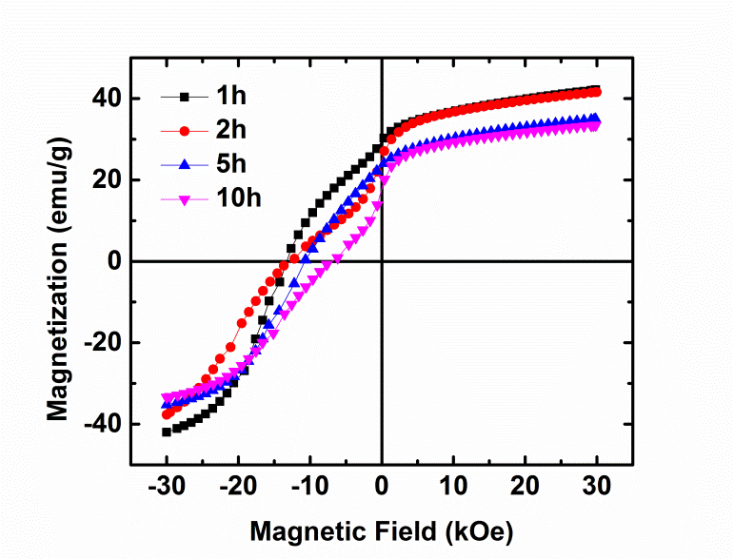

Figure 42 Hysteresis loops of FePt nanoparticles with different milling times

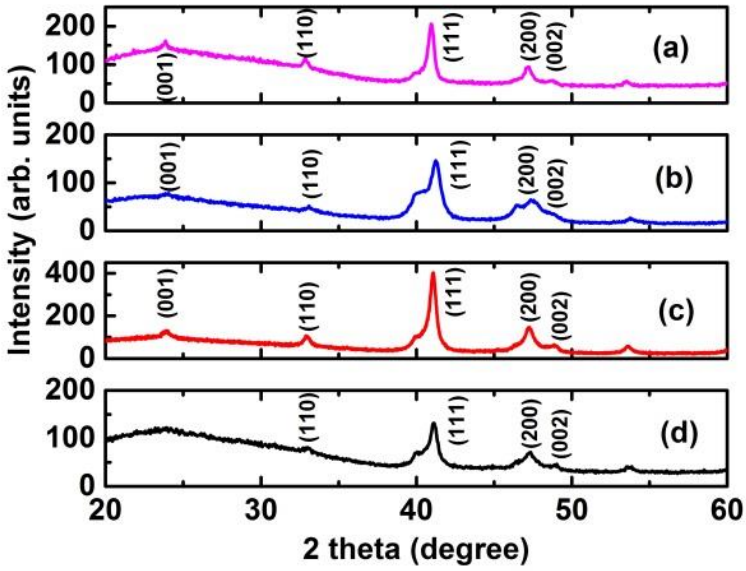

Figure 43 XRD patterns of FePt nanoparticles milled for (a) 1h (b) 2h (c) 5h (d)10h

5.6 Conclusions

In this chapter, we introduced a green synthesis of FePt nanoparticles with the magnetically hard $L1_0$ structure. To the best of our knowledge this is the first time that magnetically hard nanoparticles are synthesized using only environmentally friendly chemical products like water and sodium chloride. We used the $[Fe(H_2O)_6]PtCl_6$ as the precursor which has a special layered structure with Fe and Pt atoms alternatively layered inside the crystal. Different annealing temperatures varying from 100℃ to 500℃ are used to determine the $L1_0$ phase formation temperature. The XRD spectra and hysteresis loops revealed that at temperatures as low as 350℃, this layered structure can react with H_2 and form $L1_0$ FePt. This temperature is 250℃ lower than typical phase transformation temperature. DTA-TGA analysis demonstrated the reaction process and a qualitative model was used to explain the significant decrease

of $L1_0$ phase formation temperature. By the planetary ball milling of the precursor and NaCl and subsequent annealing at 400 ℃ in a reducing atmosphere (5% H_2 and 95% Ar), we obtained FePt $L1_0$ nanoparticles with selected size as a function of $[Fe(H_2O)_6]PtCl_6$ / NaCl ratio. By varying this ratio, we were able to avoid the coalescence phenomena and obtain single crystal nanoparticles with size around 6 nm. The influence of ball milling time on the particle size and magnetic properties was also investigated. With longer ball milling time, the average particle size decreased significantly. There was not much difference in the coercitives with the change of ball milling time. But there were shoulders in the second quadrant of the hysteresis loops. There are two possible reasons: one is the mixture of fct/fcc particles and the other one is the defects introduced by the ball milling which bring local disorder inside the nanoparticles. This method in principle could be used, starting from other bimetallic salts, to carry out environmentally friendly synthesis of many other bimetallic chemically ordered alloys as AuCu, CoPt, etc. applicable in fields as magnetism and catalysis.

5.7 Proposed future work

Although we successfully obtained FePt nanoparticles with the acceptable coercivity of 4.7 kOe and average size of 6.2 nm, most of the samples have the problem of agglomeration which is certainly undesirable for ultra-high density magnetic recording. To solve this problem, two possible methods can be used.

The first technique is spin-coating. Figure 44 demonstrates the mechanism of spin-coating. Porous membrane such as Al_2O_3 templates can be used to hold certain amount of $[Fe(H_2O)_6]PtCl_6$ solution. High speed spinning can help to disperse the

solution evenly into the pore of the template. After the spinning, annealing can be applied to finish the reaction and form $L1_0$ FePt.

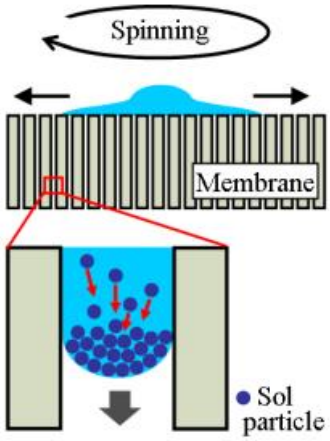

Figure 44 Mechanism of spin-coating

In the other technique demonstrated in Figure 45, a 2D functionalized nano-perforated film is used in the dip coating process with a controlled withdraw speed. Certain amount of $[Fe(H_2O)_6]PtCl_6$ solution will be trapped in the film. After the post annealing under reduction atmosphere, the FePt nanoparticles can be collected by removal of the film.

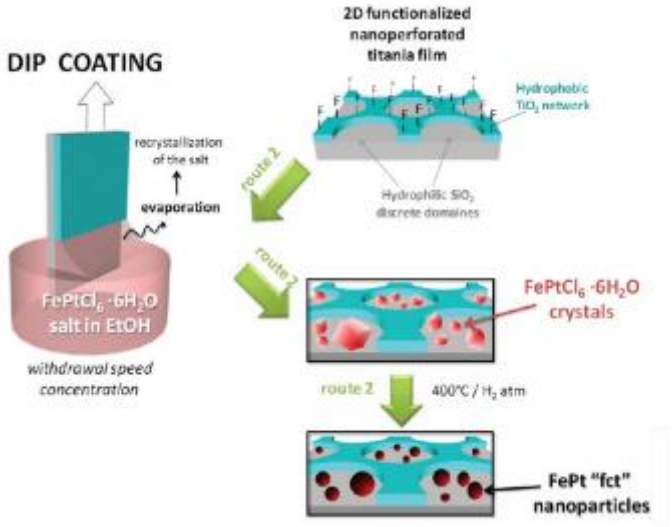

Figure 45 Demonstration of dip coating technique to avoid the agglomeration of FePt nanoparticles

Chapter 6

SOLID STATE FABRICATON OF L10 FEPT NANOPARTICLES ON EXFOLIATED GRAPHENE FROM LAYERED PRECURSOR

6.1 Introduction

In Chapter 5, a novel green chemical synthesis fabrication method of $L1_0$ FePt nanoparticles was introduced. Well separated FePt nanoparticles with average size of 6.2 nm and room temperature coercivity of 4.7 kOe were obtained. However, most of the FePt nanoparticles prepared have the problem of agglomeration and relatively wide size distribution. The use of electromagnetic field to collect the FePt nanoparticles causes the agglomeration and the planetary ball milling technique introduces a wide particle size distribution. To solve this problem, exfoliated graphene support is used during the fabrication process and a novel solid state fabrication of $L1_0$ FePt nanoparticles with uniform size distribution and high coercivity is described in this chapter.

Graphene (G), a two-dimensional single layer of carbon atoms with p-electrons fully delocalized on the graphitic plane, has a large surface area, good chemical stability, very high electrical conductivity and strong mechanical properties which make it an excellent supporting materials in the application of molecular electronic devices, energy transfer and storage and fuel cell catalysts [10, 94-96]. G is often used as a support for certain functional particles with special features useful in optical [97], electrical catalysis and so on [98]. Graphene can maximize the surface area of nanosized electrocatalysts, facilitate electron transport, promote mass transfer at the electrode surface and keep a stable catalyst structure [99]. Among the methods to prepare G, thermal reduction of graphene oxide (GO) is a promising approach for

large-scale production [100-104]. GO is a strongly oxidized layer of carbon material which can be easily exfoliated into thin-layer sheets dispersed in water[105]. The existence of sp^2 domains and oxygen-containing groups allow the bonding interactions between GO and a wide range of materials which makes GO an ideal substrate to hold inorganic nanoparticles for a wide range of applications[106]. Due to the Van der Waals interactions, the as-dispersed GO sheets tend to agglomerate again. The existence of inorganic nanoparticles will prevent the agglomeration of G sheets during the reduction. The specific area of the inorganic materials can be kept at a high level which is required for adsorption, catalysis and other applications [107, 108].

One of the most commonly used techniques to deposit FePt nanoparticles onto G is to firstly fabricate monodisperse FePt nanoparticles with the particle size around 6 nm and then disperse the FePt nanoparticles with hexane into the DMF solution of G[10]. To prepare the monodisperse FePt nanoparticles, the method of chemical reduction of platinum (II) acetylacetonate ($Pt(acac)_2$) and iron pentacarbonyl ($Fe(CO)_5$) is used [109]. However, there are several disadvantages of this method one of which is the surfactant used in the fabrication process of FePt nanoparticles which decreases the contact between the FePt nanoparticles and the reaction solution. What is more problematic, is the FePt nanoparticles fabricated by this method are usually in the face centered cubic (fcc) phase. To obtain the ordered structure of FePt nanoparticles, post annealing is required which however will destroy the assembly of FePt nanoparticles and cause undesirable sintering and agglomeration. In this thesis, a novel solid state fabrication method of FePt nanoparticles on G is introduced. A solution of precursor of $[Fe(H_2O)_6]PtCl_6$ was dispersed into a water solution of GO and after the mixture of $[Fe(H_2O)_6]PtCl_6$ and GO was precipitated, water was

removed. Post annealing was introduced for this mixture under the atmosphere of forming gas (5% hydrogen and 95% argon) at different temperatures varying from 600℃ to 950℃. FePt nanoparticles in the fct phase with a uniform size distribution were fabricated. Even under an annealing temperature as high as 750℃, the FePt nanoparticles still maintain a small and uniform size as well as high coercivity.

6.2 Fabrication and Characterization of FePt Nanoparticles on the Surface of Exfoliated Graphene

6.2.1 Fabrication of FePt Nanoparticles on the Surface of Exfoliated Graphene

To synthesize the $[Fe(H_2O)_6]PtCl_6$ precursor, 0.5 M $H_2PtCl_6 \cdot 6H_2O$ (Aldrich) and $FeCl_2 \cdot 4H_2O$ (Aldrich) water solution were mixed to form the equal atomic solution of $FePtCl_6 \cdot 6H_2O$. The acidity of the solution was kept at pH=1 to prevent the Fe^{2+} to Fe^{3+} oxidation. The reaction to form $FePtCl_6 \cdot 6H_2O$ began immediately after mixing of the reactants with the production of HCl gas.

Figure 46 shows the fabrication process of FePt nanoparticles on the graphene. 40mg GO sheets were exfoliated in water solution by sonication pulses (5s sonication with 15s interval) forming a grey mixture of exfoliated GO and deionized water. The $FePtCl_6 \cdot 6H_2O$ solution was then added to the above mixture with magnetic stirring. The new mixture was kept magnetically stirred for 15 min. After the GO with $FePtCl_6 \cdot 6H_2O$ was precipitated, the top solution was removed and the water was evaporated. The product was then annealed under the atmosphere of forming gas (5% hydrogen and 95% argon) for 30 min at temperatures within the range of 600℃ to 950℃. Two reactions happened during the annealing, one of which is the reduction of GO to G under the reducedatmosphere at high temperature. The other reaction is the following:

$$[Fe(H_2O)_6]PtCl_6 + 3H_2 \rightarrow FePt\ (L1_0) + 6H_2O + 6HCl$$

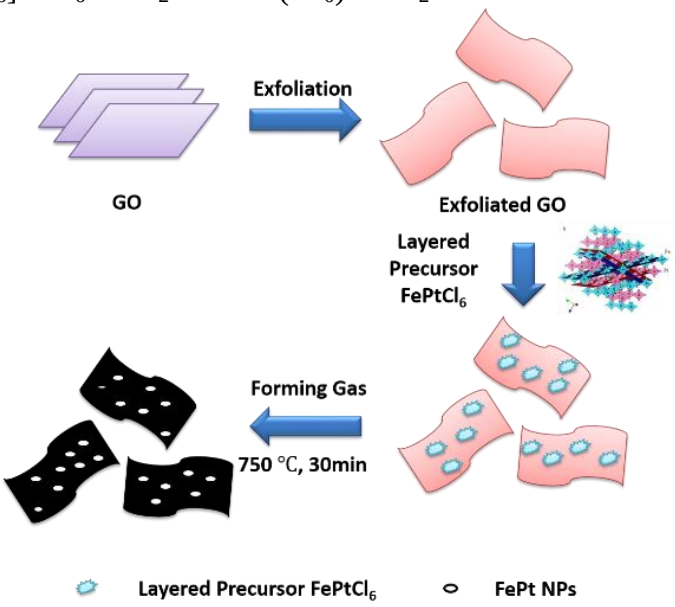

Figure 46 Demonstration of the fabrication process of FePt nanoparticles on the graphene

6.2.2 Characterization of FePt Nanoparticles on the Surface of Exfoliated Graphene

The morphology of FePt nanoparticles on the G sheet, the size and size distribution of FePt nanoparticles were determined by transmission electron microscopy (TEM) (JEOL, JEM-3010) with a voltage of 300 keV. The composition of FePt nanoparticles was determined by X-ray energy dispersive spectrometry (EDS) equipped with the JEM-3010. The crystal structure was measured by both X-ray diffraction (XRD) (Ultima IV with Cu Kα radiation) using a conventional θ-2 θ plane reflection geometry and selected area electron diffraction (SAED) (also equipped with JEM-3010). A Versalab vibrating sample magnetometer (VSM) (Quantum Design) was used to measure the magnetic properties of the samples.

X-ray photoelectron spectroscopy (XPS) measurements were performed under ultrahigh vacuum conditions with a base pressure of 5×10^{-10} mbar in a SPECS GmbH instrument equipped with a monochromatic MgKα source (hν = 1253.6 eV) and a Phoibos-100 hemispherical analyzer. Pulverized samples were dispersed in toluene (1 wt%), and after short sonication and stirring, a minute quantity of the suspensions was drop cast on evaporated gold films supported on mica substrates and left to dry in air before transfer to ultrahigh vacuum. The energy resolution was set to 0.3 eV and the photoelectron take-off angle was 45 °with respect to the surface normal. Recorded spectra were the average of 3 scans with energy step set to 0.05 eV and dwell time 1 sec. All binding energies were referenced to the C1*s* core level at 284.6 eV. Spectral analysis included a Shirley background subtraction and peak deconvolution employing mixed Gaussian−Lorentzian functions, in a least squares curve-fitting program (WinSpec) developed at the Laboratoire Interdisciplinaire de Spectroscopie Electronique, University of Namur, Belgium.

Raman spectra were recorded with a micro-Raman (μ-Raman) Renishaw RM1000 system using a laser diode excitation line at 532 nm in the frequency range of 200–3500 cm^{-1}. Raman scatter was collected by means of an Olympus optical microscope, equipped with 50 × and 100 × lenses. Using the 50 × lens, the probing spot was about 2 μm in diameter, while laser was operated at 20 mW unless photodecomposition occurred and power was decreased. The spectrometer was calibrated by recording the spectrum from a Si sample with characteristic Raman peak at 520.7 cm^{-1}. Raman spectra were obtained from samples in the form of drop casted films onto glass substrates. The reported spectra are an average of 3-5 scans.

6.2.3 Advantages of the Fabrication Method

The main advantage of this fabrication method is to avoid the use of any solvent except deionized water. So there is not any surfactant or organic solvent surrounding the FePt nanoparticles which will improve the contact between FePt nanoparticles and the reactants. The other advantage of this method is that FePt nanoparticles in fct phase were prepared directly from the reduction of crystalline precursor without any intermediate process. A uniform particle morphology and size distribution can also be controlled.

6.3 Results and discussion

6.3.1 One typical example

Figure 47 shows a typical sample of FePt nanoparticles on the G which was annealed under the atmosphere of forming gas at 750℃. The bright-field images Figure 47(a) and 47(b) showed that the FePt nanoparticles are located on the surface of G separately with average size of 8.5 nm. In the most commonly used fabrication method of FePt, annealing at the temperature as high as 750℃ will lead to severe sintering and agglomeration. In the fabrication process demonstrated in this paper, the existence of G successfully prevented the agglomeration of FePt nanoparticles and the size distribution is narrow (shown in Figure 48). The high resolution image Figure 47(c) revealed that the FePt nanoparticles are single crystals and the atomic composition of FePt nanoparticles is $Fe_{56}Pt_{44}$ which is within the composition range of fct phase.

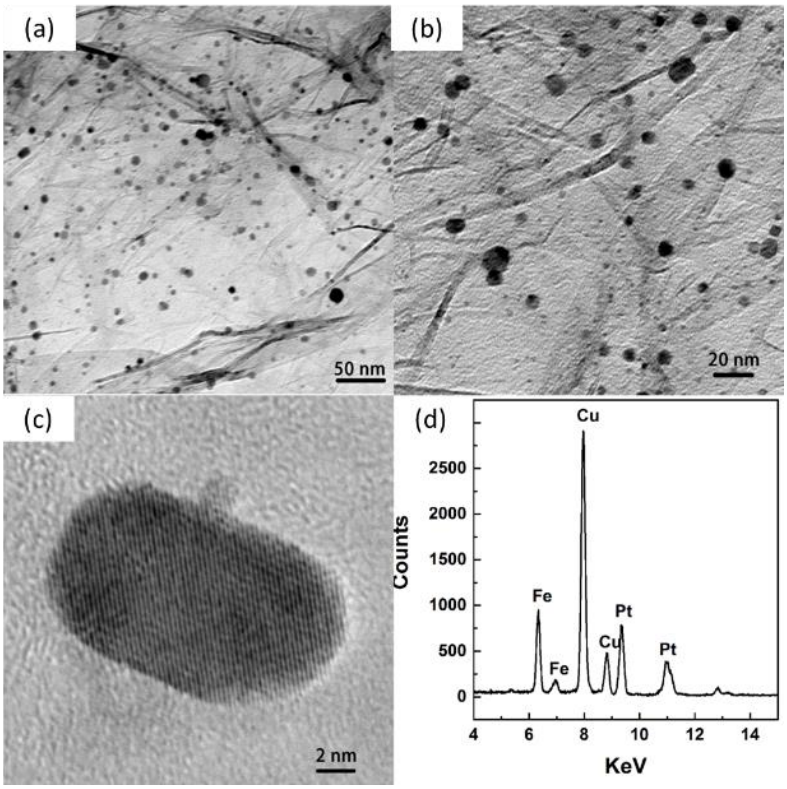

Figure 47 (a) (b) Bright-field images (c) high-resolution image (d) EDAX spectrum of FePt nanoparticles on the G annealed at 750℃

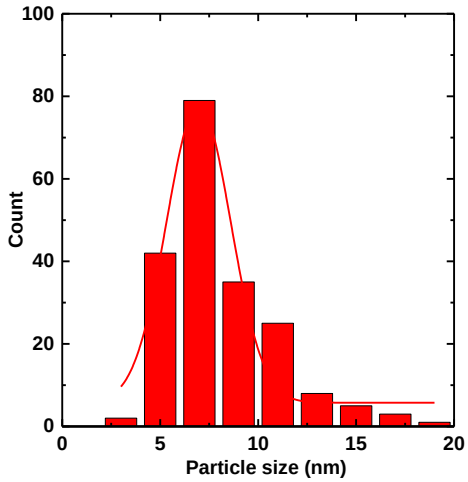

Figure 48 Size distribution of FePt nanoparticles on the graphene annealed at 750℃

In the XRD spectra of Figure 49, the high broad peak at 18 degree is the peak of GO which showed that the reduction of GO to G is not complete at the temperature of 750℃. At 25 degree, a clear peak of G is shown. In fact, the complete reduction from GO to G requires temperatures higher than 1000℃ which will destroy the fct structure of FePt nanoparticles. At 750℃, the characteristic superlattice peaks of (100), (110) and (201) are clearly shown in the XRD pattern as well as the split the peaks of (200) and (002), (220) and (202). All these characteristic peaks showed that the FePt nanoparticles are fabricated in in fct phase. The hysteresis loop in Figure 50 is also a proof of the magnetically hard fct phase of the FePt nanoparticles. With the annealing temperature of 750℃, the FePt nanoparticles have a coercivity of 8.3 kOe. The magnetization value is low (10 emu/g) because the G sheet has a very large surface and the FePt nanoparticles only occupy a small portion of the surface area. The non-magnetic G increases the sample mass.

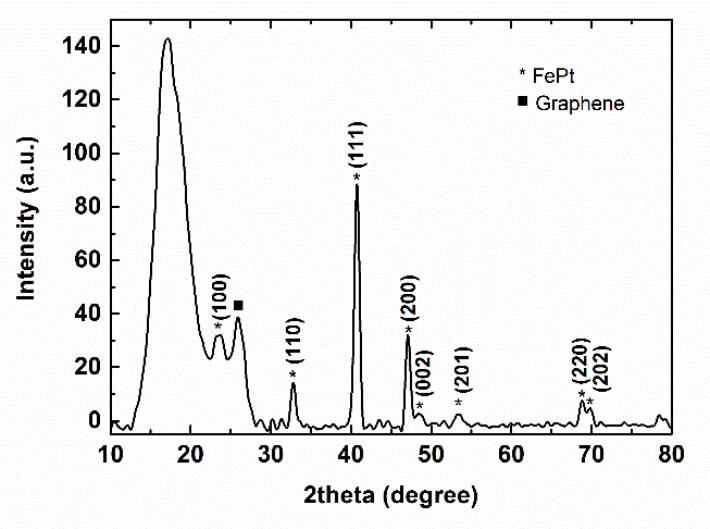

Figure 49 XRD spectrum of FePt nanoparticles on the graphene annealed at 750℃

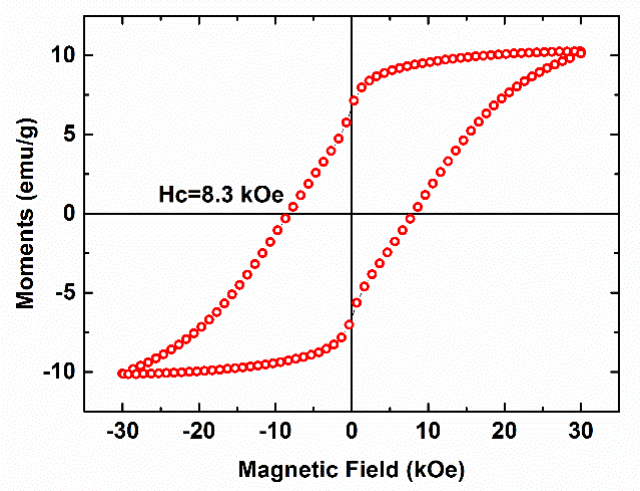

Figure 50 Hysteresis loop of FePt nanoparticles on the graphene annealed at 750℃

The XRD findings for the incomplete reduction of GO towards R-GO are further verified by XPS and Raman spectroscopies. C1*s* core level XPS spectrum and Raman of FePt nanoparticles on the G annealed at 750^{o}C are shown in Figure 51.

After deconvolution with mixed Gaussian−Lorentzian functions, the C1*s* spectrum consists of five components. The first component, recorded at a binding energy of 284.6 eV, corresponds to C-C and C-H bonds and contributes a 20.0% to the total C1*s* intensity. The main peak at 285.6 eV, representing 42.2% of the total C1*s* intensity, is attributed to hydroxyl C-O bonds, while the third peak at 286.5 eV (23.8%) is assigned to C-O-C epoxide/ether groups. The peak at 287.4 eV (11.7%) originates from the carbonyl functional groups (C=O), whereas the higher binding energy contribution located at 288.7 eV (2.3%) is associated with carboxyl groups (O-C=O) [110, 111]. Shape and deconvolution of the C1*s* XPS spectrum strongly suggest that graphene oxide undergoes partial reduction upon annealing at 750^{o}C. This behavior is commonly found with thermal annealing in a reducing Ar/H_2 atmosphere [112]. Although oxygenated groups and mainly C-O still dominate the C1*s* spectrum, reduction is exposed by two facts; a noteworthy contribution from the C-C bonds arises at lower binding energy and the shape of the spectrum exhibits easily visible differences compared to relevant pristine GO C1*s* XPS spectra where the C-C bond usually has minor contribution while more oxidized species as carboxyl and carbonyl groups dominate [110, 112]

On the other hand, Raman spectrum of FePt nanoparticles on the G annealed at 750^{o}C exhibits both G- and D-bands at 1583 and 1349 cm^{-1}, respectively. The G-band at 1583 cm^{-1} which is associated with sp^2 hybridized carbon atoms is asymmetric and shifted compared to the G-band of GO, near the relevant peak of graphite which is positioned at ~ 1580 cm^{-1} [113, 114]. As better observed at the inset of Figure 52, G-band consists of two different peaks, the one derived by pristine GO at ~ 1600 cm^{-1} and a minor sharper one arising from reduced GO at ~ 1580 cm^{-1}. In addition, while

GO does not have significant peaks in the 2D region [115], a broad peak arises at 2690 cm^{-1} in the Raman spectrum of the 750°C annealed sample. This is ascribed to the 2D vibrational mode (overtone of the D peak) and has roughly half the intensity of the G-band [113, 114]. According to literature, the red shift of G-band, the enhanced intensity of the 2D peak as well as its shift below 2700 cm^{-1} are clear evidence of R-GO presence and few layers formation [110, 113, 116]. Unfortunately, in our case the exact number of stacked graphene layers cannot be estimated but due to the broadening of the 2D peak it is rational that there should be a wide distribution concerning the number of the stacked layers.

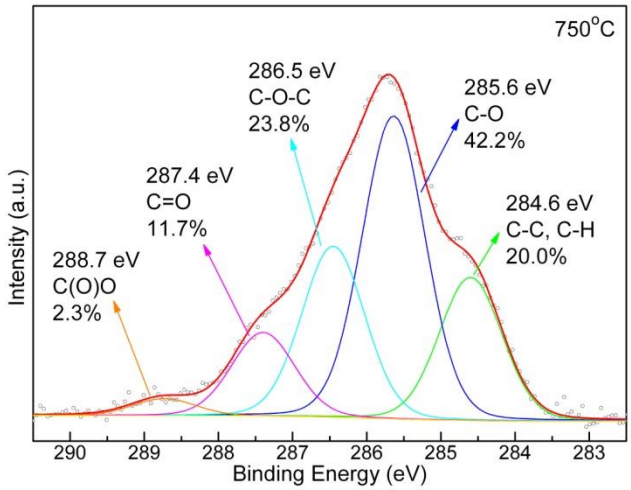

Figure 51 C1*s* core level X-ray photoemission spectrum of FePt nanoparticles on the G annealed at 750°C

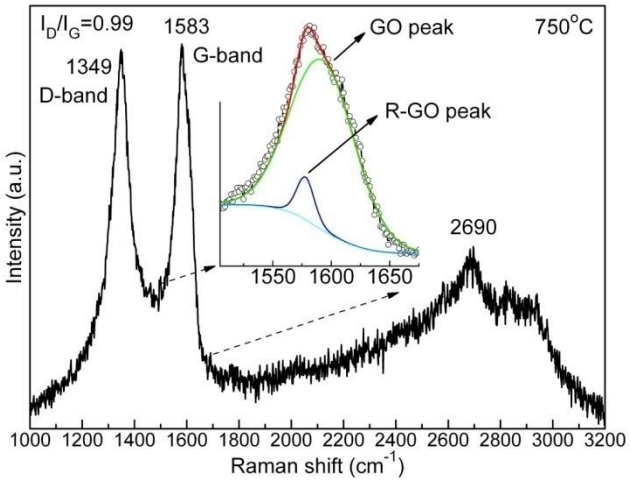

Figure 52 Raman spectrum of FePt nanoparticles on the G annealed at 750°C. Inset of (b): zoom in on the region of the G-band

6.3.2 Effect of annealing temperatures

The annealing temperature has a significant influence on the morphology, size and magnetic properties of the FePt nanoparticles. To further investigate the influence of annealing temperatures, samples with different annealing temperatures of 500℃, 600℃, 750℃ and 950℃ were prepared. Figure 53 showed the morphology, size and crystal structure of the FePt nanoparticles prepared. From the bright field images of FePt nanoparticles from Figure 53(a1) to Figure 53(d1) and Table 8, a clear trend of increasing particle size could be observed. The particle size distribution data from Figure 53(a2) to Figure 53(d2) was obtained by counting the size of 200 particles (More than one bright field images were used for counting) from the bright field TEM images. The FePt nanoparticles annealed at 600℃ and 750℃ have a similar average particle size around 8 nm. The FePt nanoparticles annealed at 500℃ have the smallest particle size of 4.6 nm. All of these 3 samples maintain small and uniform size and the particles are separated without any agglomeration. However, when the annealing

temperature is as high as 950℃, the particle size increases significantly to the average size of 29.8 nm and some very large particles as large as 100 nm are observed. The annealing temperature of 950℃ is too high that causes the growth of particle size (shown in Figure 54). As mentioned before, complete reduction from GO to G requires temperature higher than 1000℃. To maintain a small and uniform size distribution of FePt nanoparticles, annealing temperatures lower than 950℃ are needed which means we can only get a mixture of G and GO. The size distribution of Figure 53(a2) to 53(d2) showed that the 500℃ and 750℃ samples have a narrower size distribution and the 950℃ sample has a bad size uniformity. The high resolution images of Figure 53(a3) to 53(d3) showed that all the samples made are single crystals. However, due to the limitation of the resolution of TEM, we cannot rule out the defects and possible disorder inside the nanoparticles.

Table 8 Average sizes of FePt nanoparticles annealed at different temperatures.

Annealing temperature(℃)	500	600	750	950
Average size (nm)	4.6	8.1	8.5	29.8

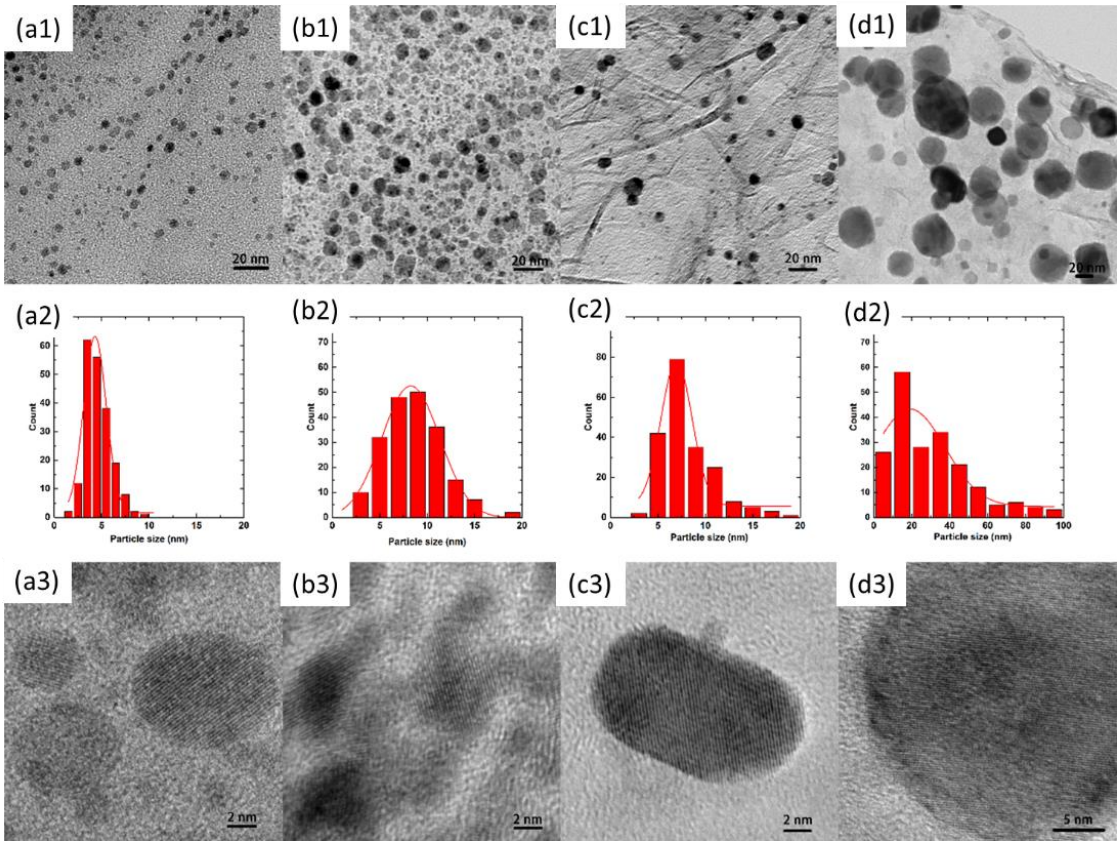

Figure 53 Bright-field images of FePt nanoparticles on the G annealed at (a1) 500 ℃ (b1) 600 ℃ (c1) 750 ℃ and (d1) 950℃, size distribution of FePt nanoparticles on the G annealed at (a2) 500 ℃ (b2) 600 ℃ (c2) 750 ℃ and (d2) 950℃, high-resolution images of FePt nanoparticles on the G annealed at (a3) 500 ℃ (b3) 600 ℃ (c3) 750 ℃ and (d3) 950℃

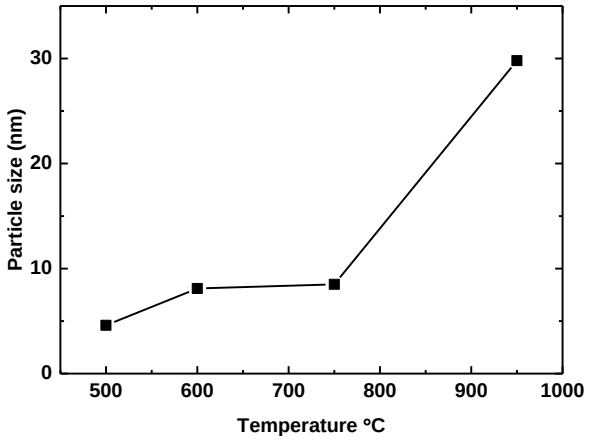

Figure 54 Average particle size of FePt nanoparticles on the graphene as a function of annealing temperature

Figure 55 shows the XRD pattern of the FePt nanoparticles on G with different annealing temperatures. The peaks at around 25 degree with a square mark are the graphene peaks. They are broad and there is a shift of these peaks because the annealing temperatures are not high enough to completely transfer the GO to G which makes a mixture of GO and G. The peaks with star sign are FePt peaks. The XRD pattern of the sample annealed at 500℃ demonstrates typical fcc phase pattern which is in accordance to the reported phase transformation temperature of FePt nanoparticles from fcc to fct (higher than 600℃). When the annealing temperature was increased to 600℃, the (200) peak shifts to higher degree which is also the evidence of larger portion of fct phase. From the XRD pattern of 750℃ and 950℃ samples, the supperlattice peaks of (001) and (110) can be seen and the original (200) splitting to two separate peaks of (200) and (002). All of the above observations are clear signs of face tetragonal phase. For the 950℃ sample, the split of (200) and (002) are more obvious and there is one more superlattice peak of (201) which means there is a larger

portion of fct phase at higher annealing temperatures. The degree of ordering increases with the increase of annealing temperature. Since the size of the nanoparticles is small and there is a width of the peaks, there are possibilities of partial disordering inside the nanoparticles and a small portion of fcc/lower degree of ordering fct nanoparticles.

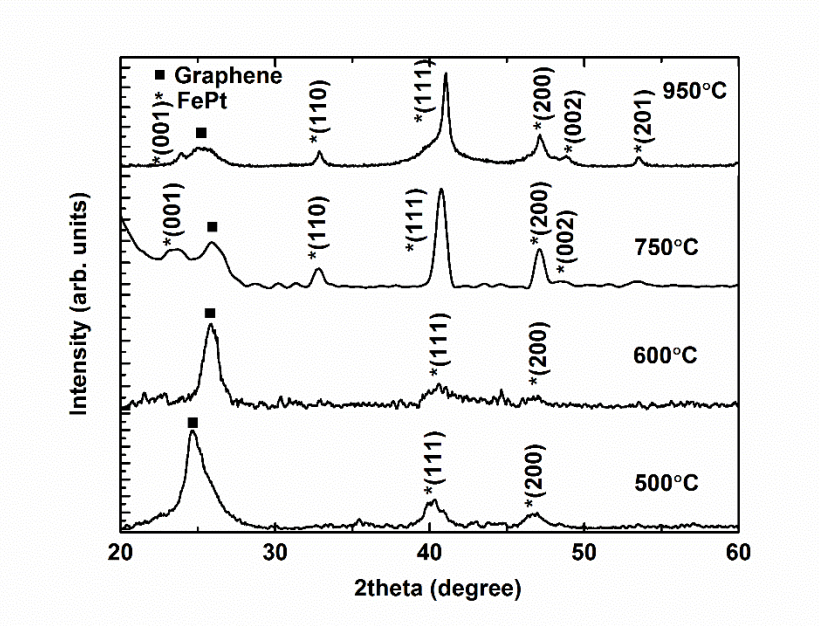

Figure 55 XRD spectrums of FePt nanoparticles on the graphene annealed at 500℃, 600℃, 750℃ and 950℃

Raman spectra of FePt nanoparticles on the G annealed at all four temperatures are presented in Figure 56. As seen there, the D-band is recorded at 1349 cm^{-1} in all cases, whereas the G-band appears at 1593 cm^{-1} except for the 750^{o}C sample as discussed previously. Moreover, samples at 500^{o}C, 600^{o}C and 950^{o}C do not exhibit any important peak in the 2D region in contrary to the 750^{o}C sample. These two observations, the position of the G-band and the lack of any major 2D peaks, suggest

that the annealing process in the reducing atmosphere did not lead to relevant reduction of GO for the rest samples as for the one annealed at 750°C. This conclusion comes in full agreement with the XRD patterns and XPS spectra. Furthermore, the ratio of the D- to G-band intensities (I_D/I_G) is increasing with higher annealing temperatures. I_D/I_G is equal to 0.88 for the first two samples where the temperature variation is small, but reaches 0.99 for the FePt nanoparticles on the G annealed at 750°C and 1.06 for the FePt nanoparticles on the G annealed at 950°C. This is expected and well documented in literature since together with the restoration of the sp^2 graphene lattice, defects and vacancies are also formed, and the same time the full width at half maximum of the D-band is decreasing [112, 117].

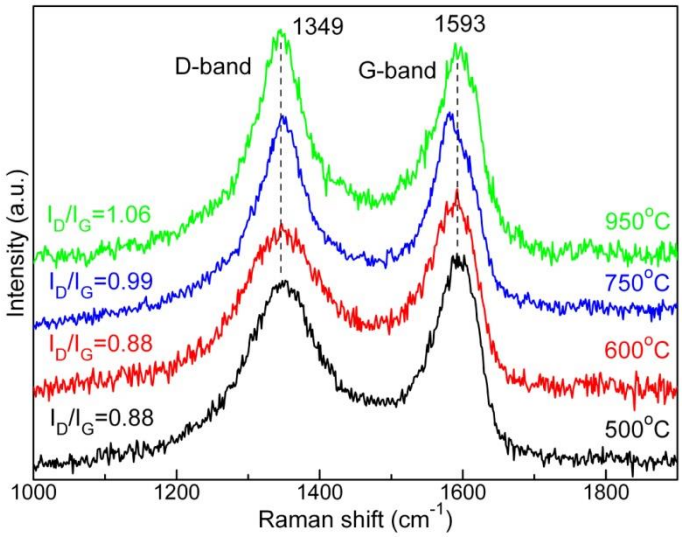

Figure 56 Raman spectra of FePt nanoparticles on the G annealed at 500°C, 600°C, 750°C and 950°C

Figure 57 shows the hysteresis loops of FePt nanoparticles with different annealing temperatures. As discussed before, the annealing temperature of 500°C is

not high enough to form fct phase FePt nanoparticles. The sample is in the fcc phase which is in agreement with the very low coercivity of 0.4 kOe. With the increase of annealing temperature, the coercivity increases since the degree of ordering is higher. Table 9 lists the coercivity of the four samples with different annealing temperatures. When the annealing temperature is higher than 750℃, the samples have high coercivity of 8.1 kOe and 9.9 kOe which agrees with the XRD pattern showing that most of the samples are in the fct phase. The magnetization is low because the weight of non-magnetic G and GO is also counted.

Table 9 Coercivity of FePt nanoparticles annealed at different temperatures

Annealing temperature(℃)	500	600	750	950
Coercivity (kOe)	0.4	3.7	8.1	9.9

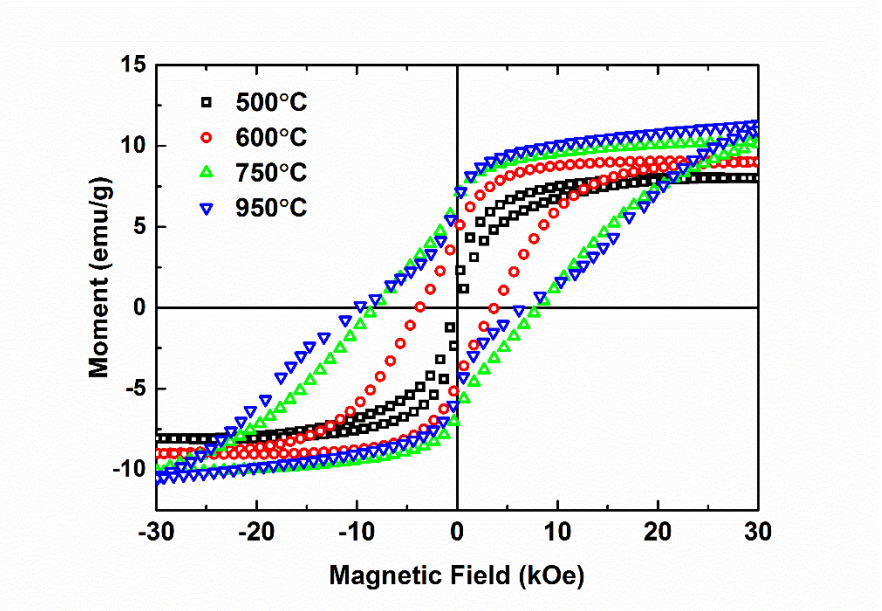

Figure 57 Hysteresis loops of FePt nanoparticles on the graphene annealed at 500℃, 600℃, 750℃ and 950℃

6.4 Conclusions

In this chapter, we described a fabrication method to directly prepare FePt nanoparticles in the fct phase on the surface of R-GO (Reduced Graphene oxide). To the best of our knowledge, this is the first time that magnetically hard nanoparticles on G are synthesized by a solid phase reaction. After mixing the layered precursor $Fe[(H_2O)_6]PtCl_6$ with GO, separate FePt nanoparticles in magnetically hard fct phase were obtained by annealing under the reduction atmosphere (5% H_2, 95% Ar). The influence of annealing temperature on the morphology, size, structure and magnetic properties was investigated. With an annealing temperature higher than 600℃, the transformation from fcc phase to fct phase began. For annealing temperatures as high as 950℃, the particle size increases significantly to 29.8 nm and the size distribution becomes wider. The 750℃ is an optimum annealing temperature to maintain a small particle size of 8.5 nm and high coercivity of 8.1 kOe.

6.5 Proposed future work

We successfully fabricated well separated FePt nanoparticles with high coercivity on graphene surface. However, the results discussed in this thesis are only prelimimary results and much work remains to be done.

1. This fabrication method can also be used to prepare CoPt and FePd nanoparticles on the surface of graphene by simply changing the starting salts to prepare layered precursor

2. The reason for the separated nanoparticles needs to be figured out. The influence of the coverage of the precursor on the graphene surface requires further investigation.

3. There is a difference of the temperature to obtain $L1_0$ phase FePt nanoparticles compared to the fabrication method in Chapter 5. The ordering behavior of FePt nanoparticles needs to be investigated.

Chapter 7

ORDERING OF FEPT NANO-ISLANDS EPITAXIALLY GROWN ON MgO

7.1 Introduction

Development of ultrahigh capacity magnetic storage technology requires media with high areal density. The major challenge for the hard drive industry is that the current Co based alloy is reaching its theoretical limit, which means with decreasing grain size the thermal energy at room temperature can demagnetize the small grains and result in the loss of stored information[118]. As mentioned before, in the search for substitute materials, $L1_0$ magnetic alloys have been attracting intensive attention due to their large magnetocrystalline anisotropy energies (MAE) and better corrosion resistance compared with rare-earth based alloys The high MAE density ensures that the FePt units (grains, particles) with stable magnetization at room temperature can be as small as 2.5 nm.

A large amount of research has been conducted in the fabrication of FePt and CoPt nanoparticles and nano islands. Different techniques have been reported in the synthesis of the nanostructures including wet-chemistry, evaporation, sputtering, and gas-phase deposition [15, 119-124]. Recent efforts have been focused on decreasing the size of the particles for magnetic storage media with terabit/in^2 density. However, with decreasing particle size, it was found that even after long annealing, the coercivity of the nanoparticles was still low. In the past few years, the size-dependent ordering effect has ignited intensive experimental and theoretical studies on the ordering and phase transformation of FePt nanoparticles to reveal the origin of the low

coercivity of the small particles [125-131]. Microstructural investigation has been done to study the size and the ordering of the nanoparticles. Surface segregation has been reported to be one of the possible causes of the reluctance in ordering[123].

Recent studies suggest that the annealing temperature for the ordering is size dependent [122, 124]. Particularly, with decreasing particle size, difficulties in acquiring ordered $L1_0$ FePt or CoPt nanoparticles were reported. It has also been reported that no ordering takes place upon annealing nanoparticles with a diameter smaller than 4 nm [132]. Theoretical calculations show that at a typical annealing temperature of about 600°C, highly ordered $L1_0$ nanoparticles with a diameter of 3.5 nm can be achieved [129]. Miyazaki's experimental work put this size limit down to 2 nm [43]; however more recent work demonstrates that ultra-small (~2 nm) FePt nanoparticles can also be fully transformed to the $L1_0$ phase [133, 134]. These varying and sometimes contradictory results reflect the complexity of the issues surrounding the FePt $L1_0$ ordering or the nano-phase transformation.

In this chapter, we studied the microstructure of FePt nano-islands sputtered on MgO(001) substrate utilizing C_s corrected (both probe and image corrected) (Scanning) Transmission Electron Microscope ((S)TEM). Different from the nanoparticles synthesized with chemical methods or deposited on amorphous substrates, the epitaxial relationship between the substrate and the nanoparticles ensures that for most nanoparticles, the (001) plane is parallel to the beam direction during the cross-sectional TEM observation. This is the ideal orientation to unambiguously determine the ordering. In addition, other than determining the atomic ordering from a diffraction pattern which averages among different particles, the C_s corrected (S)TEM provides the opportunity for direct observation of atomic scale

information inside individual nanoparticles with unprecedented resolution and accuracy. The effect of substrate is also evaluated.

7.2 Experimental Methods

An alloy target with composition of $Fe_{50}Pt_{50}$ was used to fabricate the FePt islands. Samples consisting of FePt nano-islands with size varying from 5 to 20 nm were prepared by annealing DC magnetron sputtered $Fe_{50}Pt_{50}$ thin films on MgO(001) substrate. The sputtering base pressure and Ar sputtering pressure used were 3×10^{-7} Torr and 5 mTorr, respectively. The substrates were one-side polished MgO (001) single crystals, which were heated up to 500℃-700℃ before sputtering to ensure cubic-cubic epitaxial growth of the FePt thin films. Film growth rate was 0.15 nm/s. Different sputtering times from 5 to 25s were applied to investigate how different sputtering conditions influence the size and structure of the FePt islands. The as-sputtered samples were annealed at 600 ℃ for 30 min to obtain $L1_0$ ordered FePt islands.

The island size was determined by transmission electron microscopy (TEM) (JEOL JEM-3010) with a voltage of 300 keV. The morphology and magnetic domains were made by atomic force microscopy (AFM) and magnetic force microscopy (MFM), respectively using an NT-MDT unit. The actual elemental composition of FePt islands was quantified by energy dispersive X-ray spectroscopy (EDS) (JEOL JEM-3010). The structure and chemical ordering parameter was determined from X-ray diffraction (XRD) spectra (Ultima IV) by using a conventional θ-2θ plane reflection geometry with Cu Kα radiation. Magnetic properties were measured by vibrating sample magnetometer (VSM) from Quantum Design.

Atomic scale observation of the ordering of annealed FePt nano-islands was carried out on the TEAM-0.5 microscope, a double-aberration-corrected (scanning) transmission electron microscope (STEM/TEM) capable of producing images with 50 pm resolution. TEAM-0.5 is equipped with a monochromator and two CEOS hexapole-type spherical aberration correctors for probe and imaging corrections separately and is capable of producing images with 50 pm resolution. For aberration-corrected high-angle annular dark-field imaging in STEM mode, in order to decrease the beam damage to the particles, which may lead to particle degradation, the microscope was set to work on 80 kV at the sacrifice of image quality. However, a charging effect was observed at such a low voltage due to the non-conductive MgO substrate. Phase contrast high resolution TEM (HRTEM) images and images for focal-series reconstruction were taken at 300 kV. Although the image interpretation for the phase-contrast imaging is usually not as straightforward as for the Z-contrast imaging, the reconstructed phase images are not affected by lens aberrations and defocusing, which make it possible to eliminate the imaging artifacts that may complicate the interpretation of HRTEM images. Furthermore, the phase-contrast image has the advantages of more accurate determination of atomic positions. The reconstruction of the focal-series of C_s-corrected HRTEM images was performed using MacTempas software. For reconstruction, 50 successive images were selected from 100 focal-series images taken at C_s=-0.1 μm with a focus step of 1 nm.

7.3 Results and discussion

7.3.1 Epitaxial growth and morphology of $L1_0$ FePt islands

Figure 59 shows the planar-view bright-field image of FePt islands deposited at the substrate temperature of 600℃ for 10 s. With a deposition rate of 0.15 nm/s, the nominal thickness of this sample is 1.5 nm. The image demonstrates well separated nano-islands. Figure 59(b) and 59(c) are high-resolution and bright-field images of the cross-section view of FePt islands with the same deposition condition. Together with the selected area electron diffraction (SAED) pattern, where both fct-FePt(001) and fct-FePt(110) spots are shown, these images give a direct evidence of epitaxial growth of $L1_0$ FePt islands where the surface energy of (001) plane is the lower. When the island size is small, the surface and interfacial energies are larger than the volume free energy, and therefore it is relatively easy to form epitaxial texture. The stripe contrast observed in Figure 59(a) is the Moire pattern resulted from the lattice parameter difference between FePt (a_{FePt}=0.40 nm) and MgO(001) (a_{MgO}=0.42 nm). This mismatch of lattice parameters is also demonstrated in Figure 59(b) where plane distortions are observed showing that the fabricated FePt islands are not perfectly ordered.

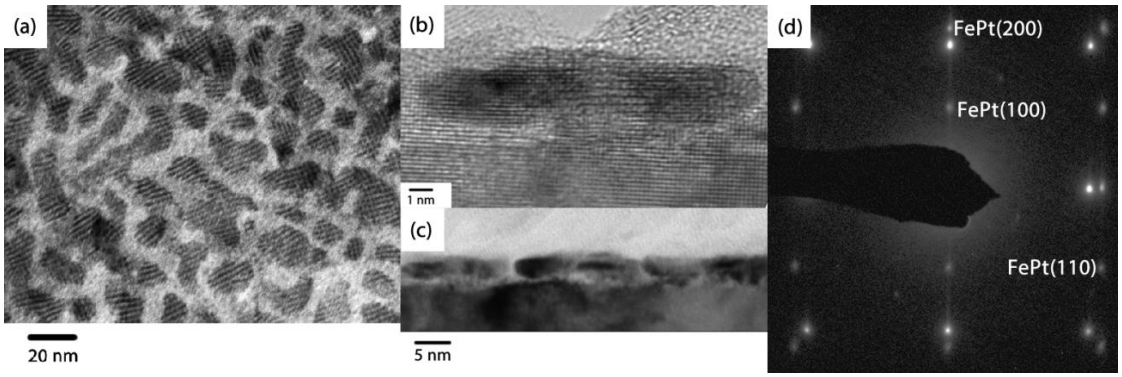

Figure 58 TEM pictures of FePt islands deposited at 600℃ for 10s (a) planar-view bright-field image, (b) high resolution cross-sectional image, (c) cross-sectional view bright-field image and (d) selected area diffraction pattern of cross-sectional FePt islands

Figure 60(a) and 60(b) show the 2-dimensional and 3-dimensional morphology of FePt islands deposited at 600℃ for 10s. The average roughness calculated is 0.483 nm which means that the surface of the prepared FePt islands is rather smooth. This conclusion also is in accordance with Figure 59 (b) where the FePt islands show a flat morphology. The area peak-to-valley height is 5.3 nm which also agrees with the cross-sectional image showing that the nominal thickness of FePt islands is around 4-5 nm. Cross-sectional data of 3D AFM images reveal that the grain size is between 15-20 nm which is in agreement with the size distribution in Figure 61. From the 2D and 3D MFM images in Figure 60(c) and 60(d), the sharp black and white color contrast shows that the easy axis of FePt islands is out-of-plane (along the c-axis). The 3D image also reveals the inter-connection of FePt grains which is also observed in plane-view images.

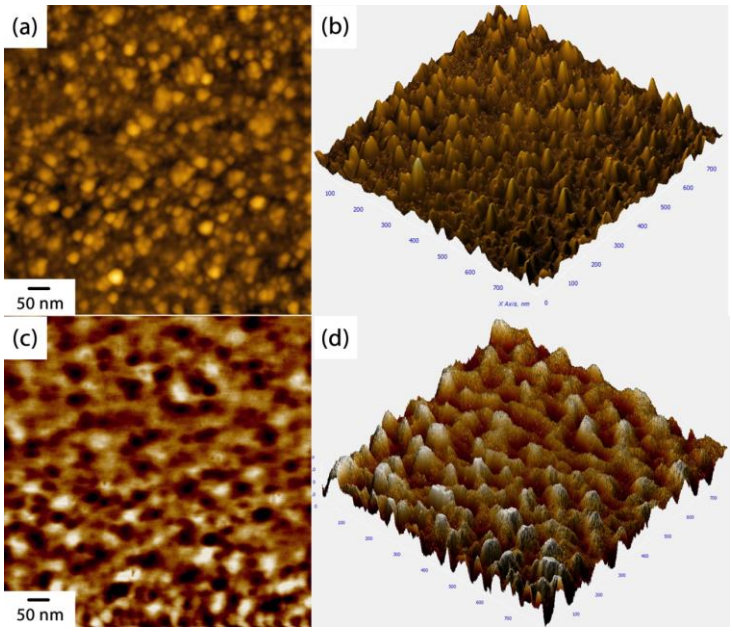

Figure 59 AFM and MFM images of FePt islands deposited at 600℃ for 10s (a) 2D AFM image, (b) 3D AFM image, (c) 2D MFM image and (d) 3D MFM image

7.3.2 Influence of Deposition Conditions on the Morphology, Structure and Magnetic Properties

Figure 61 shows the planar-view bright-field TEM images and size distribution of FePt islands deposited for 10s at different substrate temperatures: (a)(d) 500℃, (b)(e) 600℃ and (c)(f) 700℃. With the increase of substrate temperature from 500℃ to 700℃, the grain size increases from 14 nm to 22 nm. Some very small particles with size below 5 nm are observed in all the three images. For substrate temperature from 500 to 600℃, the amount of particles below 5 nm decreases and the islands become more inter-connected. The particles with size larger than 30 nm account for the inter-connected islands. However, when the substrate temperature rises to 700℃, because of the higher diffusion coefficient, the islands have a more uniform shape and there are some larger separated particles with size larger than 30 nm. Figure 62 shows

planar-view bright-field TEM pictures of FePt islands sputtered at 600℃ with different deposition time, (a) 10s, (b) 15s and (c) 20s. As expected, as the sputtering time increases, the islands become more inter-connected.

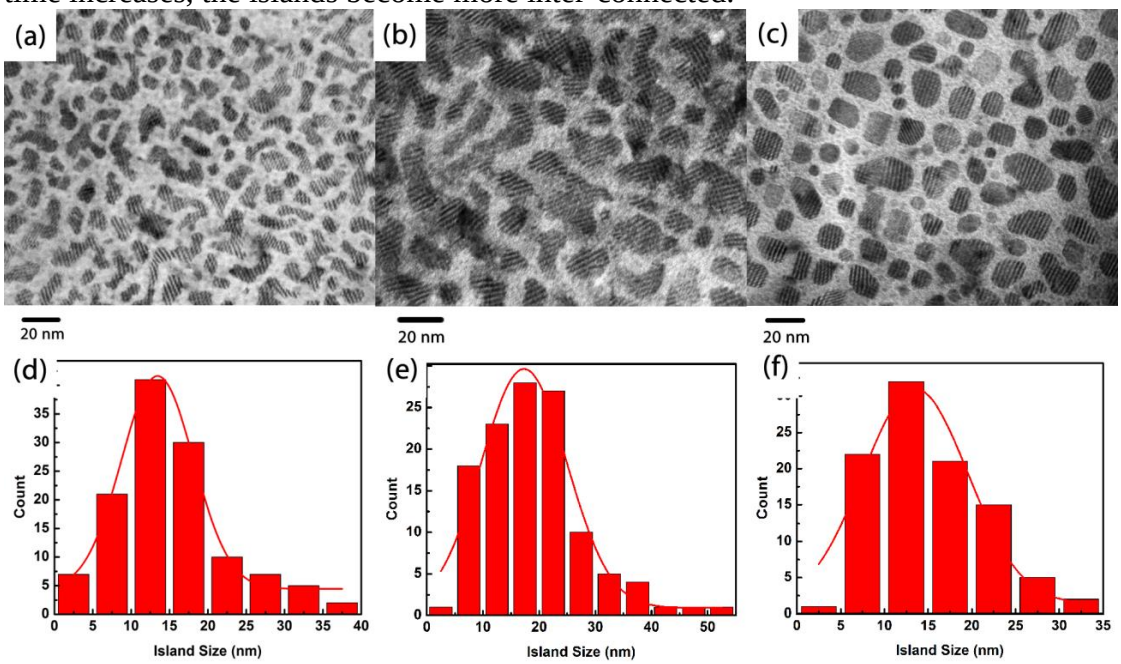

Figure 60 Planar-view bright-field images of FePt islands deposited for 10s at (a) 500℃, (b) 600℃ and (c) 700℃. Size distribution of FePt islands deposited for 10s at (d) 500℃, (e) 600℃ and (f) 700℃

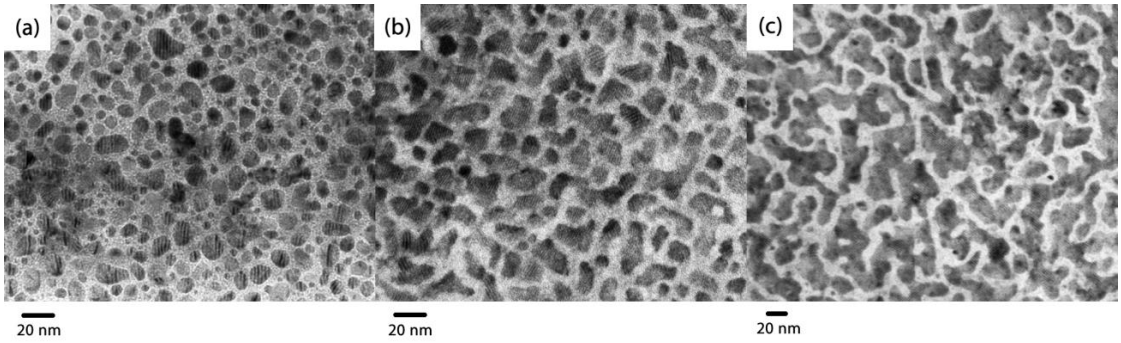

Figure 61 Planar-view bright-field images of FePt islands deposited at 600℃ for (a) 10s, (b) 15s and (c) 20s.

Figure 62(a) shows the XRD spectra of FePt islands deposited at different substrate temperatures from 500℃ (c) to 700℃ (a). The sample deposited at 500℃ has a very weak fct-FePt (001) peak. With the increase of substrate temperature, the (001) peak becomes sharper and stronger indicating grain growth and improvement of ordering. Also, a shift of fct-FePt (002) peak to higher angle between 45° and 50° is observed. As the c-axis of fct-FePt phase is smaller than the a-axis, the shift of the peak suggests that the islands become more ordered. The degree of chemical ordering of FePt islands can be quantified by the long-range ordering parameter S which can be calculated by the following formula:

$$S = \left[\left(\frac{I_{001}}{I_{002}}\right)\left(\frac{F_f}{F_s}\right)^2 \frac{(L \times A \times D)_f}{(L \times A \times D)_s}\right]^{\frac{1}{2}} \cong 0.85\left(\frac{I_{001}}{I_{002}}\right)^{\frac{1}{2}}$$

Where I_{hkl} is the integrated intensity, F the structure factor, L the Lorentz polarization factor, A the absorption factor, D the temperature factor, and the subscripts f and s refer to the fundamental and superlattice peaks respectively.[92] Figure 62 (b) shows the ordering parameter S as a function of substrate temperature. As the substrate temperature increases, the degree of ordering increases which agrees with the shift of the fct-FePt (002) peak between 45° and 50°.

XRD patterns are shown in Figure 63(c) for FePt islands deposited at 600℃ for different times (from top (a) to bottom (d) are 10s, 15s, 20s and 25s respectively). A clear increase of the intensity of fct-FePt (001) peak can be found indicating that longer deposition times can improve the ordering of FePt islands. The calculated ordering parameter also shows the same tendency of increasing from 0.6 to 0.7 as the sputtering time extends from 10 to 25 s.

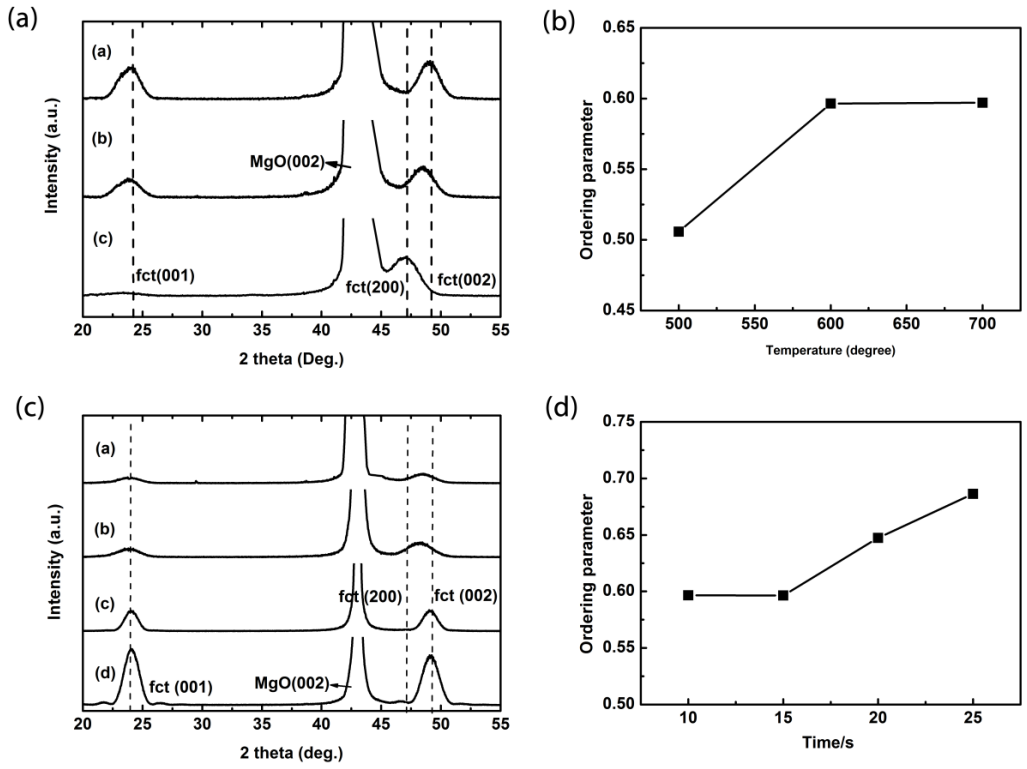

Figure 62 θ-2θ XRD pattern of FePt islands deposited at (a) different substrate temperatures and (c) different sputtering times. Ordering parameter of FePt islands deposited at (b) different substrate temperatures and (d) different sputtering times

The highest coercivity observed is 5kOe for the sample prepared at 600℃ for 25 s as is shown in Figure 63. There are several possible reasons for the relatively low coercivity. The most important one is the imperfect epitaxial growth of FePt islands which is demonstrated in Figure 59(b) due to the crystal mismatch between MgO substrate and FePt. Also, the deposition rate is 0.15 nm/s which is relative high for epitaxial growth of thin films with good perpendicular structure.[135] The deposition time is less than 25s which is too short for the energy transfer for the diffusion to re-order the atoms. From the discussion below with the ultra-high resolution TEM and

HAADF images, different types of defects were found in the fabricated nano-islands which significantly decrease the degree of ordering and a local mixture of order-disorder phase are observed. This type of defects is most probable the reason for the low coercivities. Another possible reason is the wide size distribution of FePt islands introduced by the growth mode of magnetron sputtering. The dominating mechanism in small single-domain particles is the rotation of the magnetization including incoherent process such as buckling. But for the inter-connected islands, whose sizes are over 30 nm, nucleation of reversed magnetic domains becomes significant resulting in decrease of coercivity due to a low resistance to movement of the nucleated domain walls within the inter-connected regions[42].

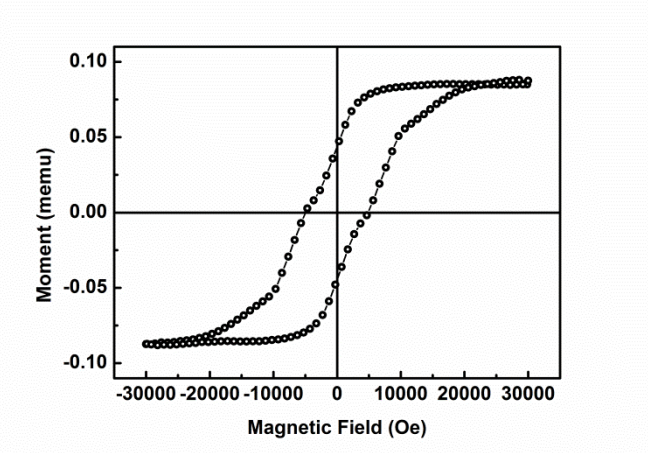

Figure 63 Hysteresis loop of FePt islands deposited at 600℃ for 25s

7.3.3 Ordering Study of the Annealed FePt Nano-Islands

Because of the epitaxial growth of FePt nano-islands, coercivities higher than 10 kOe are expected. However, the highest coercivity we obtained in our as-made samples is only 5 kOe. To improve the magnetic properties, post annealing at 600°C for 30 min was introduced. The XRD profile of the sample after annealing at 600°C

for 30 min shows epitaxial growth of FePt. The strong (001) superlattice diffraction indicates the transition from the disordered *fcc* to the ordered *fct* phase (Figure 65). The shoulder next to the right of this peak is strain induced (001) peak from MgO substrate. Planar view TEM bright field image reveals the formation of islands. The size of these islands ranges from 3 nm to 7 nm with an average size of about 5 nm. The composition of the particles is $Fe_{50}Pt_{50}$ with a dispersion of 6%. The hysteresis loop observed at room temperature confirms the ordering of the FePt islands, but the shape of the loop indicates an inhomogeneity of the sample (Figure 66). The loop shows clearly the presence of magnetically soft and hard phases in the magnet as indicated by the kink in the second quadrant of the loop.

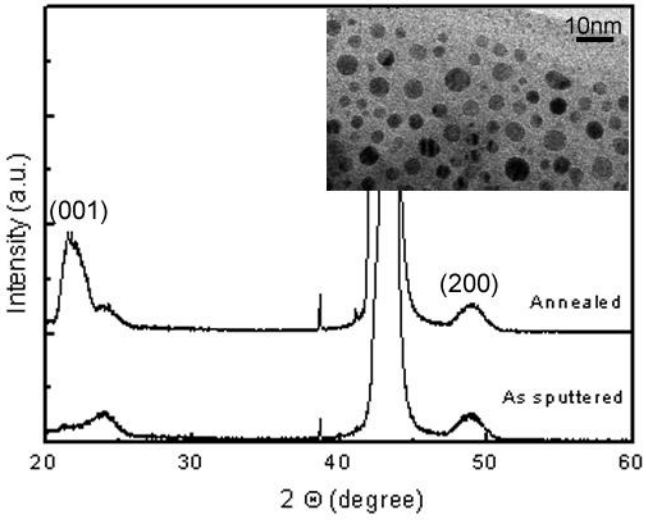

Figure 64 XRD pattern of the FePt nano islands annealed at 600 °C. The inset shows the TEM bright field image from the planar view of the sample

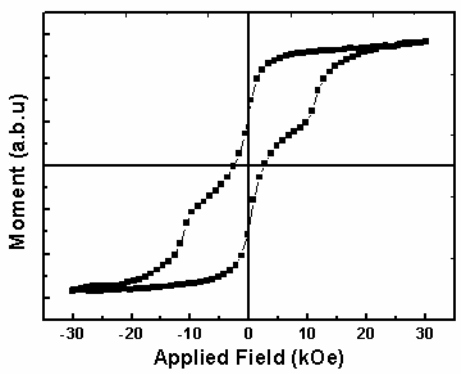

Figure 65 Magnetic hysteresis loop of the sample at room temperature

For the investigation of atomic ordering of the particles, cross-sectional TEM observation is precisely suited for this work considering the epitaxial growth of the nano-islands has an inherent orientation reference offered by the interface or the substrate. Both HRTEM and HAADF (high angle annular dark field)-STEM were employed. The advantage of HRTEM is its uniform and lower dose associated with less likelihood of beam damage and phase transition. Particularly, here HRTEM image is reconstructed from focal series images, and during reconstruction, the artifacts that interfere with phase interpretation can be removed. The Cs corrected HRTEM image shows an FePt island with a diameter of about 6 nm (Figure 67). The fast Fourier transform of the particle image reveals the *fct* ordering (Figure 67(a)). From the reconstructed image, the phase profile along the atomic column shows alternate phase change, which is the evidence of ordering along the c-axis of the *fct* FePt particle (Figure 67(b) and 67(c)).

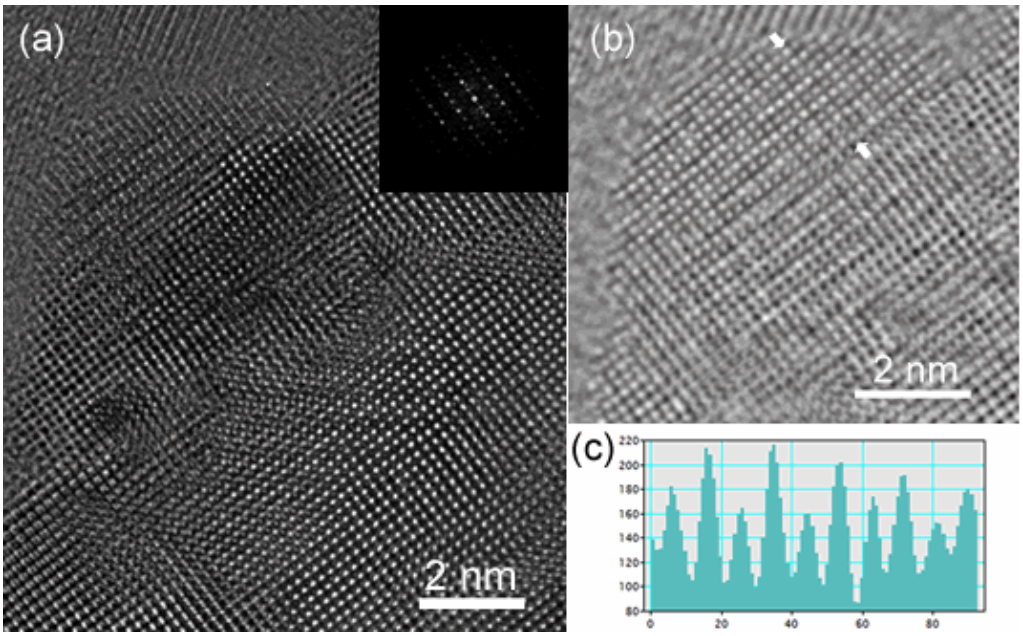

Figure 66 (a) Cs-corrected HRTEM image of the islands, the inset being the fast Fourier transform of the island; (b) Phase image of exit-wave reconstruction result of a FePt nano island. (c) Profile of shell-wise oscillatory contrast variation extracted from the atomic columns marked with arrows

Ordering of FePt nano-islands as small as 3 nm was discovered both in HRTEM and HAADF-STEM observations (Figure 68). It is interesting to notice that in Figure 68(b), the c-axis of the islands is parallel to the substrate surface. On the surface of the island shown in Figure 68(b), the lower contrast between Fe and Pt layer indicates a lower ordering near the surface of the island. In the STEM observation, it is noticed that near the surface of the island, there are two continuous Pt layers along the c direction (Figure 69). It means even though ordering was detected from the XRD pattern, there are defects in the islands that may affect their anisotropy field.

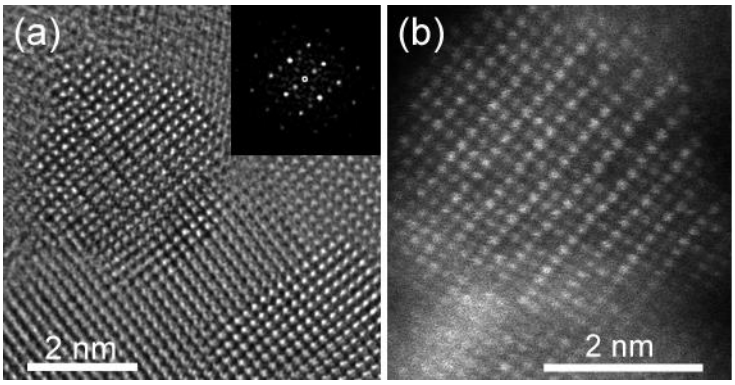

Figure 67 (a) HRTEM image of an ordered FePt island; the inset fast Fourier transform showing the c-axis parallel to the substrate surface; (b) HAADF-STEM image of a FePt nano island

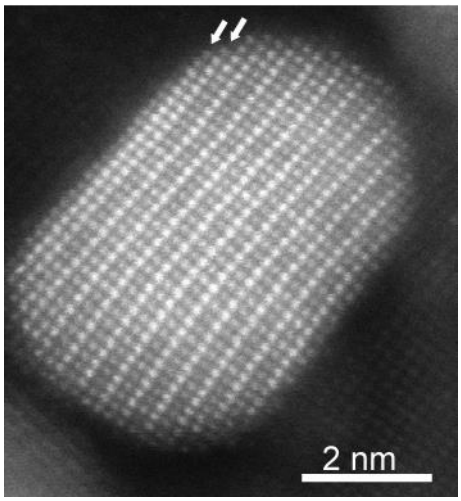

Figure 68 HAADF-STEM image of a FePt nano island, the arrows indicating two continuous Pt atomic layers

Significantly, a unique structure was observed as shown in Figure 70. In this image, orthogonal double periodicity appears on the surface of the particle, which is the evidence of *fct* ordering. However, the c-axis of the ordered domains in either the

left or the right side of the particle is not perpendicular to the substrate, but instead parallel to the surface of the substrate. Therefore, the particle is surrounded by (001) planes from all directions. From a symmetry consideration, it is plausible to assume that in the other two directions perpendicular to the paper, a similar phenomenon happens. Due to the interference among these domains, the center of the island shows a complicated pattern. Similar phenomenon was reported in CuAu nanoparticles, but in FePt system, to the best of the authors' knowledge, this is the very first time to reveal such a structure [93]. The structure consists of six domains and these domains are perpendicular to each other and form an intermetallic onion as detailed in Figure 71(a)-(d). At the interface, each domain is sharing the planes with two other adjacent domains to form *c*-domain boundaries as shown in Figure 71(b). To confirm the structure of this particle, a structure model was constructed in Figure 71(c). The cross-section of this model is shown in Figure 71(d).

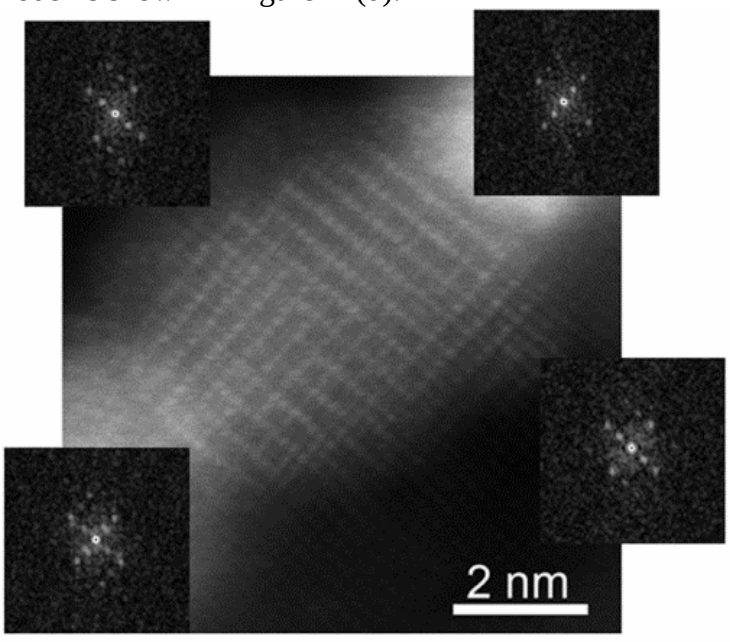

Figure 69 HAADF-STEM image of a FePt nano island, the insets showing Fast Fourier Transforms corresponding to different regions in the island

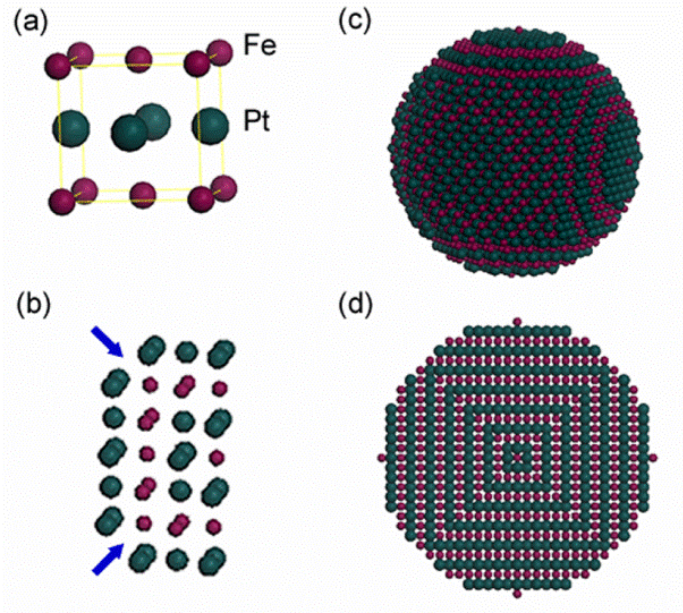

Figure 70 Atomic model of (a) $L1_0$ FePt; (b) c-domain boundaries, the arrows labeling the c-domain boundaries; (c) a particle of the onion like island shown in Figure 5, and (d) the cross section of (c)

An HR-STEM image was simulated suing QSTEM software based on the model (Figure 72). All the experimental parameters are used as input for the image simulation process. The simulated image shows excellent match with the experimental image except for the global shape difference. Near the center of the island, the interference between the different domains leads to the deviation of the contrast of the STEM image from that of *fct* FePt image. While near the surface of the island, along the beam direction, there is no domain overlapping and the simulated image shows exactly what is revealed by the HR-STEM image perpendicular to the c-axis of *fct* FePt in individual domains with different c-axis orientations (Figure 70).

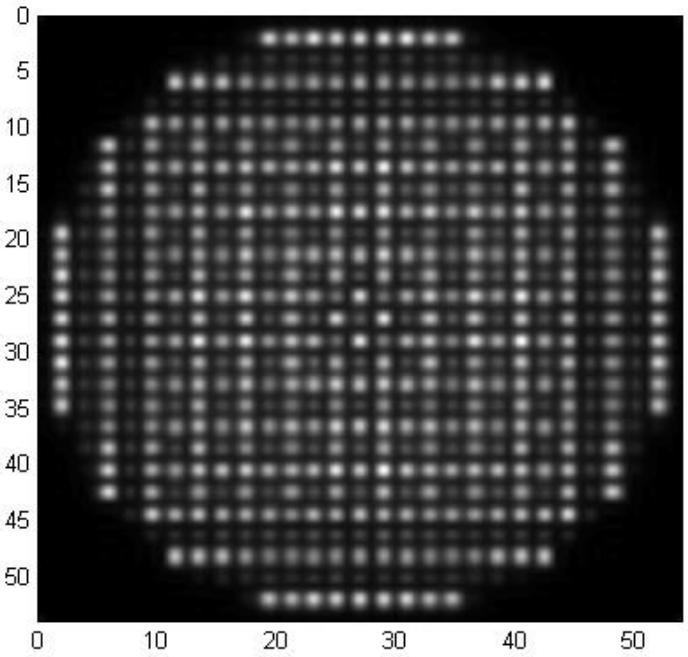

Figure 71 Simulated HAADF-STEM image based on the model shown in Figure 7(c), the unit for both axes is Å

During the transformation from disordered *fcc* to *fct* ($L1_0$), any of the three <010> axes of the cubic matrix may be taken as the tetragonal *c*-axis, which leads to a complex hierarchic arrangement of the microstructure. A variety of planar defects have been reported in FePt bulk alloys and nanoparticles [136-138]. The slight difference in lattice parameters of the *fcc* and $L1_0$ phases causes strain at the interfaces of the domains with different orientations. The energy increase may be compensated by a decrease in surface energy due to the unique structure of the island. Theoretical calculations show that the surface energy in (001) and (100) facets is much lower than in (110) and (011) facets, and is slightly higher than in the (111) facet of $L1_0$ FePt [139]. Multi-twinned structures are theoretically favorable and have been observed in

experimental work [134, 140, 141]. The *c*-domain boundary is also predicted to be the lower energy planar defect in $L1_0$ FePt [93, 142]. The MgO substrate in current work also restricts the types of the planar defects that may occur in the islands. For example although the (111) twins and multi-twinned decahedral structure may be energetically more favorable on free-standing particles as they have been widely discovered, these defects may increase the interface energy between the islands and the MgO substrate. Therefore, in the current work, we did not even find any of such defects in our sample.

All the defects discovered in the present work may substantially affect the magnetic performance considering the size of the particles. The deviation of the atomic position from the ideal structure changes the anisotropy field of the particles, and thus the coercivity. The onion like particles formed from perpendicular *c*-domains may not even show any hard-magnetic behavior considering the different orientations of different domains and the lattice distortion extended from the domain boundaries [143].

7.4 Conclusions

In summary, different defects have been revealed through Cs-corrected (S)TEM in FePt nano islands on MgO(110) substrate. Despite the fact that X-ray diffraction shows atomic ordering in the islands, the lattice distortion, atomic segregation and planar defects in these islands possibly lead to deteoration of the hard magnetic properties. Although there has been long term disputing regarding the size effect on the ordering, our work shows that the *fcc* to *fct* transformation does happen in particles as small as 3 nm. However the defects in the ordered $L1_0$ particles can substantially decrease the coercivity.

Chapter 8

CONCLUSIONS

In this dissertation, we have investigated different fabrication methods to prepare FePt nanoparticles/nanostructures in the magnetically hard $L1_0$ phase. Two novel chemical synthesis routes and the traditional physical vapor deposition technique were used for the synthesis. The structural, microstructural, magnetic properties and the chemical ordering behavior of the synthesized FePt nanoparticles were investigated.

To be more specific, both of the two novel chemical synthesis methods involve a crystal molecular precursor $Fe(H_2O)_6]PtCl_6$ which has a special layered structure with Fe and Pt planes layered alternatively. This structure is the similar with the structure of $L1_0$ phase FePt alloy which is studied in this dissertation. Due to the structural similarity, significant lower temperature (400℃ compared to the commonly used 600℃) is needed to obtain the $L1_0$ phase. A qualitative model was introduced to explain the temperature decrease.

However, direct annealing the precursor produces porous bulk FePt which is not desirable. Two techniques were applied to decrease the sample size from bulk to nanoscale. The first technique is planetary ball milling. By ball milling of the $[Fe(H_2O)_6]PtCl_6$ precursor in a NaCl matrix and annealing at 400 ℃ in reducing atmosphere, we obtained FePt $L1_0$ nanoparticles with different $[Fe(H_2O)_6]PtCl_6$ / NaCl ratios. By varying this ratio, we were able to obtain single crystal nanoparticles with size around 6 nm.

The second technique is to introduce exfoliated graphene support. We prepared FePt nanoparticles in $L1_0$ phase on the surface of reduced graphene oxide through solid-state reaction. After mixing the layered precursor $Fe[(H_2O)_6]PtCl_6$ solution with exfoliated graphene oxide, separate FePt nanoparticles in $L1_0$ phase were obtained by annealing under the atmosphere of forming gas. With an annealing temperature higher than 600℃, the transformation from fcc phase to fct phase took place. Even with an annealing temperature as high as 750℃ (at this temperature, severe agglomeration and sintering usually happened using the common fabrication method), we succeeded to maintain a small particle size of 8.5 nm and high coercivity of 8.1 kOe. When the annealing temperature was further increased to 950℃, the particle size increases significantly to 29.8 nm and the size distribution becomes wider.

Besides novel chemical synthesis method, traditionally sputtering was also used in this dissertation to investigate the ordering behavior of FePt nano-islands. FePt nanoislands were deposited on a heated MgO(001) substrate The influence of different deposition times, substrate temperatures was investigated. Epitaxial growth of FePt nano-islands was observed but the degree of ordering of the nano-islands was low. Ultra-high resolution (S)TEM was used to investigate the reason for the low ordering. Despite the fact that X-ray diffraction shows atomic ordering in the islands, the lattice distortion, atomic segregation and planar defects in these islands possibly lead to deteoration is this the correct spelling of the hard magnetic properties. What is more interesting is that the transformation from *fcc* to *fct* was observed in particles as small as 3 nm. For the first time, a unique onion-like structure was discovered and simulations of the phase formation was in good accordance with the observed structure.

REFERENCES

1. Ross, C., *Patterned magnetic recording media.* Annual Review of Materials Research, 2001. **31**: p. 203-235.
2. Herzer, G., *Modern soft magnets: Amorphous and nanocrystalline materials.* Acta Materialia, 2013. **61**(3): p. 718-734.
3. Pathak, A.K., et al., *Cerium: An Unlikely Replacement of Dysprosium in High Performance Nd-Fe-B Permanent Magnets.* Advanced Materials, 2015. **27**(16): p. 2663-2667.
4. Mohri, K., T. Uchiyama, and L.V. Panina, *Recent advances of micro magnetic sensors and sensing application.* Sensors and Actuators a-Physical, 1997. **59**(1-3): p. 1-8.
5. Chappert, C., A. Fert, and F.N. Van Dau, *The emergence of spin electronics in data storage.* Nature Materials, 2007. **6**(11): p. 813-823.
6. David. J. Sellmyer, R.S., *Advanced Magnetic Nanostructures*. 2006: Springer Science & Business Media. 508.
7. Melzer, M., et al., *Direct Transfer of Magnetic Sensor Devices to Elastomeric Supports for Stretchable Electronics.* Advanced Materials, 2015. **27**(8): p. 1333-+.
8. Takeiri, Y., et al., *Development of an Intense Negative Hydrogen-Ion Source with an External Magnetic Filter.* Review of Scientific Instruments, 1995. **66**(3): p. 2541-2546.
9. Spatz, J.P., et al., *A combined top-down/bottom-up approach to the microscopic localization of metallic nanodots.* Advanced Materials, 2002. **14**(24): p. 1827-1832.
10. Guo, S.J. and S.H. Sun, *FePt Nanoparticles Assembled on Graphene as Enhanced Catalyst for Oxygen Reduction Reaction.* Journal of the American Chemical Society, 2012. **134**(5): p. 2492-2495.
11. Moser, A., et al., *Magnetic recording: advancing into the future.* Journal of Physics D-Applied Physics, 2002. **35**(19): p. R157-R167.
12. Weller, D., et al., *Sub-nanosecond Heat Assisted Magnetic Recording of FePt Media.* Ultrafast Magnetism I, 2015. **159**: p. 228-231.
13. Andreazza, P., et al., *Structure and order in cobalt/platinum-type nanoalloys: from thin films to supported clusters.* Surface Science Reports, 2015. **70**(2): p. 188-258.
14. Klemmer, T., et al., *Magnetic Hardening and Coercivity Mechanisms in L1(0) Ordered Fepd Ferromagnets.* Scripta Metallurgica Et Materialia, 1995. **33**(10-11): p. 1793-1805.

15. Sun, S.H., et al., *Monodisperse FePt nanoparticles and ferromagnetic FePt nanocrystal superlattices.* Science, 2000. **287**(5460): p. 1989-1992.
16. Sun, S.H., *Recent advances in chemical synthesis, self-assembly, and applications of FePt nanoparticles.* Advanced Materials, 2006. **18**(4): p. 393-403.
17. Elkins, K.E., et al., *Ultrafine FePt nanoparticles prepared by the chemical reduction method.* Nano Letters, 2003. **3**(12): p. 1647-1649.
18. Shima, T., et al., *Coercivity exceeding 100 kOe in epitaxially grown FePt sputtered films.* Applied Physics Letters, 2004. **85**(13): p. 2571-2573.
19. Visokay, M.R. and R. Sinclair, *Direct Formation of Ordered Copt and Fept Compound Thin-Films by Sputtering.* Applied Physics Letters, 1995. **66**(13): p. 1692-1694.
20. Thiele, J.U., et al., *Perpendicular magnetic anisotropy and magnetic domain structure in sputtered epitaxial FePt (001) L1(0) films.* Journal of Applied Physics, 1998. **84**(10): p. 5686-5692.
21. Laughlin, D.E., et al., *Crystallographic aspects of L1(0) magnetic materials.* Scripta Materialia, 2005. **53**(4): p. 383-388.
22. Gutfleisch, O., et al., *Magnetic Materials and Devices for the 21st Century: Stronger, Lighter, and More Energy Efficient.* Advanced Materials, 2011. **23**(7): p. 821-842.
23. McFadyen, I.R., E.E. Fullerton, and M.J. Carey, *State-of-the-art magnetic hard disk drives.* Mrs Bulletin, 2006. **31**(5): p. 379-383.
24. Piramanayagam, S.N. and K. Srinivasan, *Recording media research for future hard disk drives.* Journal of Magnetism and Magnetic Materials, 2009. **321**(6): p. 485-494.
25. *http://www.storagenewsletter.com/news/marketreport/ihs-isuppli-storage-space*.
26. *http://www.ece.neu.edu/faculty/nian/mom/technology.html*.
27. Iwasaki, S. and K. Takemura, *Analysis for Circular Mode of Magnetization in Short Wavelength Recording.* Ieee Transactions on Magnetics, 1975. **11**(5): p. 1173-1175.
28. Iwasaki, S. and Y. Nakamura, *Analysis for Magnetization Mode for High-Density Magnetic Recording.* Ieee Transactions on Magnetics, 1977. **13**(5): p. 1272-1277.
29. Iwasaki, S. and K. Ouchi, *Co-Cr Recording Films with Perpendicular Magnetic-Anisotropy.* Ieee Transactions on Magnetics, 1978. **14**(5): p. 849-851.
30. Richter, H.J., *The transition from longitudinal to perpendicular recording.* Journal of Physics D-Applied Physics, 2007. **40**(9): p. R149-R177.
31. Piramanayagam, S.N., *Perpendicular recording media for hard disk drives.* Journal of Applied Physics, 2007. **102**(1).

32. Richter, H.J., *Recent advances in the recording physics of thin-film media (vol 32, pg R147, 1999).* Journal of Physics D-Applied Physics, 1999. **32**(23): p. 3092-3092.
33. Iwasaki, S., *Perpendicular magnetic recording-Its development and realization.* Journal of Magnetism and Magnetic Materials, 2012. **324**(3): p. 244-247.
34. Rottmayer, R.E., et al., *Heat-assisted magnetic recording.* Ieee Transactions on Magnetics, 2006. **42**(10): p. 2417-2421.
35. Wang, J.P., *FePt Magnetic Nanoparticles and Their Assembly for Future Magnetic Media.* Proceedings of the Ieee, 2008. **96**(11): p. 1847-1863.
36. Kuo, C.M. and P.C. Kuo, *Magnetic properties and microstructure of FePt-Si3N4 nanocomposite thin films.* Journal of Applied Physics, 2000. **87**(1): p. 419-426.
37. Luo, C.P., S.H. Liou, and D.J. Sellmyer, *FePt : SiO2 granular thin film for high density magnetic recording.* Journal of Applied Physics, 2000. **87**(9): p. 6941-6943.
38. Bian, B., et al., *Fabrication and nanostructure of oriented FePt particles.* Journal of Applied Physics, 2000. **87**(9): p. 6962-6964.
39. Luo, C.P., et al., *Nanostructured FePt : B2O3 thin films with perpendicular magnetic anisotropy.* Applied Physics Letters, 2000. **77**(14): p. 2225-2227.
40. Ohtake, M., et al., *L1(0) ordered phase formation in FePt, FePd, CoPt, and CoPd alloy thin films epitaxially grown on MgO(001) single-crystal substrates.* Journal of Applied Physics, 2012. **111**(7).
41. Zhang, A.M., et al., *Effects of substrate on structure and the magnetic properties of (001)-textured FePt films grown at low temperature.* Journal of Applied Physics, 2012. **111**(7).
42. Shima, T., et al., *Preparation and magnetic properties of highly coercive FePt films.* Applied Physics Letters, 2002. **81**(6): p. 1050-1052.
43. Miyazaki, T., et al., *Size effect on the ordering of L1(0) FePt nanoparticles.* Physical Review B, 2005. **72**(14).
44. Itoh, Y., et al., *Structural and magnetization properties of island FePt produced by rapid thermal annealing.* Japanese Journal of Applied Physics Part 1-Regular Papers Short Notes & Review Papers, 2004. **43**(12): p. 8040-8043.
45. Tsai, J.L., G.B. Lin, and H.T. Tzeng, *Magnetic properties and microstructure of (001) oriented Ag/FePt, Ag/FePt/Ag films.* Journal of Alloys and Compounds, 2009. **487**(1-2): p. 18-23.
46. Lim, B.C., J.S. Chen, and J.P. Wang, *Thickness dependence of structural and magnetic properties of FePt films.* Journal of Magnetism and Magnetic Materials, 2004. **271**(2-3): p. 159-164.
47. Klemmer, T.J., et al., *Structural studies of L1(0) FePt nanoparticles.* Applied Physics Letters, 2002. **81**(12): p. 2220-2222.

48. Brombacher, C., et al., *Influence of annealing time on structural and magnetic properties of rapid thermally annealed FePt films.* Journal of Physics D-Applied Physics, 2011. **44**(35).
49. Colak, L., *Chemically Synthesized Fe-Pt Binary Alloy Nanoparticles.* 2010.
50. Dai, Z.R., S.H. Sun, and Z.L. Wang, *Phase transformation, coalescence, and twinning of monodisperse FePt nanocrystals.* Nano Letters, 2001. **1**(8): p. 443-447.
51. Sun, S.H., et al., *Controlled synthesis and assembly of FePt nanoparticles.* Journal of Physical Chemistry B, 2003. **107**(23): p. 5419-5425.
52. S. Momose, H.K., N. Ihara, T. Uzumaki, A. Tanaka,, *L10-FePt Nanoparticles in a Magnetically Isolated State.* Jpn. J. Appl. Phys., 2003(42): p. 1252.
53. Chen, M., J.P. Liu, and S.H. Sun, *One-step synthesis of FePt nanoparticles with tunable size.* Journal of the American Chemical Society, 2004. **126**(27): p. 8394-8395.
54. Zeng, H., et al., *Bimagnetic core/shell FePt/Fe3O4 nanoparticles.* Nano Letters, 2004. **4**(1): p. 187-190.
55. Young, H.D., *University Physics, 8th Ed*. 1992: Addison-Wesley.
56. Subir K. Banerjee, R.F.B.a. and R.v.d. Voo., *Essentials of Paleomagnetism.* 2009.
57. D, C.B., *Introduction to Magnetic Materials*. 1972, Reading, MA, USA: Addison-Wesley.
58. Inomata, K., T. Sawa, and S. Hashimoto, *Effect of Large Boron Additions to Magnetically Hard Fe-Pt Alloys.* Journal of Applied Physics, 1988. **64**(5): p. 2537-2540.
59. Englman, R., *Citation Classic - the Energy-Gap Law for Radiationless Transitions in Large Molecules.* Current Contents/Engineering Technology & Applied Sciences, 1988(31): p. 16-16.
60. Ryan, F.M., E.W. Pugh, and R. Smoluchowski, *Superparamagnetism, Nonrandomness, and Irradiation Effects in Cu-Ni Alloys.* Physical Review, 1959. **116**(5): p. 1106-1112.
61. Faraji, M., Y. Yamini, and M. Rezaee, *Magnetic Nanoparticles: Synthesis, Stabilization, Functionalization, Characterization, and Applications.* Journal of the Iranian Chemical Society, 2010. **7**(1): p. 1-37.
62. Herzer, G., *Grain-Size Dependence of Coercivity and Permeability in Nanocrystalline Ferromagnets.* Ieee Transactions on Magnetics, 1990. **26**(5): p. 1397-1402.
63. *Introduction to EM booklet*. 2010: FEI.
64. Leng, Y., *Materials Characterization*. 2008: John Wiley & Sons.
65. *http://www.tulane.edu/~sanelson/eens211/x-ray.htm.*
66. O'Connor, C.J., et al., *Magnetic properties of FePtx/Au and CoPtx/Au core-shell nanoparticles.* Journal of Magnetism and Magnetic Materials, 2001. **226**: p. 1915-1917.
67. *https://www.qdusa.com/products/ppms.html.*

68. Hanada, M., et al., *Improvement of beam uniformity by magnetic filter optimization in a Cs-seeded large negative-ion source.* Review of Scientific Instruments, 2006. **77**(3).
69. Zhang, H.W., Y. Liu, and S.H. Sun, *Synthesis and assembly of magnetic nanoparticles for information and energy storage applications.* Frontiers of Physics in China, 2010. **5**(4): p. 347-356.
70. Balamurugan, B., et al., *Prospects for nanoparticle-based permanent magnets.* Scripta Materialia, 2012. **67**(6): p. 542-547.
71. Mari, A., et al., *Ordered arrays of FePt nanoparticles on unoxidized silicon surface by wet chemistry.* Superlattices and Microstructures, 2009. **46**(1-2): p. 95-100.
72. Akbarzadeh, A., M. Samiei, and S. Davaran, *Magnetic nanoparticles: preparation, physical properties, and applications in biomedicine.* Nanoscale Research Letters, 2012. **7**: p. 1-13.
73. Tiefenauer, L.X., et al., *In vivo evaluation of magnetite nanoparticles for use as a tumor contrast agent in MRI.* Magnetic Resonance Imaging, 1996. **14**(4): p. 391-402.
74. Bader, S.D., *Colloquium: Opportunities in nanomagnetism.* Reviews of Modern Physics, 2006. **78**(1): p. 1-15.
75. Gibot, P., et al., *(Co,Fe)Pt nanoparticles by aqueous route; self-assembling, thermal and magnetic properties.* Journal of Magnetism and Magnetic Materials, 2005. **290**: p. 555-558.
76. Dong, Q., et al., *A Polyferroplatinyne Precursor for the Rapid Fabrication of L10-FePt-type Bit Patterned Media by Nanoimprint Lithography.* Advanced Materials, 2012. **24**(8): p. 1034-1040.
77. Nakaya, M., et al., *Hydrogen-induced crystal structural transformation of FePt nanoparticles at low temperature.* Journal of Physical Chemistry C, 2007. **111**(20): p. 7231-7234.
78. Wen, W.C., et al., *Accelerating disorder-order transitions of FePt by preforming a metastable AgPt phase.* Acta Materialia, 2012. **60**(20): p. 7258-7264.
79. Tzitzios, V., et al., *Direct chemical synthesis of L1(0) FePt nanoparticles.* Journal of Applied Physics, 2011. **109**(7).
80. Nakaya, M., M. Kanehara, and T. Teranishi, *One-pot synthesis of large FePt nanoparticles from metal salts and their thermal stability.* Langmuir, 2006. **22**(8): p. 3485-3487.
81. Wellons, M.S., et al., *Direct synthesis and size selection of ferromagnetic FePt nanoparticles.* Chemistry of Materials, 2007. **19**(10): p. 2483-2488.
82. Capobianchi, A., et al., *General Strategy for Direct Synthesis of L1(0) Nanoparticle Alloys from Layered Precursor: The Case of FePt.* Chemistry of Materials, 2009. **21**(10): p. 2007-2009.

83. Li, W.F., et al., *Fabrication and Microstructure Evolution of Single Crystalline Sm2Co17 Nanoparticles Prepared by Mechanochemical Method.* Journal of Physical Chemistry C, 2013. **117**(20): p. 10291-10295.
84. Gabay, A.M., X.C. Hu, and G.C. Hadjipanayis, *Mechanochemical synthesis of fine R2Fe14BHx and R2Fe14B powders with R = Nd or Nd-Dy.* Journal of Alloys and Compounds, 2013. **574**: p. 472-476.
85. Capobianchi, A., et al., *Crystal and molecular structure of the saline complex hexaaquairon(II) hexachloroplatinate, [Fe(H2O)(6)][PtCl6].* Zeitschrift Fur Kristallographie, 2009. **224**(8): p. 384-388.
86. Hu, X.C., et al., *A low temperature and solvent-free direct chemical synthesis of L1(0) FePt nanoparticles with size tailoring.* Green Chemistry, 2014. **16**(4): p. 2292-2297.
87. X. C. Hu, E.A., C. Ni, G. C. Hadjipanayis, A. Capobianchi, *Direct Green Chemical Synthesis of L10 FePt Nanoparticles with Size Tailoring.* 2013. **Submitted**.
88. Hsiao, S.N., et al., *Effect of Annealing Process on Strain-Induced Crystallographic Orientation of FePt Thin Films.* Ieee Transactions on Magnetics, 2012. **48**(11): p. 4014-4017.
89. Endo, Y., et al., *Lowering of ordering temperature for fct Fe-Pt in Fe/Pt multilayers.* Journal of Applied Physics, 2001. **89**(11): p. 7065-7067.
90. Reddy, V.R., S. Kavita, and A. Gupta, *Fe-57 Mossbauer study of L1(0) ordering in Fe-57/Pt multilayers.* Journal of Applied Physics, 2006. **99**(11).
91. Song, H.M., et al., *Growth of FePt nanocrystals by a single bimetallic precursor [(CO)(3)Fe(mu-dppm)(mu-CO)PtCl2].* Chemical Communications, 2006(12): p. 1292-1294.
92. Christodoulides, J.A., et al., *Magnetic, structural and microstructural properties of FePt/M (M = C, BN) granular films.* Ieee Transactions on Magnetics, 2001. **37**(4): p. 1292-1294.
93. Yu, R., et al., *Multishell Intermetallic Onions by Symmetrical Configuration of Ordered Domains.* Physical Review Letters, 2010. **105**(22).
94. Novoselov, K.S., et al., *Electric field effect in atomically thin carbon films.* Science, 2004. **306**(5696): p. 666-669.
95. Lv, W., et al., *Low-Temperature Exfoliated Graphenes: Vacuum-Promoted Exfoliation and Electrochemical Energy Storage.* Acs Nano, 2009. **3**(11): p. 3730-3736.
96. Qu, L.T., et al., *Nitrogen-Doped Graphene as Efficient Metal-Free Electrocatalyst for Oxygen Reduction in Fuel Cells.* Acs Nano, 2010. **4**(3): p. 1321-1326.
97. Liu, M., X.B. Yin, and X. Zhang, *Double-Layer Graphene Optical Modulator.* Nano Letters, 2012. **12**(3): p. 1482-1485.
98. Ao, Z.M. and F.M. Peeters, *Electric field: A catalyst for hydrogenation of graphene.* Applied Physics Letters, 2010. **96**(25).

99. Sharma, S., et al., *Rapid Microwave Synthesis of CO Tolerant Reduced Graphene Oxide-Supported Platinum Electrocatalysts for Oxidation of Methanol.* Journal of Physical Chemistry C, 2010. **114**(45): p. 19459-19466.
100. Fan, W., et al., *Hybridization of graphene sheets and carbon-coated Fe3O4 nanoparticles as a synergistic adsorbent of organic dyes.* Journal of Materials Chemistry, 2012. **22**(48): p. 25108-25115.
101. Stankovich, S., et al., *Graphene-based composite materials.* Nature, 2006. **442**(7100): p. 282-286.
102. Park, S. and R.S. Ruoff, *Chemical methods for the production of graphenes.* Nature Nanotechnology, 2009. **4**(4): p. 217-224.
103. Zhu, Y.W., et al., *Graphene and Graphene Oxide: Synthesis, Properties, and Applications (vol 22, pg 3906, 2010).* Advanced Materials, 2010. **22**(46): p. 5226-5226.
104. Li, D., et al., *Processable aqueous dispersions of graphene nanosheets.* Nature Nanotechnology, 2008. **3**(2): p. 101-105.
105. Tung, V.C., et al., *High-throughput solution processing of large-scale graphene.* Nature Nanotechnology, 2009. **4**(1): p. 25-29.
106. Wang, H.L., et al., *Mn3O4-Graphene Hybrid as a High-Capacity Anode Material for Lithium Ion Batteries.* Journal of the American Chemical Society, 2010. **132**(40): p. 13978-13980.
107. Zhang, H., et al., *P25-Graphene Composite as a High Performance Photocatalyst.* Acs Nano, 2010. **4**(1): p. 380-386.
108. Rakhi, R.B., et al., *High performance supercapacitors using metal oxide anchored graphene nanosheet electrodes.* Journal of Materials Chemistry, 2011. **21**(40): p. 16197-16204.
109. Kim, J., Y. Lee, and S.H. Sun, *Structurally Ordered FePt Nanoparticles and Their Enhanced Catalysis for Oxygen Reduction Reaction.* Journal of the American Chemical Society, 2010. **132**(14): p. 4996-+.
110. Gengler, R.Y.N., et al., *Revealing the ultrafast process behind the photoreduction of graphene oxide.* Nature Communications, 2013. **4**.
111. Georgakilas, V., et al., *Hydrophilic Nanotube Supported Graphene-Water Dispersible Carbon Superstructure with Excellent Conductivity.* Advanced Functional Materials, 2015. **25**(10): p. 1481-1487.
112. Shin, H.J., et al., *Efficient Reduction of Graphite Oxide by Sodium Borohydride and Its Effect on Electrical Conductance.* Advanced Functional Materials, 2009. **19**(12): p. 1987-1992.
113. Ferrari, A.C., et al., *Raman spectrum of graphene and graphene layers.* Physical Review Letters, 2006. **97**(18).
114. Kudin, K.N., et al., *Raman spectra of graphite oxide and functionalized graphene sheets.* Nano Letters, 2008. **8**(1): p. 36-41.
115. Kaniyoor, A. and S. Ramaprabhu, *A Raman spectroscopic investigation of graphite oxide derived graphene.* Aip Advances, 2012. **2**(3).

116. Torrisi, F., et al., *Inkjet-Printed Graphene Electronics.* Acs Nano, 2012. **6**(4): p. 2992-3006.
117. Mattevi, C., et al., *Evolution of Electrical, Chemical, and Structural Properties of Transparent and Conducting Chemically Derived Graphene Thin Films.* Advanced Functional Materials, 2009. **19**(16): p. 2577-2583.
118. Weller, D. and M.F. Doerner, *Extremely high-density longitudinal magnetic recording media.* Annual Review of Materials Science, 2000. **30**: p. 611-644.
119. Johnston-Peck, A.C., et al., *Sinter-free phase conversion and scanning transmission electron microscopy of FePt nanoparticle monolayers.* Nanoscale, 2011. **3**(10): p. 4142-4149.
120. Antoniak, C., et al., *Enhanced orbital magnetism in Fe50Pt50 nanoparticles.* Physical Review Letters, 2006. **97**(11).
121. Antoniak, C., et al., *A guideline for atomistic design and understanding of ultrahard nanomagnets.* Nature Communications, 2011. **2**.
122. Alloyeau, D., et al., *Size and shape effects on the order-disorder phase transition in CoPt nanoparticles.* Nature Materials, 2009. **8**(12): p. 940-946.
123. Rong, C.B., et al., *Size-dependent chemical and magnetic ordering in L1(0)-FePt nanoparticles.* Advanced Materials, 2006. **18**(22): p. 2984-+.
124. Sato, K., K. Yanajima, and T.J. Konno, *Effect of cooling rate on size-dependent atomic ordering of CoPt nanoparticles.* Philosophical Magazine Letters, 2012. **92**(8): p. 408-416.
125. Yang, B., et al., *The nature of A1-L10 ordering transitions in alloy nanoparticles: A Monte Carlo study (vol 54, pg 4201, 2006).* Acta Materialia, 2006. **54**(19): p. 5335-5335.
126. Blanc, N., F. Tournus, and V. Dupuis, *Measuring the L1(0) chemical order parameter of a single CoPt nanoparticle smaller than 4 nm.* Physical Review B, 2011. **83**(9).
127. Penuelas, J., et al., *Controlling structure and morphology of CoPt nanoparticles through dynamical or static coalescence effects.* Physical Review Letters, 2008. **100**(11).
128. Andreazza, P., et al., *Probing nanoscale structural and order/disorder phase transitions of supported Co-Pt clusters under annealing.* Physical Review B, 2010. **82**(15).
129. Chepulskii, R.V. and W.H. Butler, *Temperature and particle-size dependence of the equilibrium order parameter of FePt alloys.* Physical Review B, 2005. **72**(13).
130. Muller, M., P. Erhart, and K. Albe, *Thermodynamics of L1(0) ordering in FePt nanoparticles studied by Monte Carlo simulations based on an analytic bond-order potential.* Physical Review B, 2007. **76**(15).
131. Tournus, F., et al., *Evidence of L1(0) chemical order in CoPt nanoclusters: Direct observation and magnetic signature.* Physical Review B, 2008. **77**(14).
132. Takahashi, Y.K., et al., *Size effect on the ordering of FePt granular films.* Journal of Applied Physics, 2003. **93**(10): p. 7166-7168.

133. Delalande, M., et al., *L1(0) Ordering of Ultrasmall FePt Nanoparticles Revealed by TEM In Situ Annealing.* Journal of Physical Chemistry C, 2012. **116**(12): p. 6866-6872.
134. Tournus, F., et al., *Multi-L1(0) Domain CoPt and FePt Nanoparticles Revealed by Electron Microscopy.* Physical Review Letters, 2013. **110**(5).
135. Jun Jiang, W.S., Joshua L. Hertz, *Fabrication of Epitaxial Zirconia and Ceria Thin Films with Arbitrary Dopant and Host Atom Composition.* Thin Solid Films, 2012.
136. Vlasova, N.I., G.S. Kandaurova, and N.N. Shchegoleva, *Effect of the polytwinned microstructure parameters on magnetic domain structure and hysteresis properties of the CoPt-type alloys.* Journal of Magnetism and Magnetic Materials, 2000. **222**(1-2): p. 138-158.
137. Xiao, Q.F., et al., *Phase transformation and magnetic properties of bulk CoPt alloy.* Journal of Alloys and Compounds, 2004. **364**(1-2): p. 64-71.
138. Dmitrieva, O., et al., *Quantitative structure analysis of L1(0)-ordered FePt nanoparticles by HRTEM.* Journal of Crystal Growth, 2007. **303**(2): p. 645-650.
139. Dannenberg, A., et al., *Surface energies of stoichiometric FePt and CoPt alloys and their implications for nanoparticle morphologies.* Physical Review B, 2009. **80**(24).
140. Hu, X.R., et al., *Observation of L1(0)-like chemical ordering in a decahedral FePt nanoparticle by C-s-corrected high resolution transmission electron microscopy.* Journal of Applied Physics, 2009. **105**(7).
141. Dai, Z.R., S.H. Sun, and Z.L. Wang, *Shapes, multiple twins and surface structures of monodisperse FePt magnetic nanocrystals.* Surface Science, 2002. **505**(1-3): p. 325-335.
142. Alam, A., B. Kraczek, and D.D. Johnson, *Structural, magnetic, and defect properties of Co-Pt-type magnetic-storage alloys: Density-functional theory study of thermal processing effects.* Physical Review B, 2010. **82**(2).
143. Gruner, M.E., et al., *Multiply twinned morphologies of FePt and CoPt nanoparticles.* Physical Review Letters, 2008. **100**(8).